STRUCTURAL AND THERMOCHRONOLOGICAL CONSTRAINTS ON THE MOVEMENT HISTORY OF THE MONTOSA FAULT, CENTRAL NEW MEXICO

Rose-Anna Behr

Department of Earth and Environmental Science
New Mexico Institute of Mining and Technology
Socorro, New Mexico

Submitted in partial fulfillment of the requirements for the degree of
Masters of Science in Geology

May 1999

ABSTRACT

The 90 kilometer long Montosa fault bounds the east side of the Los Piños and Manzano Mountains of central New Mexico. Overall fault strike is north-northeast and dip is 55-70° west. The fault shows predominantly reverse separation and has been interpreted as Laramide in age. Local normal stratigraphic separation across the fault and normal-slip slickenlines on earlier reverse and strike-slip faults indicate that fault reactivation occurred during Neogene Rio Grande rift extension.

Lineations and kinematic indicators on minor fault planes, and fold hinges, were examined to constrain the direction of maximum shortening during formation of these structures and, by inference, the sense of slip on the Montosa fault. Three different directions of shortening were determined: east-west, northwest-southeast, and north-south. Other workers have reported that structures recording east-west shortening are cross-cut by those recording north-south shortening. East-west shortening would impart dextral reverse oblique-slip motion on the Montosa fault. The central portion of the fault shows strong evidence for northwest-southeast shortening, which would cause sinistral reverse oblique-slip motion on the Montosa fault. Along the north-central portion of the fault, minor planes and folds accommodated north-south shortening, which would result in sinistral reverse oblique-slip motion on the fault. East-west shortening was the most significant stage in the movement history of the Montosa fault, resulting in reverse separation, with a component of dextral strike-slip offset. The Montosa fault also shows evidence of normal reactivation during Neogene Rio Grande rift formation.

Apatite fission track (AFT) analysis was used to determine the thermal history of samples collected in several transects across the fault. Because the thermal history of a sample reflects the tectonic history, AFT data can be used to constrain the relative timing of faulting. AFT data from along the Montosa fault indicate that denudation in early Eocene to late Eocene time (55-35 Ma) resulted in cooling of the lower elevations of the Los Piños Mountains. Samples from the lower elevations of the Manzano Mountains cooled in early Oligocene to early Miocene time (33-22 Ma), ascribable to exhumation following Laramide uplift and during the formation of the Rio Grande rift. The southern fault tip shows normal separation of sedimentary strata, which is attributed to reactivation during rift-related extension. Samples in this area did not cool until the late Oligocene to mid-Miocene (25-14 Ma). Broad track-length distributions suggest that all of the samples remained within the partial annealing zone (PAZ) for apatite (temperature range ~60° to ~120°C) for long periods of time where elevated temperatures caused fission tracks to shorten. Thermal modeling of the AFT ages and track-length distributions reveals that the samples remained in the PAZ for 10-30 million years, then cooled quickly to surface temperatures.

AFT analysis did not show significant age variation across the fault, which indicates that faulting predated cooling; therefore, movement on the Montosa fault during the Laramide orogeny must have occurred at temperatures greater than ~120°C. Any normal fault reactivation during rift formation also occurred at temperatures greater than 60-120°, or was too minimal to be recorded by AFT.

ACKNOWLEDGMENTS

TABLE OF CONTENTS

PART II: APATITE FISSION-TRACK THERMOCHRONOLOGICAL CONSTRAINTS
ON THE MOVEMENT HISTORY OF THE MONTOSA FAULT,
CENTRAL NEW MEXICO

LIST OF TABLES

LIST OF APPENDICES

LIST OF PLATES

INTRODUCTION

The original intention of this thesis research was to constrain the Laramide deformation history of the Montosa fault, which bounds the Los Piños and Manzano Mountains of central New Mexico. Structural analysis of kinematic indicators and thermochronological investigation through apatite fission-track (AFT) analysis were used to investigate the fault history. Structural analysis provided insight into the Laramide deformation history and later fault reactivation during Neogene Rio Grande rift extension. AFT analysis along the Montosa fault, however, revealed unexpectedly young ages indicative of cooling in the early Eocene to mid- Miocene during post-Laramide exhumation and Rio Grande rift extension. Because the structural and AFT data record different events, my thesis has been divided into two separate parts. Each part is independent and intended to stand alone. Part I, titled Structural Constraints on the Laramide Movement History of the Montosa fault, Central New Mexico, documents a structural analysis of fault geometry, fold hinge orientations, and kinematic indicators. Sense of slip on the Montosa fault is determined by the interpreted direction of local maximum shortening during the Laramide orogeny. Part II is titled Apatite Fission-Track Thermochronological Constraints on the Movement History of the Montosa fault, Central New Mexico. AFT analysis was conducted on samples along the Montosa fault to determine the timing of cooling of the hanging wall and footwall rocks and the timing of faulting relative to cooling.

PART I: STRUCTURAL CONSTRAINTS ON THE LARAMIDE MOVEMENT HISTORY OF THE MONTOSA FAULT, CENTRAL NEW MEXICO.

INTRODUCTION

The puzzling aspect of the Laramide orogeny is that the force of large-scale plate interactions was transmitted so far inland - two thousand kilometers from the ancient continental margin (Rodgers, 1987). One theory about the driving force of the Laramide orogeny states that the shallow subduction of the Farallon plate under the North American plate caused a buoyancy of the rigid Colorado Plateau which in turn translated stress inland (e.g., Chapin and Cather, 1981). A second theory is that a foreign terrane collided with the western margin of North America, causing a Himalayan-type orogeny, then translated north due to oblique convergence between the plates ("hit-and-run tectonics", see Maxson and Tikoff, 1996). The angle of plate convergence or the direction of translation of the Colorado Plateau during the Laramide orogeny affected the maximum shortening direction in New Mexico.

Widely variable orientations of principal shortening directions have been inferred for the Laramide orogeny from fault displacement using piercing lines (e.g. Bauer and Ralser, 1995; Cather, 1997; Lucas, 1997), the orientations of dikes (e.g. Rehrig and Heidrick, 1976), kinematic indicators (e.g. Abbott, 1995; Bauer and Ralser, 1995), and fault geometries (e.g. Cabezas, 1987; Fig. 1-1). Most authors have suggested that the inferred Laramide shortening axes are oriented east and northeast, but interpretations vary widely. Several authors have proposed a multi-stage Laramide deformation event (e.g. Knepper and Maars, 1971; Gries, 1983; Cabezas, 1991; Livaccari, 1991; Erslev, 1998), whereas others maintain that a single deformation event occurred (e.g. Reiches, 1949; Stone, 1969).

A controversy exists about the magnitude of dextral strike-slip displacement during the Laramide orogeny on the east side of the Colorado Plateau in the Southern Rocky Mountains. Karlstrom and Daniel (1993) report 100-170 kilometers of displacement, and Cather (1997) suggests that faults in New Mexico acted as a system to accommodate 60-

NNW

Gregson and Erslev, 1997

NW

Stark, 1956 (early)
Selvig, 1994
Erslev, 1997

WNW

Rehrig and Heidrick, 1976

N

Woodward, 1976 (NM)
Gries, 1982
Gries, 1983 (late)

NNE

Livacarri, 1991 (late)

NE

Stark, 1956 (late)
Baltz, 1967
Knepper and Maars, 1971 (middle)
Brown, 1981
Chapin and Cather, 1981 (late)
Keith, 1982
Gries, 1983 (middle)
Seager and Mack, 1983
Erslev, 1993

ENE

Stone, 1969, 1975
Rehrig and Heidrick, 1976
Chapin and Cather, 1981 (early)
Heidrick and Titley, 1982
Colpitts, 1986
Livacarri, 1991 (early)
Jurista et al., 1995

E

Reiches, 1949
Knepper and Maars, 1971 (early)
Woodward, 1976 (NV)
Gries, 1983 (early)

Figure 1-1. Various authors and the directions of maximum shortening during the Laramide orogeny they inferred from field and kinematic data. Timing or location is listed in parentheses if multi-stage Laramide deformation was suggested.

120 kilometers of offset. Lucas (1997) maintains that a maximum of 5-20 kilometers of dextral strike-slip displacement occurred across New Mexico. Dextral displacement across New Mexico is postulated to have occurred on strike-slip, or oblique-slip, north-striking faults. Because several faults were active in New Mexico during the Laramide orogeny, including the Nacimiento fault, the Rio Puerco fault zone, the Picuris-Pecos fault, the Tijeras-Cañoncito fault zone, and the Montosa fault (Fig. 1-2), an examination of these faults is necessary to resolve the controversy. The north-striking Nacimiento fault has been interpreted as both a dextral oblique-slip fault (Baltz, 1967) and a purely reverse fault (Stewart and Hibbard, 1992). The Rio Puerco fault zone has been reported to have dextral oblique-slip offset due to "a north-trending right-shift force couple" (Slack and Campbell, 1976). The north-striking Picuris-Pecos fault in the Sangre de Cristo Mountains was originally interpreted as a reverse fault during the Laramide orogeny (Sutherland in Miller et al., 1963). Miller et al. (1963) determined the fault was also dextral strike-slip, but misinterpreted faulting to be Precambrian in age. More recently, Bauer and Ralser (1995) suggested the fault has significant dextral strike-slip displacement with minor parallel reverse faults in a positive flower structure. The Tijeras-Cañoncito fault zone strikes northeast and has a complex tectonic history. Stearns (1953) described the fault zone as predominantly normal. Lisenbee et al. (1979) reported sinistral strike-slip, whereas Abbott (1995) reported mostly dextral strike-slip faulting during the Laramide orogeny.

Like other faults in New Mexico, the magnitude of dextral strike-slip motion across the north-northeast striking Montosa fault is controversial. Originally the fault was believed to have been a purely reverse fault (Stark and Dapples, 1946; Reiches, 1949; Stark, 1956; Kelley, 1977). More recently, evidence for dextral oblique-slip movement has been found (Cabezas, 1987; Hayden, 1991). Cather (1992) hypothesized that the Tijeras-Cañoncito fault zone acted as a right step in a dextral shear system including the Picuris-Pecos fault to the north and the Montosa fault to the south (Fig. 1-2).
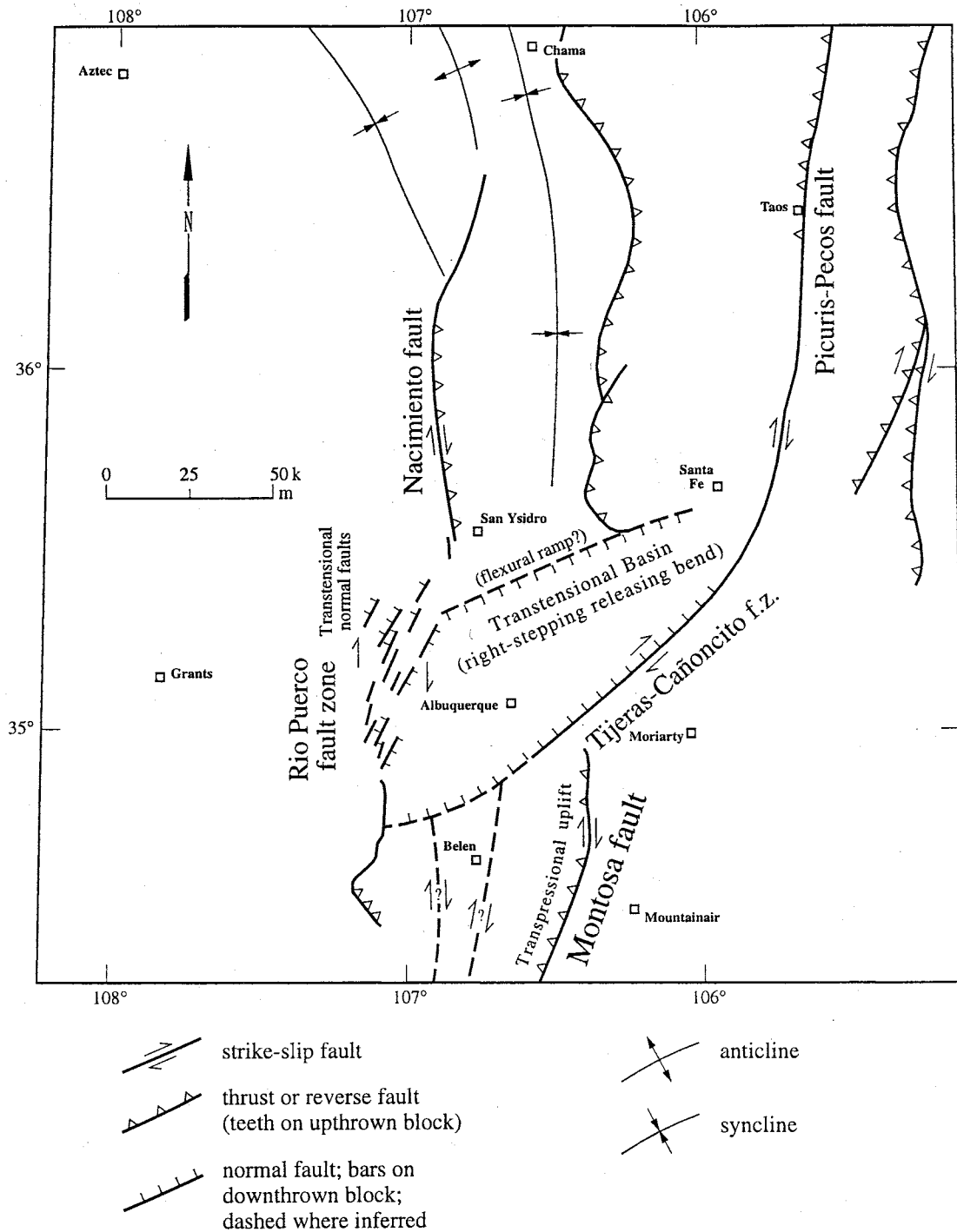
Figure 1-2. Laramide age faults and structures in northern and central New Mexico. Map and movement sense interpretations from Cather (1992).

The Montosa fault is 90 kilometers long and bounds the eastern side of the Los Piños and Manzano Mountains of central New Mexico (Fig. 1-3). The fault has been interpreted as Laramide (Late Cretaceous- early Tertiary) in age because it cuts Permian sedimentary rocks and fission-track ages indicate that faulting pre-dated the Oligocene to Miocene (Part II). Overall fault characteristics include a generally north-northeast strike and westward dip. Locally, the fault strike varies from N40W to N45E. The fault has two prominent right en échelon steps, a major left step, and many minor subparallel fault splays. The northern two-thirds of the fault shows reverse separation with Precambrian schist, quartzite, granitoid, and Pennsylvanian limestone juxtaposed against Pennsylvanian and Permian limestone and sandstone (Stark and Dapple, 1946; Reiches, 1949; Stark, 1956). The southern third of the fault shows normal separation with Pennsylvanian and Permian rocks juxtaposed against one another (Cabezas, 1987).

A COCORP (Consortium for Continental Reflection Profiling) seismic line across Abo Pass and the Rio Grande rift revealed a strong reflector interpreted as the Montosa fault, which is listric (Fig. 1-4; de Voogd et al., 1986). The Paloma fault and the Cenozoic normal Los Piños fault, which bounds the west side of the Los Piños Mountains, sole into or truncate at the Montosa fault at depth.

Because the Montosa fault itself is poorly exposed and shows no kinematic indicators, minor faults associated with the Montosa fault were examined to constrain movement sense. Sense of slip on minor planes was determined by examining slickensides, slickenside striae, slickenfibers, and Riedel shears (e.g. Petit, 1987). The sense of slip on minor faults, in addition to the orientations of fold hinges and overall fault geometry were used to evaluate regional shortening directions. This study determined that most of the deformation along the Montosa fault occurred in the early Laramide orogeny during an east-west shortening regime.

New Mexico

	Quaternary
	Triassic and Cretaceous
	Triassic
	Permian
	Pennsylvanian
	Precambrian

Montosa fault

CHILILI•

•LOS LUNAS

•TORREON

•BELEN

•MANZANO

•BOSQUE

Manzano Mountains

MOUNTAINAIR•

•ABO

US-60

Abo Pass

I-25 •LA JOYA

Cerro Montoso

Los Piños Mtns.

34°15' •SAN ACACIA

Black Mesa

Sierra de la Cruz

•LEMITAR

Cañoncito de la Uva

N

30 km

•SOCORRO

107°00'   106°45'   106°30'   106°15'
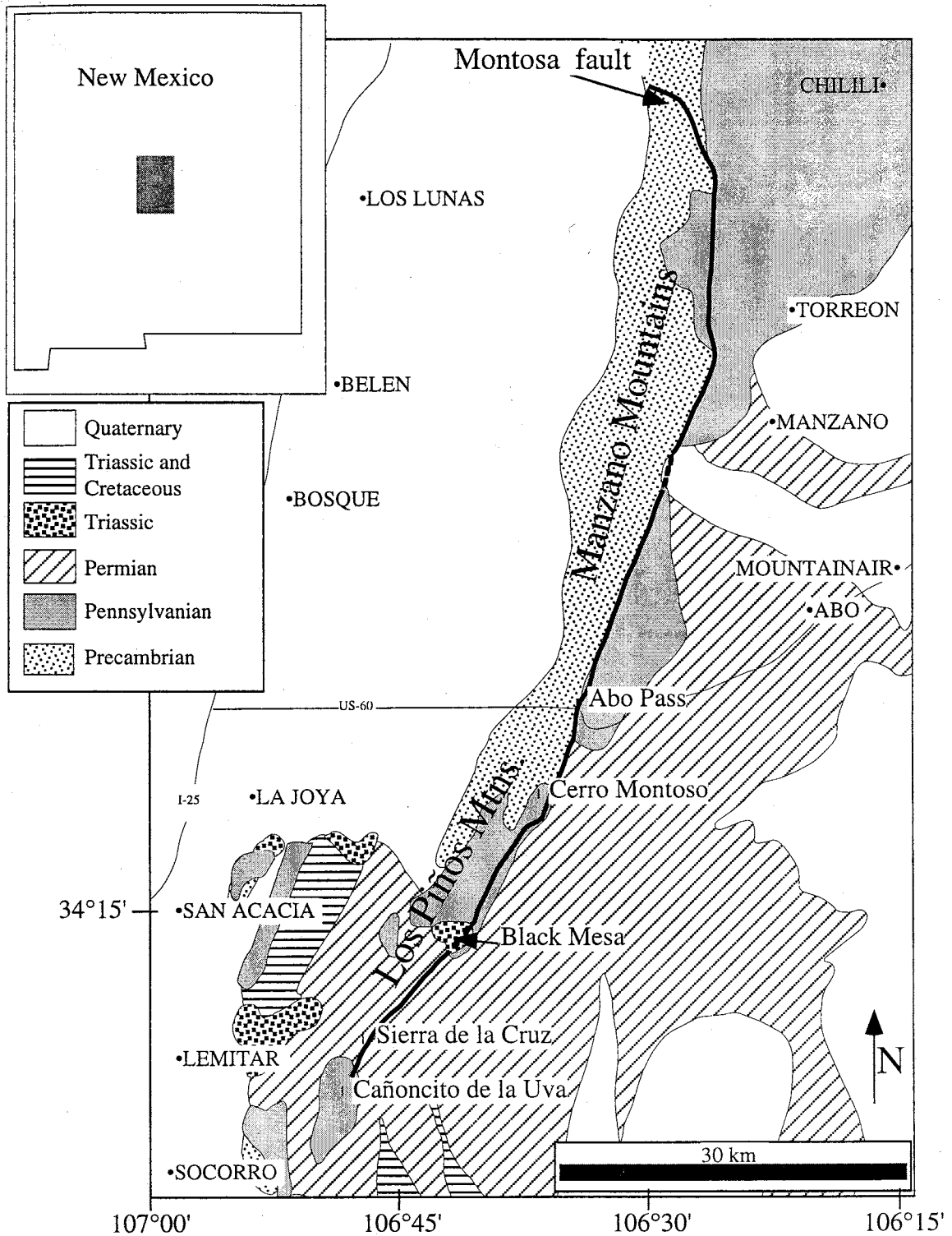
Figure 1-3. The west-dipping Montosa fault and surrounding area. Location of study area shown in upper left corner. After New Mexico Geological Society Map of New Mexico (1982).
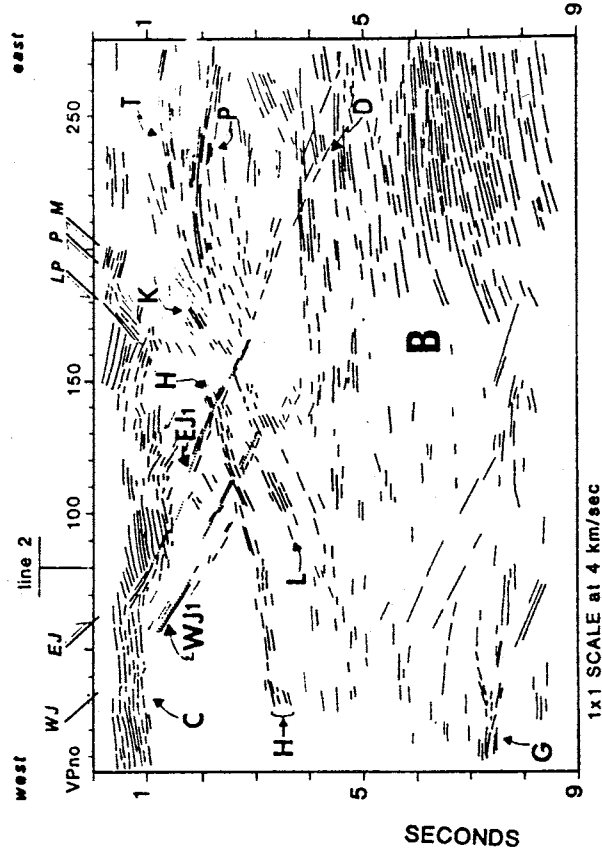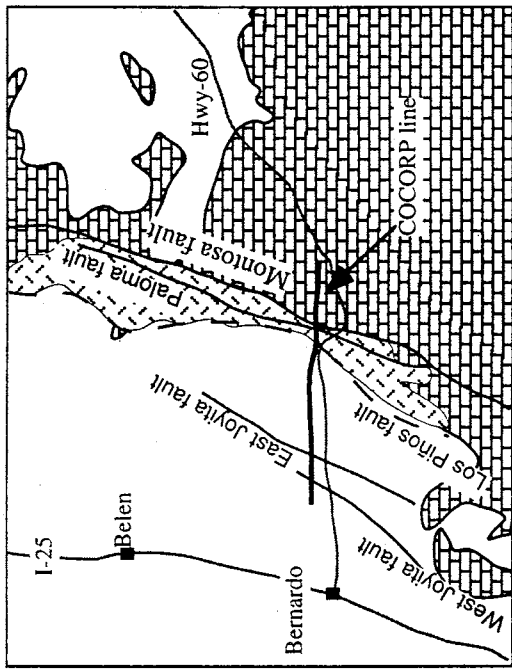
Figure 1-4. Data from the COCORP seismic line across Abo Pass. The Montosa fault (M), Paloma fault (P), and Los Piños faults (LP) are noted. Reflector H is believed to be the Montosa fault at depth. The Paloma fault soles into the Montosa fault, and the Los Piños fault, a Cenozoic rift bounding fault, is believed to have reactivated the older faults at depth. Locator map in the upper left. Data and interpretations from de Voogd et al. (1986)

TERMINOLOGY

Minor fault planes and kinematic indicators spatially associated with the Montosa fault have been measured in the field, in hand sample, and in thin section. These planes contain various kinematic indicators including polished or striated movement surfaces. In this paper, the term "slickensides" is applied to polished slip surfaces, which may or may not be striated (Fleuty, 1975) whereas the term "slickenlines" is used to describe linear structures visible as striations or ridges and grooves on slickensides. Slickenfibers are fibrous vein materials, often calcite (Fig. 1-5A). Because they form a lineation as they grow in the direction of fault movement, forming steps in the direction of slip, slickenfibers can be used as kinematic indicators. Slickenside striae are lineations that form due to friction on the fault surface (Fig. 1-5B). Secondary faults and fractures, termed R, R', P, and T shears, often form with major faults and minor movement surfaces (Fig. 1-6; Petit, 1987) and can be used to determine the sense of slip on a fault plane.

Paleozoic Stratigraphic Nomenclature

The Paleozoic stratigraphic nomenclature used by previous workers along the Montosa fault is inconsistent (Table 1-1). Specifically, maps of the northern half of the fault use the name Madera Limestone (Keyes, 1903) for the thick Pennsylvanian-Permian age limestones common throughout the area. The southern half of the fault has been mapped more recently and the Madera Limestone has been renamed the Wild Cow Formation (Myers, 1973). I will use the more recent nomenclature.

METHODS

Field Studies

Three kilometers of the fault trace were mapped in detail (1:12,000) in Sand Canyon, through Abo Pass, and along the edge of the Sais Santa Fe Quarry. Two kilometers at the southern end of the fault near Gallina Well were also mapped in detail. Mapping was restricted to within one kilometer of the fault because kinematic indicators
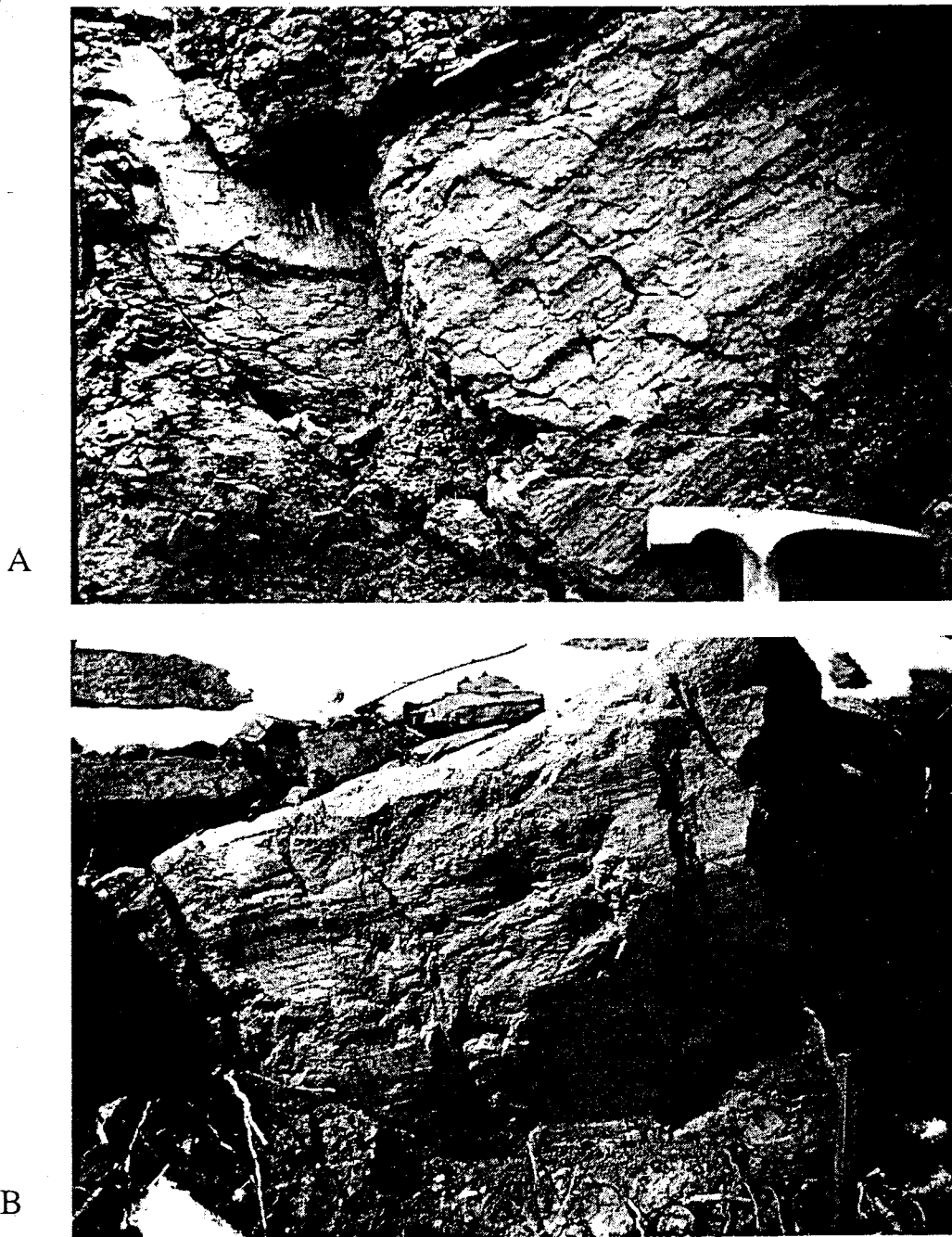
Figure 1-5 A) Two sets of calcite slickenfibers in red limy mudstone at Gallina Well. The set on the right shows dextral normal oblique-slip. The set on the left records normal motion. B) Slickenside striae on Permian Abo sandstone at Cañon Colorado.
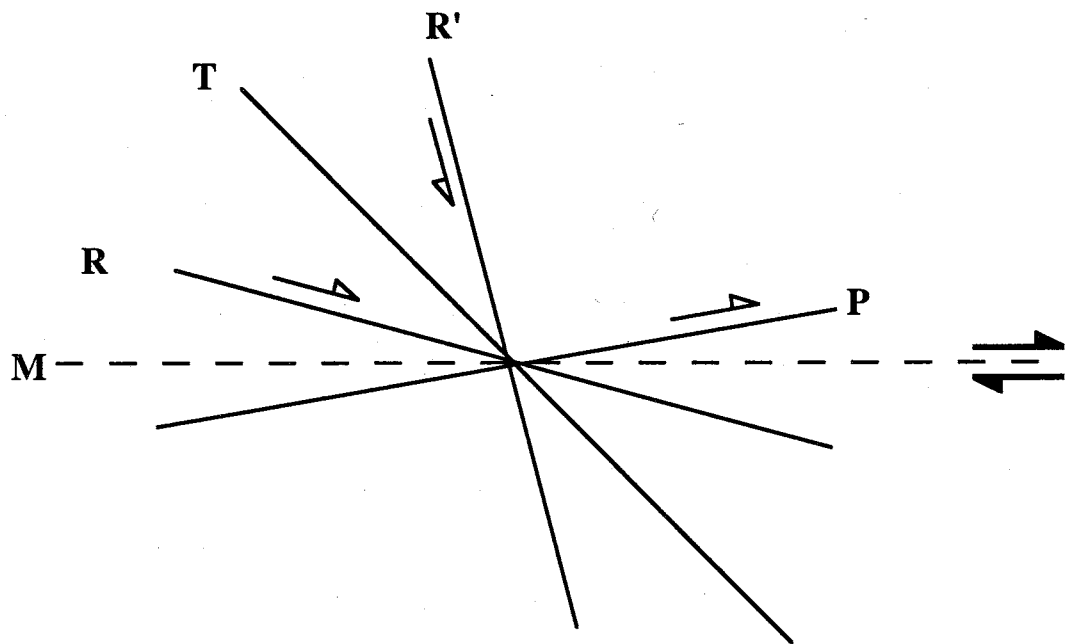
Figure 1-6. Orientations and kinematics of shear and extension fractures associated with a fault plane. M is the main slip surface showing dextral motion. R, a Riedel shear, is a synthetic, low-angle fault. P is similar to R but with a different angle of inclination from the slip surface. R' is a high-angle antithetic shear fracture. T is a tensile fracture. From Petit (1987).

			<u>Names at the southern end</u>	<u>Differences at the northern end</u>

Paleozoic	Permian	Leonardian	Yeso Formation
			   Joyita Member
			   Canas Member
			   Torres Member
			   Meseta Blanca Sandstone Member	

		Wolfcampian	Abo Formation	
			Bursum Formation	
			Wild Cow Formation La Casa Member	Madera Limestone
	Pennsylvanian	Virgilinian	Pine Shadow Member	
		Missourian	Sol se Mete Member	
		Desmoinesian	Los Moyos Limestone	= lower Madera Limestone
		Atokan	Sandia Formation	
		Morrowan		

Table 1-1. Paleozoic stratigraphic nomenclature along the Montosa fault.

were sparse further from the fault. Detailed mapping helped resolve differences in previous workers maps but did not reveal any new discoveries. Reconnaissance mapping and measurements were compiled in the Manzano Mountains at Cañon de los Seis, Cañon de Tajique, Cañon Nuevo, Cañon Colorado, the water gap at Pine Shadow Spring and an additional gap three kilometers south of Pine Shadow Spring (Plate 1). In the Los Piños Mountains, reconnaissance work was done at Parker Ranch, Montosa Draw, and the southern end of Grey Ridge at Black Mesa. The orientations of slickenside striae, slickenfibers, and Riedel shears were determined (Appendix A). Oriented samples of slickenlines were collected where movement on faults and fractures was ambiguous and warranted closer examination.

Vertical Separation

Vertical separation was estimated by determining the difference in elevation of a given stratigraphic contact on either side of the fault. Where the fault has multiple strands, separation across the entire fault zone was estimated. If two like contacts were not exposed, vertical separation was extrapolated using stratigraphic thicknesses. In the Manzano Mountains, the Precambrian-Pennsylvanian contact is exposed on the west side of the fault. On the east side of the fault, only contacts within the Pennsylvanian Wild Cow Formation are exposed. The predicted elevation of the Precambrian-Pennsylvanian unconformity was determined by subtracting the known stratigraphic thicknesses of the Pennsylvanian section as recorded on the maps (Myers and McKay, 1971; Myers and McKay, 1972; Myers et al. 1986). Vertical separation was subsequently estimated. In the Los Piños Mountains, the Precambrian-Pennsylvanian unconformity is exposed on the west side of the fault and Permian rocks are exposed on the east. South of Black Mesa, Permian contacts are exposed on both sides of the fault and vertical separation can be determined from the difference in elevation of these contacts on either side of the Montosa fault. No data were found to constrain horizontal separation.

Analytical Methods

All measured fault planes were plotted on lower hemisphere equal area plots using the program StereoNet v. 4.9.5 (Allmendinger, 1995). Planes with known sense of slip were plotted separately from those with unknown sense of slip. Shortening and extension axes were determined from these planes and associated slickenlines using FaultKin v. 3.8.3 (Allmendinger et al., 1992). Where fault planes and slickenlines with unknown sense of slip were parallel to those of known sense of slip, the unknown were assumed to have the same sense of slip as the known. These fault planes are referred to as inferred planes.

Rose diagrams of fold hinge trace orientations were plotted using Rosy v. 2.13, a two dimensional orientation analysis program (McEachran, 1994).

THE MONTOSA FAULT

Over its 90 kilometer length, the Montosa fault has an overall strike of N20E but the strike varies from N40W at the northern fault tip to nearly due east in a one of three prominent fault bends (Plate 1). A variable strike will result in a variation in the sense of slip given a particular stress field. During east-west shortening, for example, the north-striking portion of the fault would experience reverse motion, whereas the northeast-striking portion would deform through reverse dextral oblique slip. A right step in the fault would experience reverse dextral oblique slip in an east-west shortening regime. The fault dip varies from 55°-75° west, approximately parallel to the Precambrian basement foliation. Except for 1.2 kilometers in Sand Canyon and the southern 24 kilometers of the fault, the hanging wall is composed of Precambrian schist, quartzite, metarhyolite, greenstone, and granitoid, locally capped by very shallowly (<5°) south-dipping middle Pennsylvanian sedimentary rocks of the Sandia and Los Moyos Formations. In Sand Canyon north of Abo Pass, the Montosa fault juxtaposes the Precambrian Priest quartz monzonite (Thompson et al., 1996) against the Pennsylvanian Sandia and Los Moyos Formations,

except for 1.2 kilometers where the hanging wall contains the Pennsylvanian-Precambrian unconformity, the Priest quartz monzonite, and a sliver of limestone (Stark, 1956). The southern 24 kilometers of the hanging wall consists of middle Pennsylvanian to lower Permian formations including the Pennsylvanian Sandia, Los Moyos, and Wild Cow Formations, and the Permian Bursum, Abo, and Yeso Formations, which also dip very shallowly (~5°) south. The entire footwall consists of middle Pennsylvanian to lower Permian sedimentary rocks which dip very shallowly south (~6°).

The northern third of the fault is poorly exposed due to vegetative cover. The central forty-five kilometers of the fault are marked by a prominent ridge of vertical to overturned limestone beds in the footwall (Fig. 1-7). The actual fault zone is not exposed but the fault trace is easily followed. The southern sixteen kilometers of the fault occupy a broad valley between cuestas and mesas.

Stratigraphic separation along the fault varies from reverse separation at the northern tip to normal separation at the southern tip. Reverse separation at the northern fault tip is 670 meters (Plate 1). Reverse separation is 450-670 meters across the Montosa fault and a subparallel splay in the central Manzano Mountains, and 670 meters in the northern Los Piños Mountains, at Cerro Montoso. Just north of Black Mesa, away from the effects of a major drag fold, evidence is found for 155 meters of reverse separation. Near the fault, 90 meters of normal separation exists, indicating that the fault was reactivated. On the west side of the fault, the lower contact of the Pennsylvanian-Permian Sol se Mete Member of the Wild Cow Formation has an elevation of 1740 meters; on the east side, the contact is exposed at an elevation of 1830 meters in the vertical beds that make up Grey Ridge. Assuming that the contact used to be continuous, at least 90 meters of normal displacement has occurred. South of Black Mesa, the fault shows 160 meters of normal separation across a zone of multiple, anastomosing fault strands that strike N35E. Normal separation decreases to 90 meters three kilometers from the fault tip.
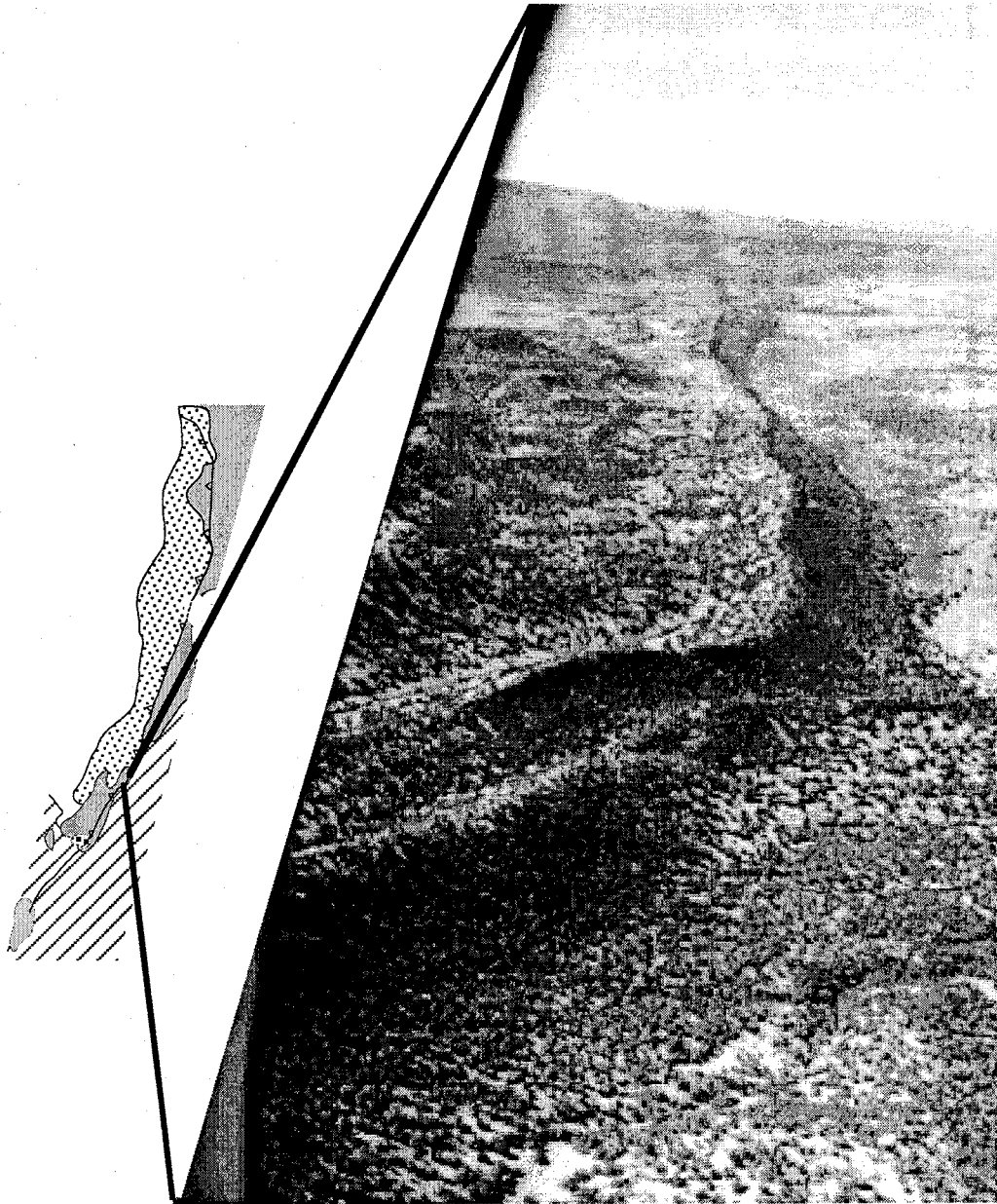
Figure 1-7. Vertical beds of limestone form a prominent ridge
along the footwall. Initially hrizontal beds are overturned near the fault.
View is to the south of the right en échelon step in the Montosa fault by
Cerro Montoso. Locator map on the left.

Where exposed, the Montosa fault is characterized by a zone of brittle deformation rather than a single slip plane. A well exposed cross-section of the fault in a railway cut by Abo Pass includes a seven meter wide zone oriented N25E, 60W of cataclasite, breccia, and jumbled blocks. Hanging wall Precambrian quartzite is juxtaposed against Pennsylvanian limestone. On the north side of the railroad tracks, the northwest edge of the fault zone is bound by an approximately 30 centimeter wide zone of angular quartzite clasts in a matrix of lime mud. The central portion of the fault zone contains jumbled, discontinuous beds of limestone. The southeast edge of the fault zone is bound by a limy mud to shale. Such layers of weaker lithologies may have accommodated some fault slip. Outside the fault zone, quartzite and limestone beds are nearly parallel to the fault zone and are cut by minor reverse and normal faults. On the southwest side of the railroad tracks the layer of quartzite clasts in lime mud matrix is absent, and the northwest side of the fault is bound by a well indurated quartzite breccia.

At the southern end of Grey Ridge, north of Black Mesa, the Montosa fault is partially exposed as a foliated limy mud. The footwall is shallowly dipping beds of Permian Abo and Yeso Formation with Pennsylvanian Los Moyos and Wild Cow Formation folded to vertical near the fault. The hanging wall is Pennsylvanian Los Moyos limestone covered by Quaternary deposits. The dips of both hanging wall and footwall limestone beds steepen to the west near the fault. Stratigraphic offset records 115 meters of reverse separation. The fault zone itself shows two foliations and contains crinoids and bivalves which have been flattened within the plane of foliation. In one area the main foliation is oriented 82°, 61N and the secondary foliation is oriented 33°, 84 E. These planes show dextral sense of slip on the main foliation. Nearby, the main foliation trends 045° and the secondary trends 065°, indicating sinistral slip. There are possibly more than two foliations in this area, which record multiple episodes of deformation. The foliations are therefore inconclusive kinematic indicators.

The Paloma fault

The Paloma fault is a major imbricate branch of the Montosa fault (Kelley, 1977). It is about 38 kilometers long, dips west, and nearly parallels the Montosa fault (Plate 1). The Paloma fault terminates southward against the Montosa fault at the right step in the Montosa fault just south of Cerro Montoso, and dies out near Cañon Colorado. The fault juxtaposes Precambrian rocks and shows 180 meters of vertical separation by Cerro Montoso. Ten kilometers north of Highway 60 the fault shows at least 735 meters of vertical separation (Stark, 1956).

Minor Faults

Over 500 slickensides, slickenside striae, and slickenfibers were measured on small faults in the field (Appendix A). Sixteen of the minor faults were examined in thin section to determine sense of slip (Appendix B). Sense of slip was determined on 135 surfaces in the field and was inferred on 125 of the unknown surfaces because slickensides and slickenlines had orientations similar to features with known sense of slip. If slickenline rake was greater than or equal to 45°, the fault is considered dominantly dip-slip. If the rake was less than 45°, it is considered dominantly strike-slip. Seven localities were examined for kinematic indicators (Plate 1). These localities are discussed from north to south in the following sections.

Cañon Colorado

Where the fault strikes N5E in Cañon Colorado, a few outcrops reveal good kinematic indicators in arkoses of the Permian Abo Formation. Slickenlines are common and slickensides are well developed with a millimeter thick cataclasite layer. Of the nineteen surfaces measured, only four display kinematic indicators. Two planes dip steeply north and record predominantly reverse motion with a minor component of dextral strike-slip motion (Fig. 1-8). One plane dips moderately northeast, and shows purely dextral strike-slip motion (Fig. 1-9). Another dips shallowly southwest, and shows pure sinistral strike-slip motion (Fig. 1-9). Six slickensides parallel the plane with known
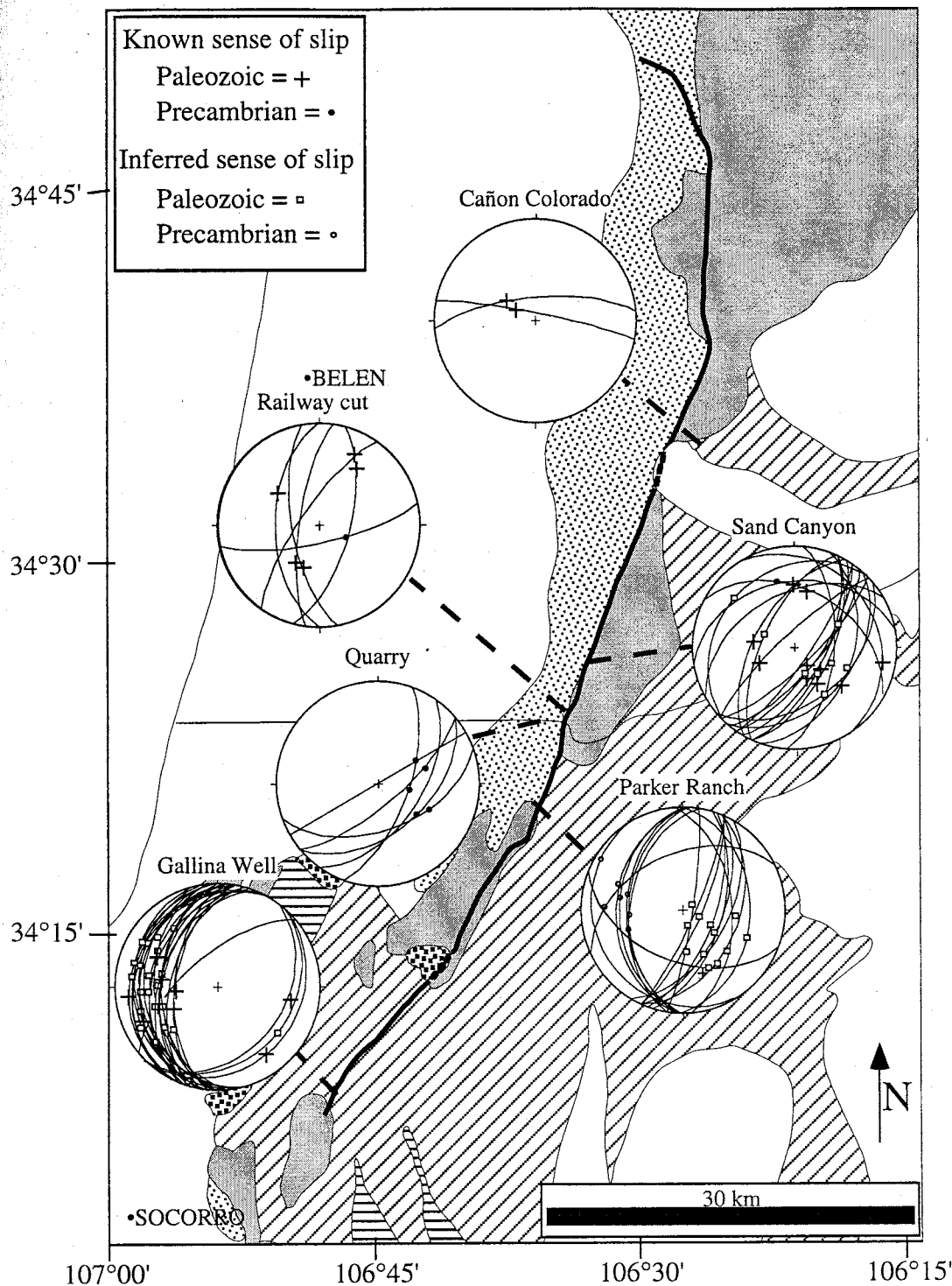
Figure 1-8. Lower hemisphere equal area plots of minor reverse faults along the Montosa fault. A dashed line connects each plot to the region in which the data were collected; localities are listed above the plots. Base map after New Mexico Geological Society Map of New Mexico (1982).
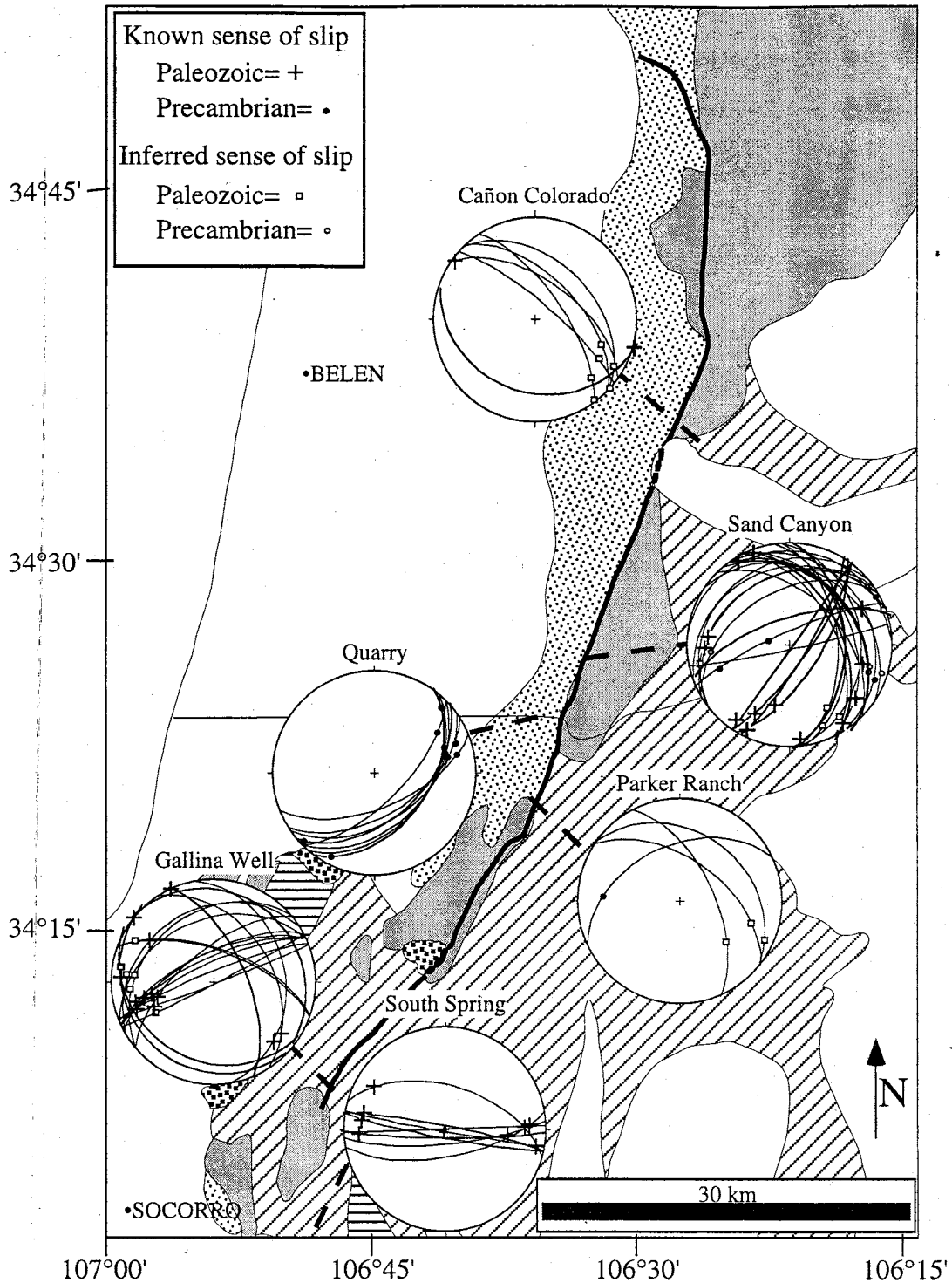
Figure 1-9. Lower hemisphere equal area plots of minor strike-slip faults along the Montosa fault. Dextral strike-slip faults are on the map, and sinistral strike-slip faults are on the overlay. A dashed line connects each plot to the region in which the data were collected; localities are listed above the plots. Base map after New Mexico Geological Society Map of New Mexico (1982).

dextral strike-slip movement. Slickenlines on these planes rake 0-20° SE and are inferred to record dextral strike-slip motion (Fig. 1-9).

Sand Canyon

Three kilometers of the Montosa fault, and up to 300 meters on either side of the fault, were examined for kinematic indicators in Sand Canyon. The Sand Canyon area contains a right-stepping bend in the Montosa fault (Plate 1) that has been interpreted as a transtensional step by Hayden (1991). In this area, the fault generally juxtaposes Precambrian quartzite, schist, and Priest quartz monzonite of the hanging wall against Pennsylvanian Sandia and Los Moyos sandstone and limestone of the footwall. This is observed everywhere except for a 1.5 km stretch where limestone is juxtaposed against limestone (Stark, 1956). Kinematic indicators in the limestones are typically calcite slickenfibers, but occasional slickenside striae were noted. The sandstones include excellent exposures of slickensides with thin layers of cataclasite. Slickenlines are distinct and often stained with iron. For clarity, the faults in Precambrian and Paleozoic rocks will be discussed separately.

Few faults showing clear kinematic indicators are present in the Precambrian rocks. Only one reverse plane was measured and it was parallel to several normal faults (Compare Figs. 1-8 and 1-10). Four dextral strike-slip faults were measured (Fig. 1-9), but no sinistral strike-slip faults were found.

Pennsylvanian beds east of Sand Canyon are nearly flat lying. Next to the fault is an asymmetric fold with one virtually horizontal limb and one nearly vertical limb. Reverse fault planes strike NNE to ENE and dip shallowly to moderately NNW, NW, and SE (Fig. 1-8). Except for a plane that dips WNW, all faults exhibit a minor component of sinistral strike-slip motion. One plane oriented parallel to the Montosa fault has slickenfibers that rake 80°S. Two sets of normal faults were found: a shallowly northeast-dipping dextral normal oblique-slip set and a shallowly southeast-dipping normal sinistral oblique-slip set (Fig. 1-10). Dextral strike-slip faults in the Pennsylvanian rocks in Sand Canyon fit into
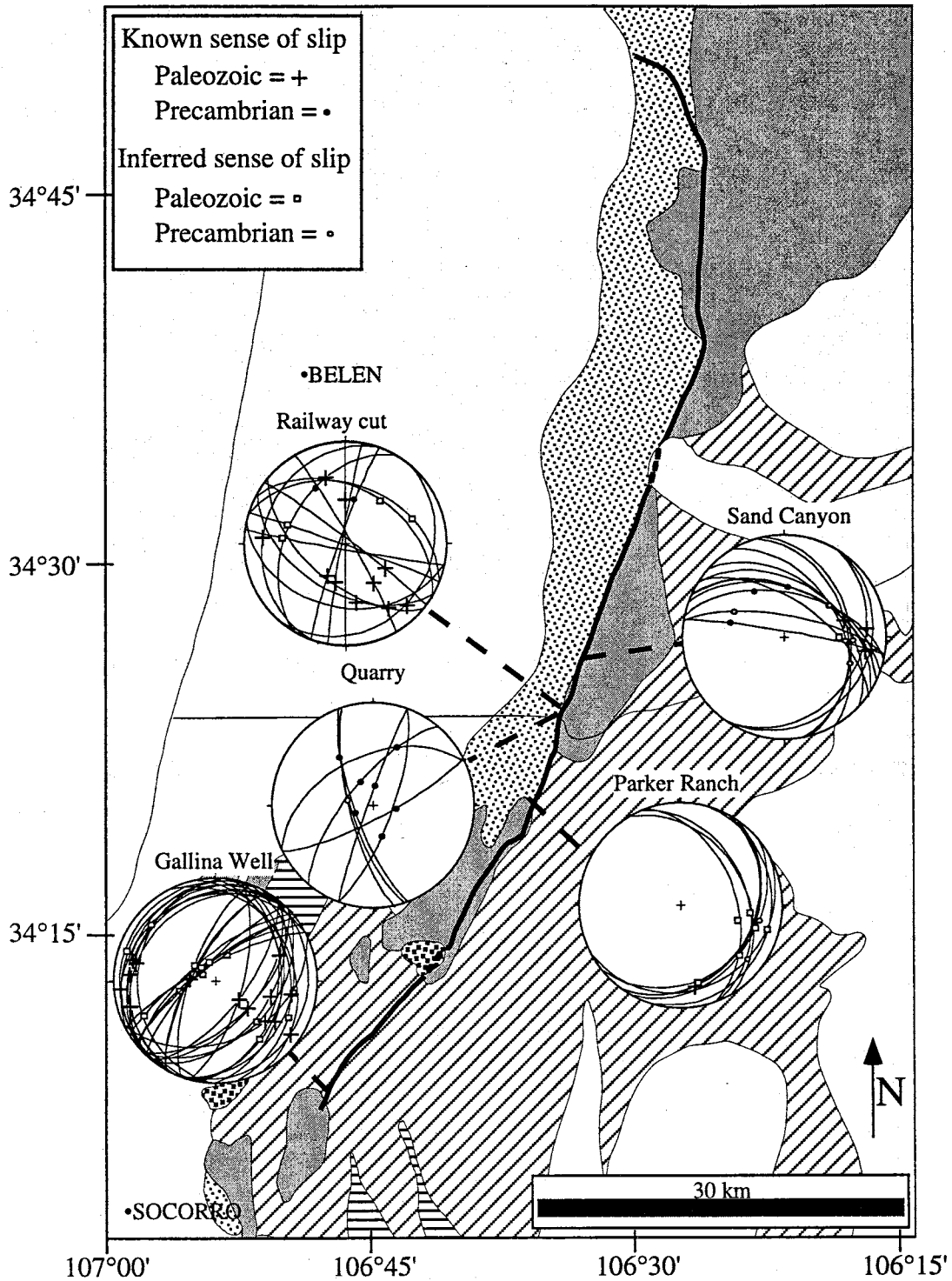
Figure 1-10. Lower hemisphere equal area plots of minor faults with normal sense of slip. A dashed line connects each plot to the region in which the data were collected; localities are listed above the plots. Base map after New Mexico Geological Society Map of New Mexico (1982).

two categories (Fig. 1-9). First, a moderately northeast-dipping dextral oblique-slip set with a component of normal motion parallels the dextral normal oblique-slip faults. Second, a northwest-dipping dextral oblique-slip fault set with a component of reverse motion was noted. A population of steeply southeast-dipping faults with shallowly southwest-plunging calcite slickenfibers shows sinistral strike-slip with minor reverse motion (Fig. 1-9). A few east- to northeast-dipping sinistral strike-slip faults were recorded. Sixteen faults with an ambiguous sense of slip are parallel to planes which show reverse, dextral strike-slip, or normal motion (Figs. 1-8, 1-9, and 1-10 respectively).

One fault with undetermined sense of slip parallels the normal faults in the Precambrian rocks, and several are parallel to normal faults in the Pennsylvanian rocks (Fig. 1-10). Four faults in the Precambrian rocks were inferred to be dextral strike-slip faults because they are parallel to dextral strike-slip faults in both Precambrian and Pennsylvanian rocks (Fig. 1-9).

Railway

The railway cut just south of Sand Canyon has exposed several faults. Outside the fault zone, one reverse and two normal faults were observed in the Precambrian quartzite (Figs. 1-8 and 1-10, respectively). In the Pennsylvanian rocks of the railway cut, a population of both steeply and shallowly dipping normal fault planes was recorded (Fig. 1-10). Three reverse faults were also found in the Pennsylvanian rocks outside the fault zone (Fig. 1-8). Four planes measured within the fault zone are parallel to normal fault planes in Precambrian rocks in Sand Canyon, and are thus inferred to be normal faults (Fig. 1-10).

Sais Santa Fe Quarry

The Sais Santa Fe Quarry is located south of Abo Pass and the Sand Canyon fault bend. The quarry offers a dramatic three-dimensional view of the Precambrian quartzite and schist in the hanging wall proximal to the Montosa fault. Several kinematic indicators were found. Six reverse faults with a dextral component of slip and several reverse dextral oblique-slip faults dip moderately to steeply southeast (Figs. 1-8 and 1-9). Two sets of

planes record normal sense of slip (Fig. 1-10). Six dextral strike-slip faults dip shallowly southeast with slickenlines that rake northeast, indicating a minor component of reverse motion (Fig. 1-9). Three sinistral oblique-slip planes in the quarry show minor thrust motion and dip moderately southeast (Fig. 1-9). Two planes were inferred to have normal motion because they are parallel to the normal faults (Fig. 1-10).

Parker Ranch

The term "Parker Ranch" refers to the area along the fault from Highway 60 to Parker Ranch, located at the foot of Cerro Montoso. One fault in the Precambrian rocks has kinematic indicators that record reverse dextral oblique-slip motion on a northwest-dipping fault (Fig. 1-9). Only two fault planes in Pennsylvanian rocks had kinematic indicators (Figs. 1-8 and 1-10). However, over twenty fault planes in both the Precambrian and Pennsylvanian rocks are parallel to faults in Sand Canyon and Gallina Well and the sense of slip on these planes has thus been tenuously inferred (Figs. 1-8, 1-9, and 1-10).

Gallina Well

The Gallina Well area is located at the southern fault tip in red and white sandstone, mudstone, siltstone, and limestone of the Permian Bursum, Abo and Yeso Formations. In this area, the fault consists of multiple braided strands. Two and a half kilometers along the fault and about 300 meters on either side of the fault were examined for kinematic indicators. A conjugate set of NNE-striking reverse fault planes was found at Gallina Well (Fig. 1-8). Normal faults are generally parallel to reverse faults (compare Figs. 1-8 and 1-10). Slickenside striae showing normal sense of slip are also noted cross-cutting strike-slip striae. Ten dextral strike-slip faults were measured, the majority of which strike NE to ENE with a near vertical dip (Fig. 1-9). A few other dextral strike-slip faults were noted. Only three sinistral strike-slip faults were measured in the Gallina Well area (Fig. 1-9).

Many of the faults in this area did not have clear kinematic indicators. Several shallow to moderately west-dipping planes and one southeast-dipping plane were inferred

to record reverse motion (Fig. 1-8). Five inferred dextral strike-slip faults and one inferred sinistral strike-slip fault were also recorded (Fig. 1-9).

Conjugate strike-slip fault sets were not found in the field. When measured faults were plotted, though, conjugate relations were noted between northwest-striking sinistral strike-slip faults and northeast-striking dextral strike-slip faults.

South Spring

An area three and a half kilometers south of the southern fault tip was examined for kinematic indicators away from the Montosa fault. All the fault planes measured strike nearly due east and dip very steeply north or south (Fig. 1-9). Some show dextral strike-slip motion whereas others show sinistral strike-slip motion.

Fold Hinges

The trends of the traces of fold axial planes and fold hinges were measured in the field and from the maps of other workers (Appendix C; Wilpolt and Wanek, 1951; Myers and McKay, 1974; Myers et al., 1981; Osburn, 1983; Colpitts, 1986; Myers et al., 1986; Brown, 1987; Cabezas, 1987). Most folds studied are situated within three kilometers of the fault but a few are up to fourteen kilometers away. The majority of the fold hinges are nearly horizontal, and all are found in Pennsylvanian and Permian rocks. The fold hinge trends vary in orientation. At Abo Pass, fold hinge trends exhibit a bimodal distribution, with modes trending 025° and 070° (Fig. 1-11). By Black Mesa, the distribution is variable with two main modes trending 025° and 050°. Along the southern portion of the fault, fold hinges trend 015° and 345°, with a few exceptions. Note that the number of fold hinges measured in each area varies significantly (Fig. 1-11).

DISCUSSION

Shortening and Extension Directions

Faults and folds are expected to initiate in specific orientations to accommodate shortening in the crust, assuming that the deformed material is initially homogeneous with
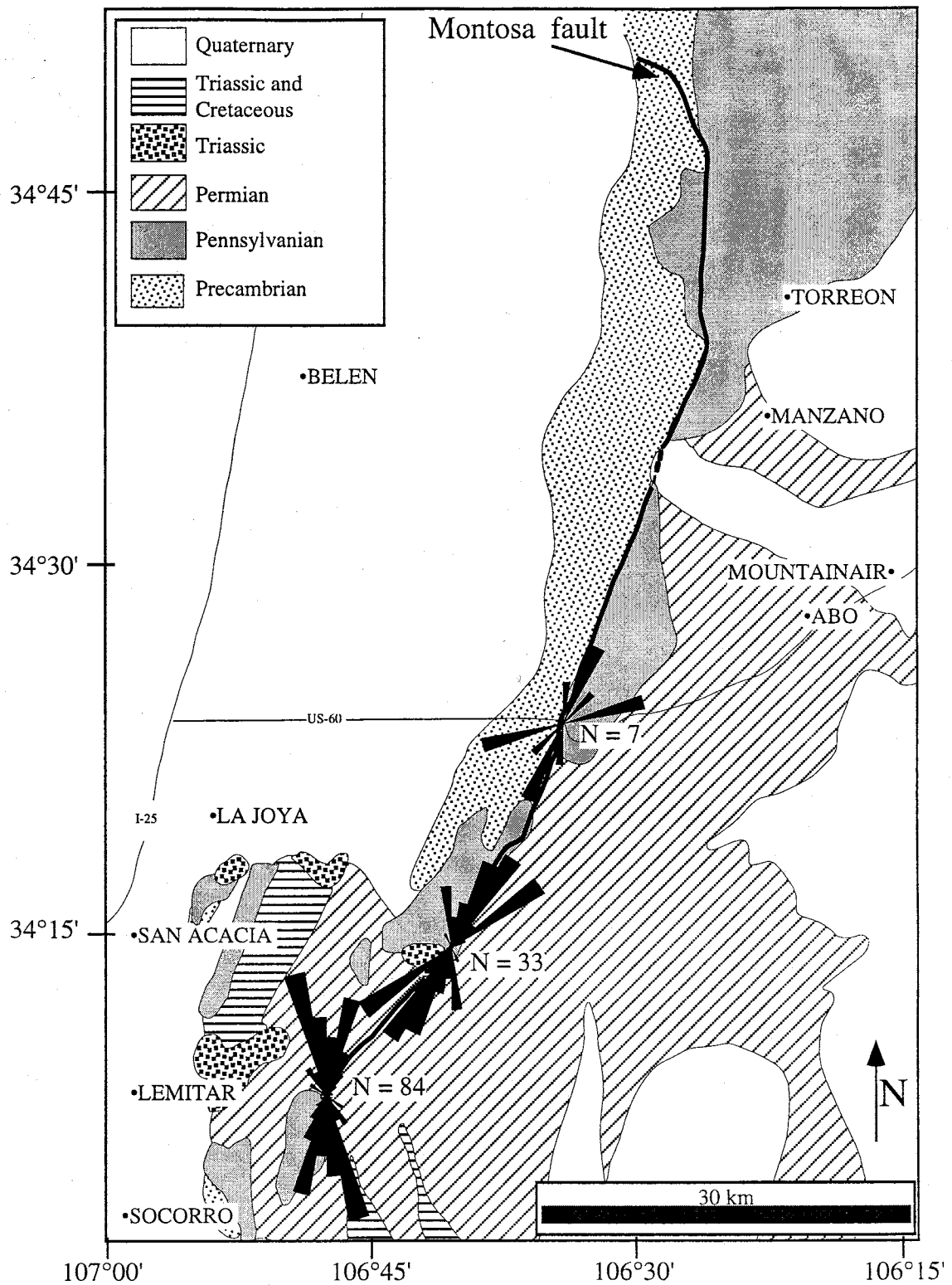
Figure 1-11. Trends of fold hinges along the fault. Note the number of fold hinges plotted in each area varies significantly. Base map from New Mexico Geological Society Map of New Mexico (1982).

no pre-existing structures or weaknesses, is lithified, and exhibits linear elastic behavior. Rocks are rarely homogeneous. Along the Montosa fault, rocks have heterogeneities including incompetent beds, bedding plane contacts, and foliations. The foliation of the Precambrian basement which also dips 55-75° west is believed to have influenced the orientation of the Montosa fault (Hayden, 1991).

Given the assumptions about deforming material listed above, the strikes of reverse faults and trends of fold hinges will initially be perpendicular to the maximum shortening direction, whereas dextral strike-slip and sinistral strike-slip faults will form at a low angle to the shortening direction (Anderson, 1951). For example, with east-west shortening, reverse faults should strike north-south and fold hinges should trend north-south. Dextral strike-slip faults would strike northeast, and sinistral strike-slip faults northwest.

It is possible to invert for the major and minor axes of the strain ellipsoid resulting from slip on a given population of faults (Michael, 1984), because incremental strain axes are oriented 45° from the fault plane (Cladouhos and Allmendinger, 1993). The inversion is based on several assumptions: 1) representative sampling of fault planes has been obtained, 2) faults were not reoriented by later tectonic events, and 3) the faults included in the analysis do not have a complex history (Marrett and Allmendinger, 1990). The direction of maximum shortening has been estimated from minor faults in the vicinity of the Montosa fault. Known kinematic indicators were processed with FaultKin v. 3.8.3 (Appendix D; Allmendinger et al., 1992) to determine shortening and extension directions (minor and major axes of the strain ellipsoid, respectively). This program uses each fault plane, lineation, and sense of slip to create a fault plane solution. The axes of shortening and extension are estimated by bisecting the angle between the nodal planes of the fault plane solution (Marrett and Allmendinger, 1990). These axes are then plotted on lower hemisphere equal area plots (e.g., Fig. 1-12).

Cross-cutting relationships observed along the Montosa fault indicate that normal motion on minor fault planes post-dates reverse and strike-slip motion on the faults.
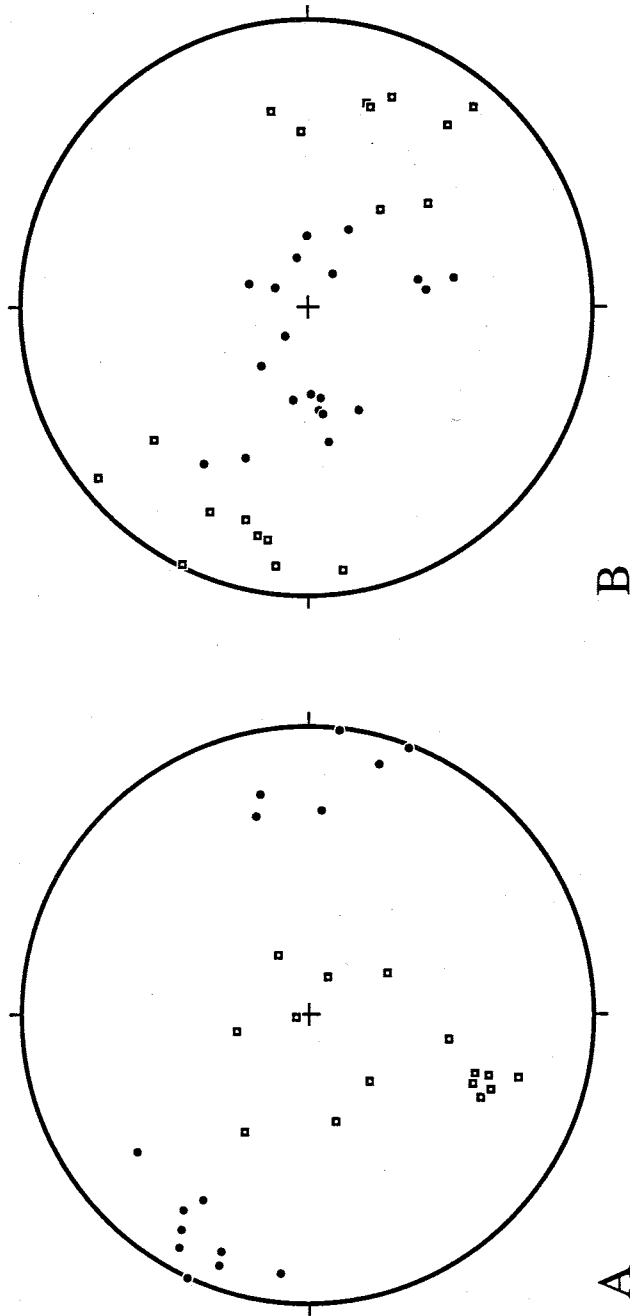
Figure 1-12. An example of output from the program FaultKin (Allmendinger, 1992). Dots are axes of maximum shortening; squares are axes of extension. A) Data from reverse and dextral fault planes from Gallina Well area, indicating west-northwest shortening. B) Shortening and extension axes from normal fault planes at Gallina Well, indicating maximum extension is west-northwest, and shortening is subvertical. These two fault systems could not have been active at the same time.

Slickenside striae on normal faults are noted to cross-cut reverse and strike-slip slickenside striae, and normal planes without cross-cutting relationships are in many places parallel to reverse and strike-slip faults in the same area. Thus, normal faults are generally interpreted as reactivated reverse and strike-slip faults. Calculated extension axes have the same orientations as shortening axes determined from combined reverse and strike-slip fault data (Fig. 1-12), indicating that reverse, strike-slip, and normal fault systems could not be active at the same time (strain incompatibility, Marrett and Allmendinger, 1990). The Montosa fault bounds the eastern edge of the Los Piños and Manzano Mountains, two eastern rift flanking ranges. As mentioned previously, a minimum of 90 meters of normal separation is recorded locally on the Montosa fault. Reactivation of minor planes is consistent with this evidence that the Montosa fault was reactivated as a normal fault. Apatite fission-track data are consistent with the interpretation that reactivation occurred during Rio Grande rift extension (Part II).

Three shortening events have been interpreted to have affected the Montosa fault, resulting in east-west, northwest-southeast, and north-south shortening (Table 1-2). Reverse and strike-slip faults at Cañon Colorado, Sand Canyon, the railway cut, and the Sais Santa Fe Quarry all record east-west shortening (Fig. 1-13). Half of the planes with known sense of slip at Gallina Well also accommodated east-west shortening. If both the sinistral and dextral strike-slip faults at South Spring were active at the same time, they would have accommodated east-west shortening. Most of the fold axes at Gallina Well and a few at Abo Pass and Black Mesa also support east-west shortening (Fig. 1-14).

Northwest-southeast shortening is interpreted based on reverse and strike-slip faults at Sand Canyon, Sais Santa Fe Quarry, the railway cut, Parker Ranch, and Gallina Well (Fig. 1-13). A few fold hinge orientations at Abo Pass and Gallina Well, in addition to a significant population at Black Mesa, also support northwest-southeast shortening (Fig. 1-14).

Shortening Direction	Supporting Evidence
East-West	Planes with known sense of slip, including: sinistral faults at Cañon Colorado, dextral faults in Precambrian rocks and a reverse plane in Pennsylvanian rocks at Sand Canyon, three sinistral strike-slip and one reverse fault in the railway cut, two reverse and six dextral strike-slip faults at Sais Santa Fe Quarry, and three reverse planes at Gallina Well. Planes with inferred sense of slip, including: two dextral planes in Pennsylvanian rocks at Sand Canyon, two reverse planes at Parker Ranch, and sinistral and dextral strike-slip and reverse planes at Gallina Well. Fold hinges, including three at Abo Pass, thirty-six at Black Mesa, and forty-five at Gallina Well.
Northwest-Southeast	Planes with known sense of slip, including: reverse, sinistral and dextral strike-slip faults in Pennsylvanian rocks at Sand Canyon and Gallina Well, three reverse faults at Sais Santa Fe Quarry, and a reverse fault at Parker Ranch. Planes with inferred sense of shear, including: dextral strike-slip faults in Precambrian rocks and reverse faults in Pennsylvanian rocks at Sand Canyon, reverse planes at the railway cut and Parker Ranch, and reverse and dextral strike-slip faults at Gallina Well. Fold hinges, including two at Abo Pass, two at Gallina Well, and fifteen at Black Mesa.
North-South	Planes with known sense of slip, including: reverse and dextral strike-slip faults at Cañon Colorado, reverse planes in Precambrian rocks and reverse, dextral, and sinistral strike-slip faults in Pennsylvanian rocks at Sand Canyon, sinistral strike-slip faults in the Sais Santa Fe Quarry, and a reverse fault at Parker Ranch. Planes with inferred sense of slip including: dextral strike-slip faults at Cañon Colorado, a dextral strike-slip fault in Pennsylvanian rocks at Sand Canyon, and reverse and dextral strike-slip faults at Parker Ranch. Fold hinges, including two at Abo Pass, one at Black Mesa, and three at Gallina Well.

Table 1-2. Supporting evidence for shortening directions determined along the Montosa fault.
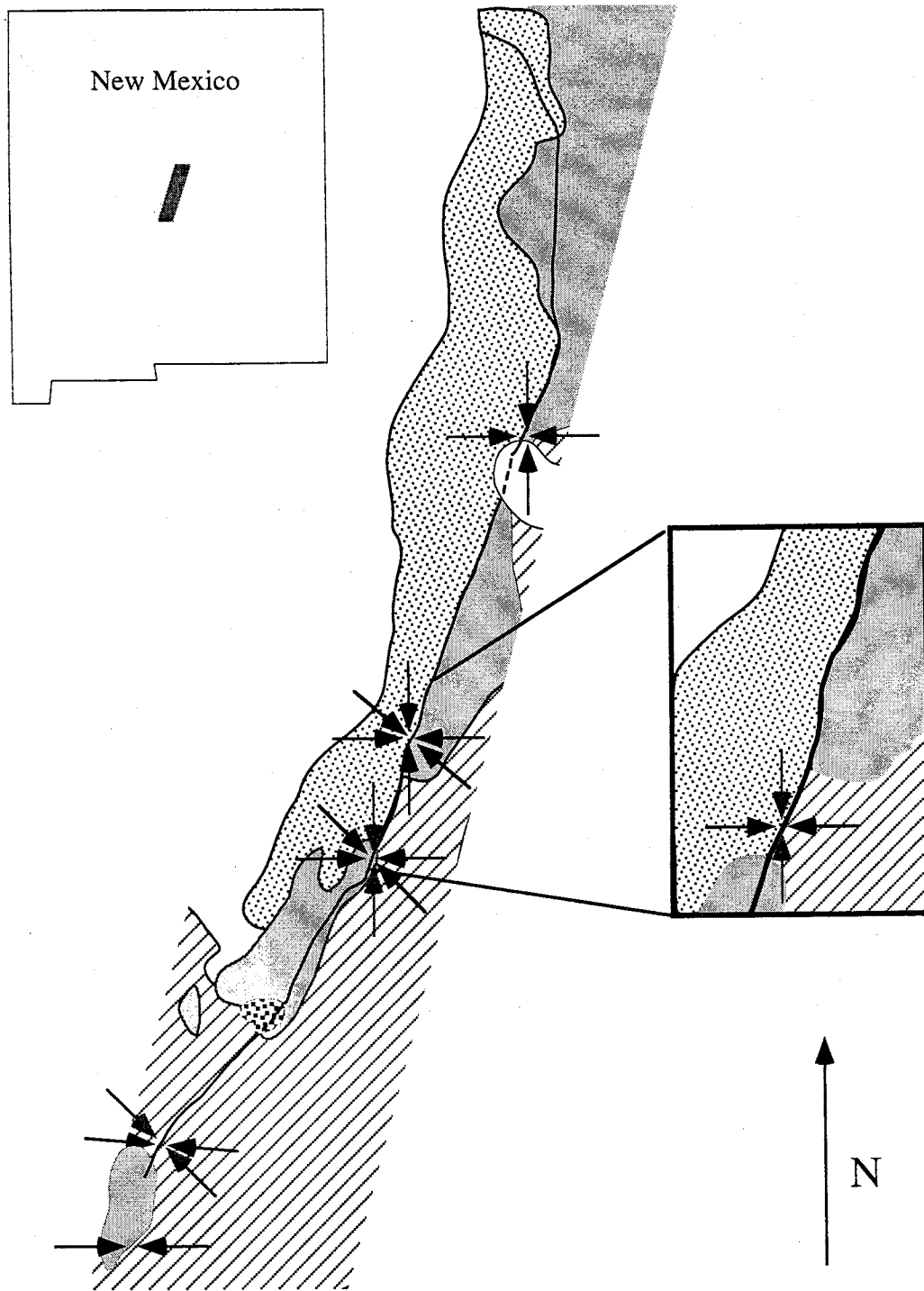
Figure 1-13. Mean directions of maximum shortening recorded by minor faults along the Montosa fault. Black arrows indicate shortening directions with strong supporting evidence. Gray arrows indicate shortening directions with less supporting evidence. Enlargement shows detail of Abo Pass area.
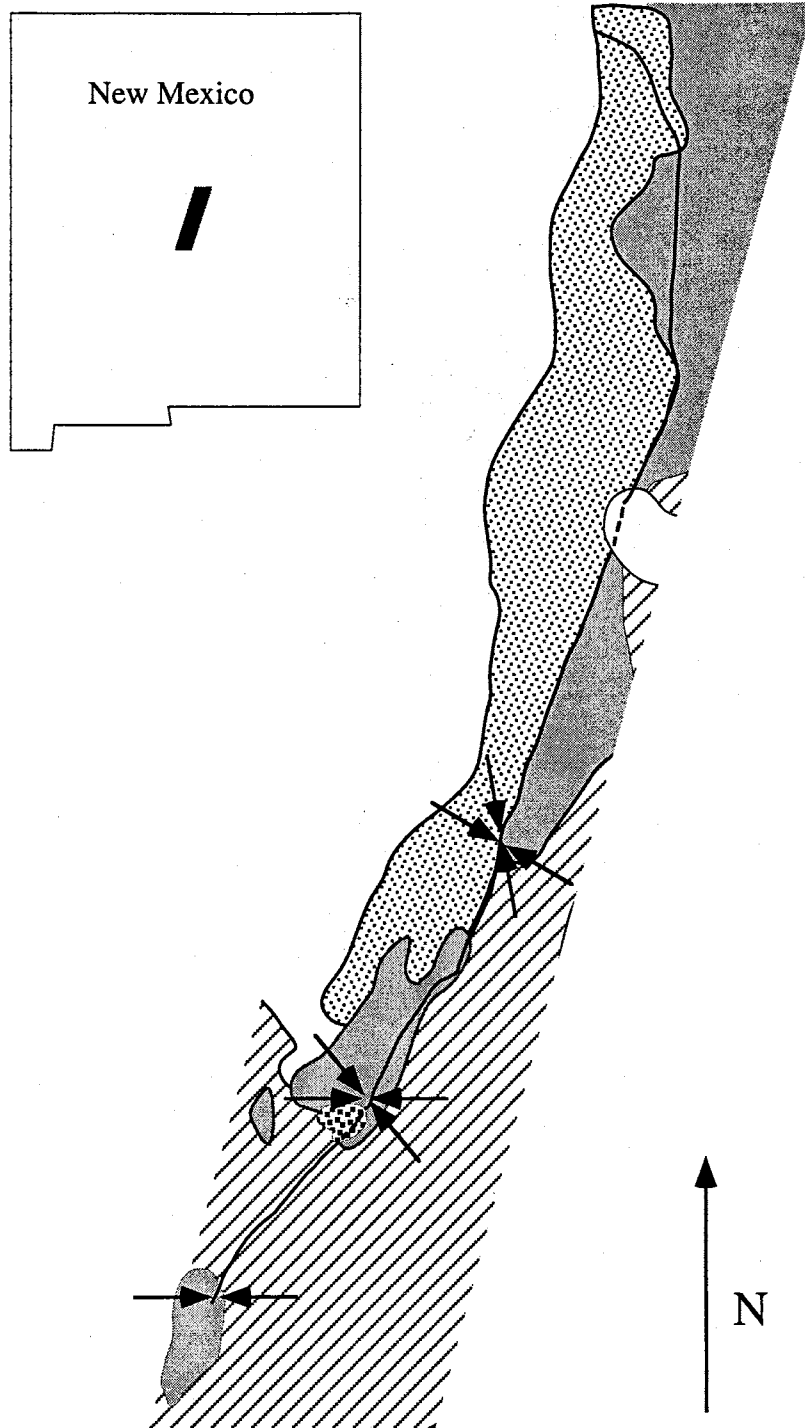
Figure 1-14. Direction of maximum shortening determined by fold hinge orientations. Axes determined from fold hinges agree with axes determined from minor fault planes.

Evidence for north-south shortening is found only along the central portion of the Montosa fault. Some reverse, dextral strike-slip and sinistral strike-slip faults in the southern Manzano Mountains and northern Los Piños Mountains, and a few folds at Abo Pass, accommodated north-south shortening (Fig. 1-13 and 1-14).

Evidence for both east-west and northwest-southeast shortening is therefore found along the whole trace of the Montosa fault that was examined, whereas evidence for north-south shortening was found only along the central portion of the fault. More planes and fold hinges were found that accommodated east-west shortening than either of the other events. No evidence was found to indicate the relative timing of the different shortening events, but other workers have found cross-cutting relationships indicating that east-west shortening predates north-south shortening (Gries, 1983; Erslev, 1998). They have determined that the east-west shortening event occurred early and the north-south late in the Laramide orogeny.

The Montosa fault would have had a different sense of slip during each of these three shortening events. If the Montosa fault, with an overall strike of N20E, was active during north-south shortening, it would have been a sinistral fault with a minor component of reverse motion (Fig. 1-15A). Evidence for north-south shortening, as indicated above, is limited to the central portion of the fault. Northwest-southeast shortening would have been accommodated by sinistral reverse motion on the fault (Fig. 1-15B). Evidence for northwest-southeast shortening is found along the whole fault but is much less common than evidence for east-west shortening (Figs. 1-8 and 1-9, Appendix D). The fault would have been a reverse fault with a component of dextral strike-slip motion if it was active during east-west shortening in the early Laramide orogeny (Fig. 1-15C). Evidence for east-west shortening is prevalent along the whole fault, including fold hinge and minor fault plane orientations, therefore the Montosa fault is largely a dextral reverse fault. This conclusion supports recent work by Cabezas (1987) and Hayden (1991) and disproves
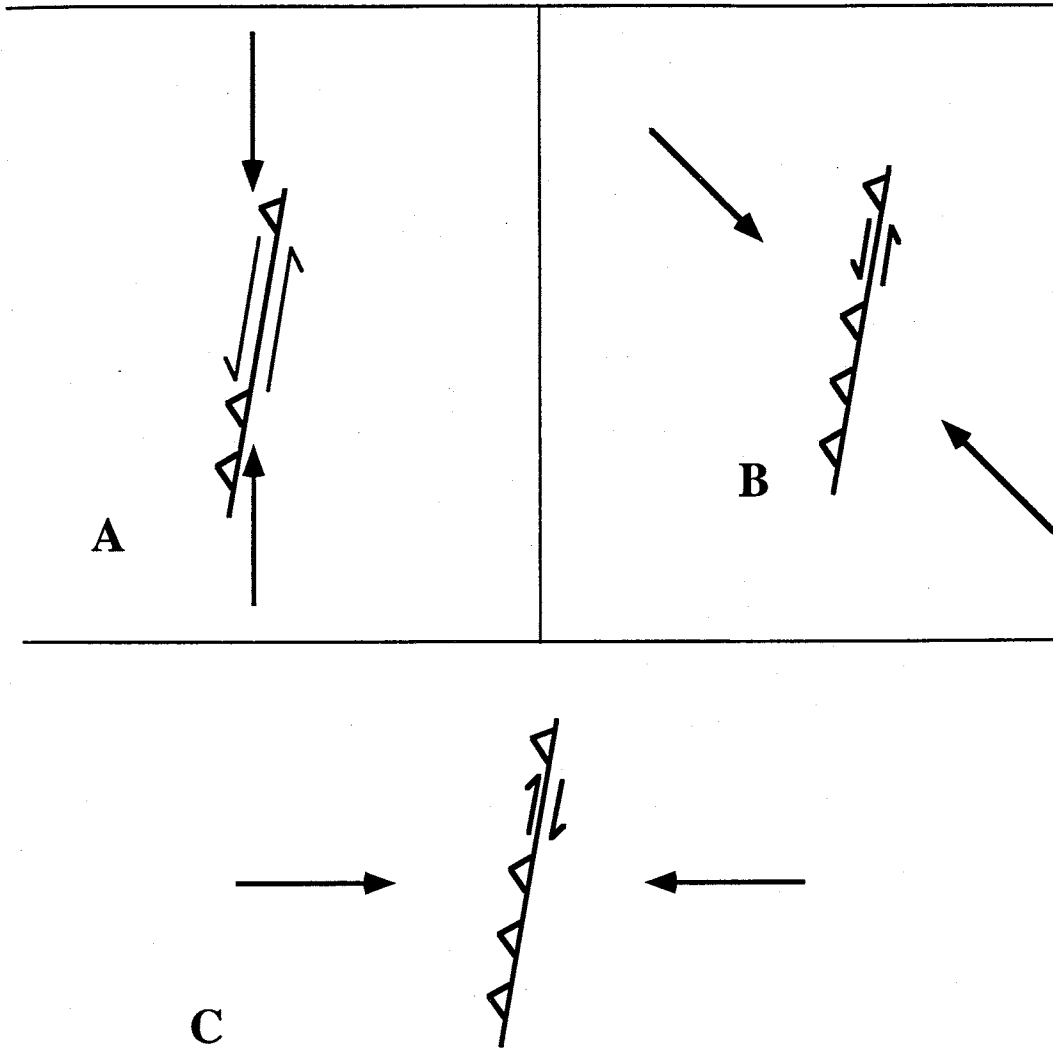
Figure 1-15. Various shortening directions determined through fault and fold analysis and associated movement on the Montosa fault. A) The Montosa fault would accommodate north-south shortening through sinistral strike-slip with minor reverse motion. B) In a northwest-southeast shortening regime, the Montosa fault would show sinistral reverse oblique-slip motion. C) The Montosa fault would accommodate east-west shortening with predominantly reverse with a minor component of dextral strike-slip motion.

earlier work by Stark and Dapples (1946), Reiches (1949), Stark (1956), and Kelley (1977).

Strain Partitioning

Homogeneous strain requires that no major discontinuity exist within a zone of deformation. Where a discontinuity is present, strain may be partitioned into wrench-dominated and pure-shear dominated components (e.g., Teyssier et al., 1995). Strain partitioning at plate margins has been studied in some detail (e.g. Mount and Suppe, 1992; Teyssier et al., 1995; Tavernelli, 1998). It has been found that the maximum instantaneous shortening direction becomes increasingly perpendicular to the plate margin as strain partitioning increases (Teyssier et al., 1995). The San Andreas fault, an active dextral transform fault at the boundary of the North American and Pacific plates, shows significant strain partitioning (95%; Teyssier et al., 1995). The angle between the plate convergence direction and the fault is 20°, but Tavernelli (1998) found folds and thrust faults which accommodated shortening perpendicular to the fault trace. These features are the result of strain partitioning, in which the shortening component of plate convergence is accommodated by small faults and folds, and the strike-slip component is accommodated by the San Andreas fault.

Borehole breakouts provide information about current stress directions. In one area, the maximum horizontal stress is oriented 25-45° from strike near the San Andreas Fault (Castillo et al., 1997), but at distances greater than 20 kilometers from the fault, the maximum horizontal stress is nearly perpendicular to fault strike (Zoback et al., 1987; Mount and Suppe, 1992). As mentioned above, the San Andreas fault zone accommodated most of the strike-slip component of plate convergence, while folds and thrust faults, some within a few kilometers of the fault, accommodated shortening (Teyssier et al., 1995; Tavernelli, 1998). This partitioning reflects a variation in the orientation of stress with proximity to the fault. These observations suggest that if one were to examine structures around a given fault to determine the direction of shortening and infer the sense of slip on

the fault, interpretations would be more accurate for structures closer to the fault. All of the minor faults examined in the analysis of the Montosa fault are situated within 300 meters of the fault itself. Most of the folds examined were within three kilometers, and a few were up to fourteen kilometers away. Because all the data were collected in the near field, it is believed that interpretations would not be affected by strain partitioning. However, the possibility of extreme strain partitioning, in which structures less than 0.5 kilometers from the fault do not record strain associated with fault motion, is considered in the following paragraphs.

If extreme strain partitioning occurred one would expect that the Montosa fault would record largely strike-slip motion and right steps in the fault would be predominantly normal. If strain partitioning did not occur along the Montosa fault, the fault itself would record largely reverse separation. Right steps in the fault would record mainly dextral strike-slip motion.

Hayden (1991) hypothesized that the fault bend at Abo pass acted as a transtensional step. Within the right steps of the Montosa fault, however, no graben structures are observed and the upturned beds in the step just south of Cerro Montoso indicate a component of reverse motion occurred in the fault step. Significant reverse motion is also recorded in stratigraphic separation along the main fault. If the Tijeras-Cañoncito fault zone, which strikes northeast and records predominantly right-lateral strike-slip motion (Abbott, 1995), was active at the same time as the Montosa fault, it supports predominantly reverse motion on the Montosa fault. This evidence suggests that extreme strain partitioning did not occur along the Montosa fault, and that both small-scale structures and large-scale structures record the same fault history.

Timing of Deformation

The possibility that the Montosa fault initiated during ancestral Rocky Mountain deformation must be considered. Ancestral Rocky Mountain tectonism took place from the latest Mississippian (Armstrong, 1962) to the Early Permian (Peterson, 1980).

In the Joyita Hills, 20 kilometers west of the Montosa fault, evidence of ancestral Rocky Mountain deformation was recorded by Beck and Johnson (1992) and Beck and Chapin (1994). They found north and northwest striking faults that record transtensional sinistral strike-slip faulting during ancestral Rocky Mountain tectonism. One subvertical fault, oriented N12E, records offset of the Sandia Formation (Atokan age) but does not cut the Madera Formation (Pennsylvanian, post-Atokan age), constraining the timing of faulting.

In the Estancia Basin, a structural basin due east of the Montosa fault, several faults have been interpreted as ancestral Rocky Mountain in age (Broadhead, 1997). North- to northeast-striking, high-angle faults are the main basin structures. These faults rarely cut the upper surface of the Abo Formation, but do offset stratigraphically lower beds, which constrains faulting to have occurred prior to the Early Permian (Wolfcampian; Table 1-1).

The Montosa fault is generally parallel to the ancestral Rocky Mountain faults at Joyita Hills and in the Estancia Basin. The timing of slip along the Montosa fault is constrained by the ages of faulted rocks and the timing of cooling recorded by apatite fission tracks. None of the rocks cut by the Montosa fault are younger than Early Permian in age. All three interpreted shortening directions are recorded in Precambrian, Pennsylvanian, and Permian rocks along the fault. Because all of the rocks present, regardless of age, record all three stages of shortening, faulting probably post-dated deposition, burial, and lithification of the Abo Formation in Early Permian (Wolfcampian) time. Faulting also predated the Oligocene according to apatite fission-track data (Part II). Together these data constrain the deformation between early Permian (Wolfcampian) and mid Tertiary (Oligocene) time. The Montosa fault therefore could have been active late in the ancestral Rocky Mountain deformation event. It is more likely, given the multi-stage history recorded by structures in the area, that deformation initiated during the Laramide orogeny.

Understanding the deformation history of the Montosa fault contributes to a better understanding of Laramide deformation in New Mexico. As mentioned in the introduction,

one school of thought is that the magnitude of dextral strike-slip separation across New Mexico is limited to less than 20 kilometers (Woodward et al., 1997; Lucas, 1997). The other school of thought is that more than 60 kilometers of offset occurred (Karlstrom and Daniel, 1993; Cather, 1997). The Montosa fault was hypothesized to be part of a dextral strike-slip shear system that included the Picuris-Pecos fault, with the Tijeras-Cañoncito fault zone acting as a transtensional step (Cather, 1992; Fig. 1-2). Evidence found in this study supports a component of unknown magnitude of dextral motion on the Montosa fault. This study neither supports nor refutes the hypothesis of a large magnitude of dextral displacement on faults across New Mexico.

CONCLUSIONS

1. A minimum of 600 meters of thrust separation exists along the central portion of the Montosa fault.

2. Slickensides with slickenside striae and slickenfibers and fold hinges indicate multi-stage Laramide deformation, with the direction of shortening along the Montosa fault ranging from east-west, to northwest-southeast, to north-south. The prevalence of minor fault and fold hinges along the fault which accommodated east-west shortening indicates that east-west shortening resulted in the greatest deformation along the Montosa fault.

3. The Montosa fault was a reverse fault with a component of dextral oblique-slip motion.

4. Normal reactivation of minor fault planes and at least of 90 meters of normal motion recorded in vertical separation across the fault by Black Mesa, indicate that at least part of the Montosa fault was reactivated during Rio Grande rift extension.

PART II: APATITE FISSION-TRACK THERMOCHRONOLOGICAL CONSTRAINTS ON THE MOVEMENT HISTORY OF THE MONTOSA FAULT, CENTRAL NEW MEXICO.

INTRODUCTION

The Montosa fault is a 90 kilometer long, north-northeast striking fault which bounds the east side of the Manzano and Los Piños Mountains of central New Mexico (Fig. 2-1). The west-dipping Montosa fault shows predominantly reverse separation, with Proterozoic schist, quartzite, and gneiss of the hanging wall juxtaposed against Late Paleozoic sandstone, mudstone, limestone, and conglomerate of the footwall (Fig. 2-2). Minor structures along the fault record a minor component of right-lateral strike-slip motion (Part I). The Montosa fault was formed during the Laramide orogeny and reactivated as a normal fault during late Oligocene to Recent Rio Grande rift extension (Part I).

The Montosa fault is located in a complex terrane that experienced shortening during the Laramide orogeny and extension during Rio Grande rift formation. The Laramide orogeny lasted from Late Cretaceous to early Tertiary time, and several workers believe it was the result of shallow subduction of the Farallon plate beneath the North American plate (e.g. Lowell, 1974; Keith, 1978; Chapin, 1983). In central and northern New Mexico, shortening was accommodated by the formation of several northerly striking faults, including the Nacimiento fault in the Nacimiento Mountains, and the Picuris-Pecos fault, located in the Sangre de Cristo Mountains (Baltz, 1967; Bauer and Ralser, 1995; Fig. 2-3). The Montosa fault represents the farthest eastern extent of significant reverse faulting associated with the Laramide orogeny in central New Mexico (Kelley, 1982).

The Laramide orogeny was followed by the formation of the Rio Grande rift. The Montosa fault bounds the eastern edge of the Manzano and Los Piños Mountains, which define the eastern flank of the Rio Grande rift (Chapin, 1971; Kelley et al., 1992). Early rift formation (30-18 Ma) was characterized by broad, shallow basins, low topographic relief, and extrusive silicic ash flow tuffs and basaltic andesite lavas. Late-phase, rift-
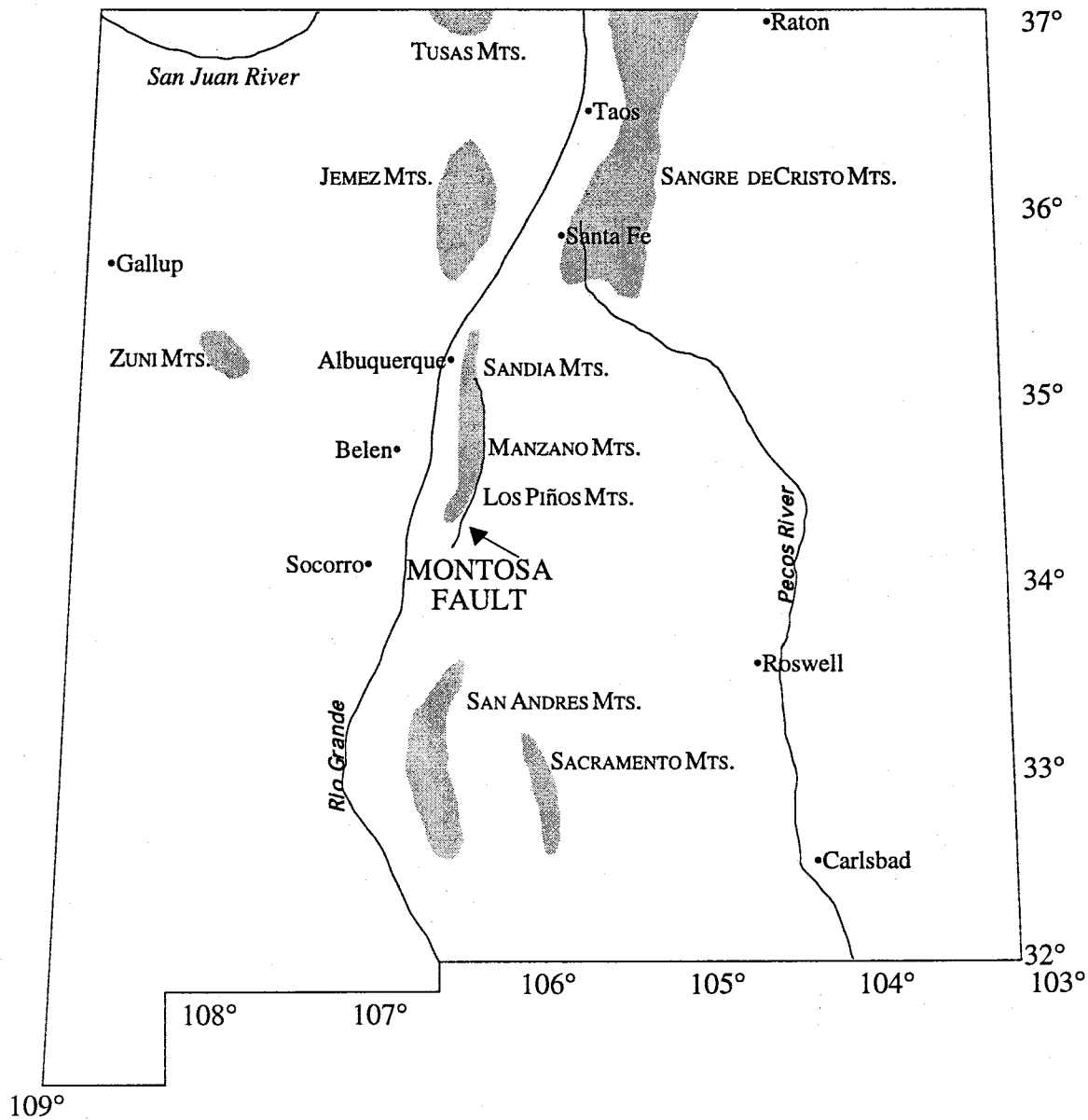
Figure 2-1. The Montosa fault bounds the Manzano and Los Piños Mountains of central New Mexico. After Stark (1956).
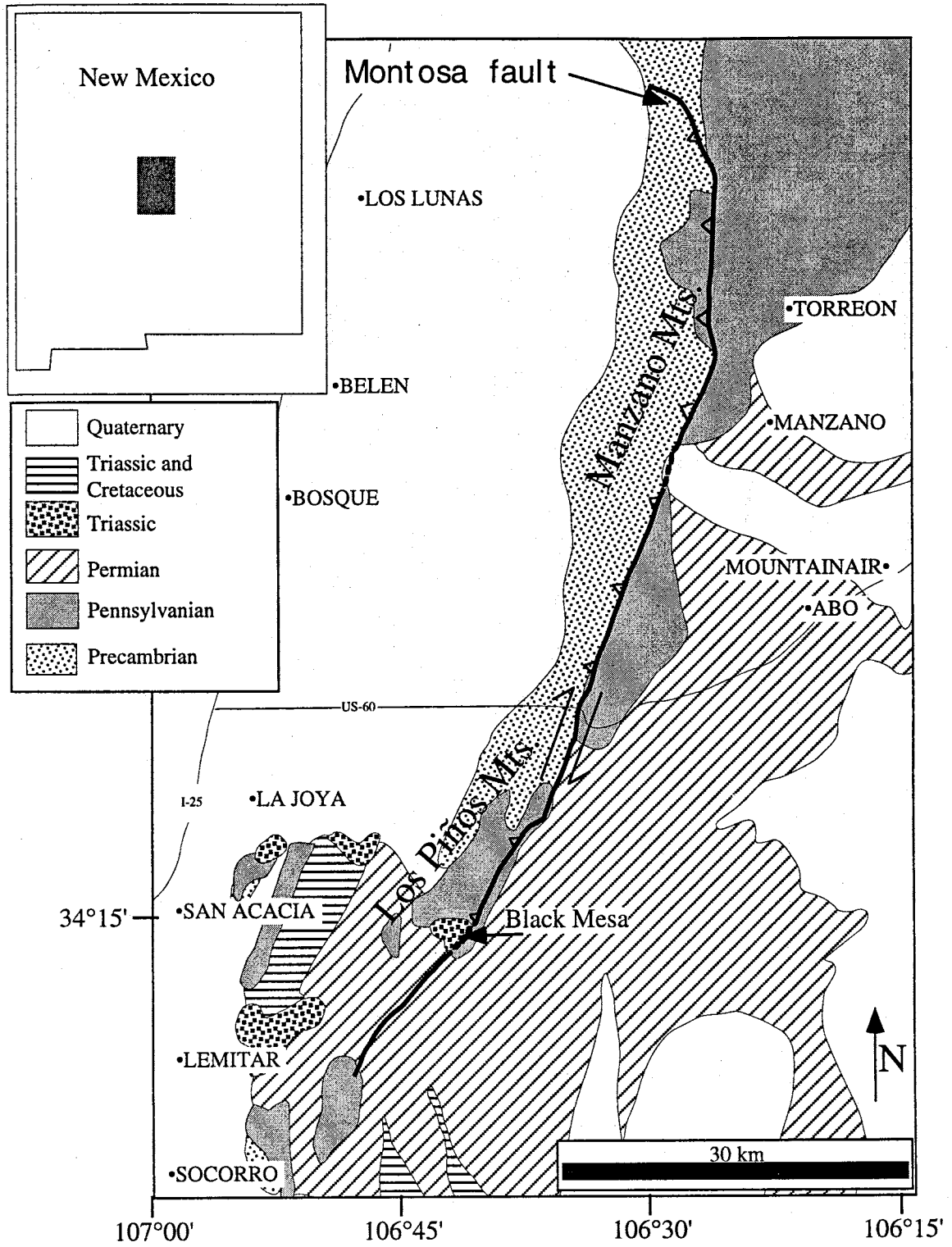
Figure 2-2. The west-dipping Montosa fault and surrounding area. Location of study area shown in upper left corner. Base map from New Mexico Geological Society Map of New Mexico (1982).
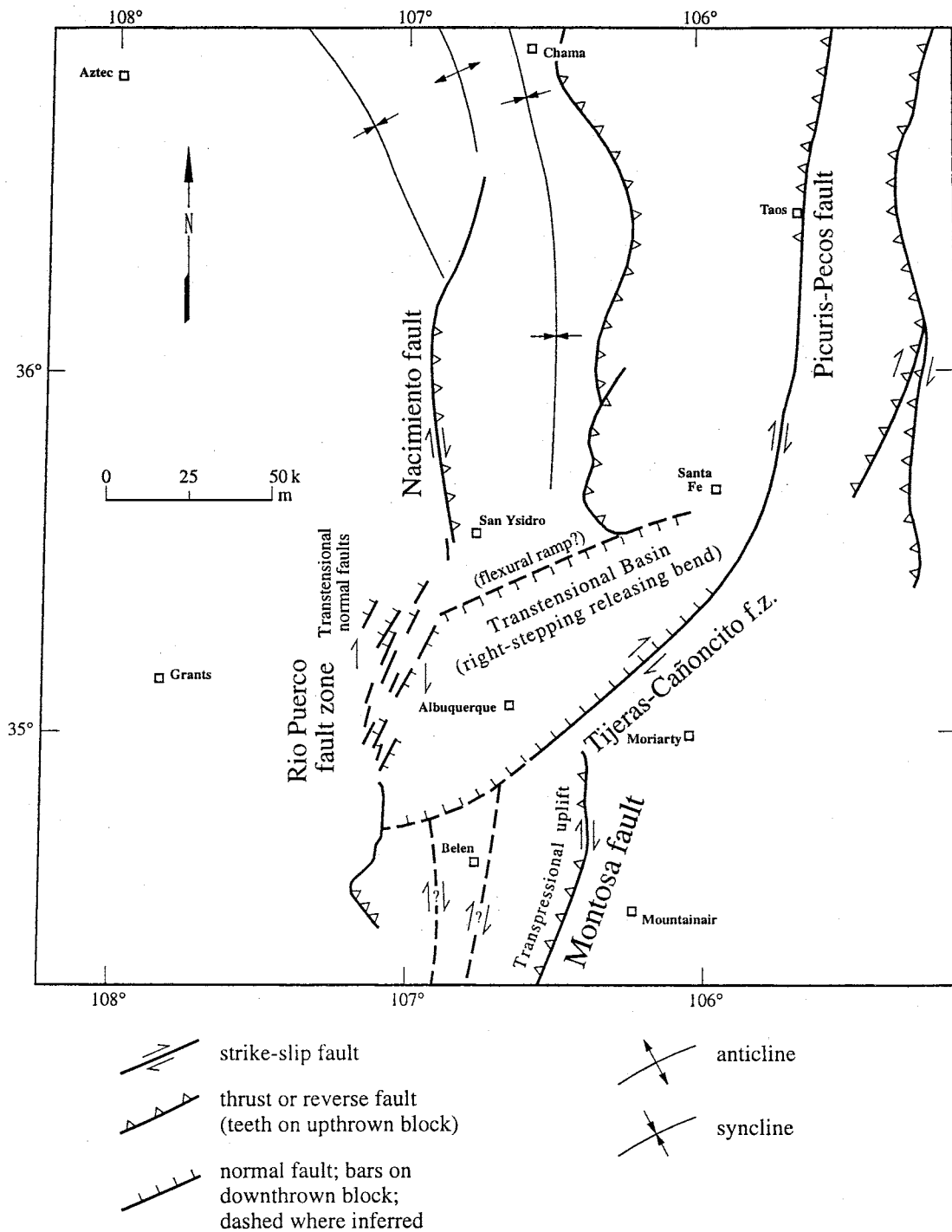
Figure 2-3. Laramide age faults and structures in northern and central New Mexico. Map and movement sense interpretations from Cather (1992).

related extension (16-7 Ma) was characterized by the formation of deep half-grabens, great topographic relief, and emplacement of alkali-olivine and tholeiitic basalts.

Because apatite fission tracks (AFT) are sensitive to temperatures in the range of 60-120°C, AFT thermochronology is useful in constraining low-temperature thermal histories (Wagner, 1968; Naeser and Faul, 1969; Wagner, 1972). Fission tracks form due to the spontaneous decay of U^{238} in the apatite crystal lattice. By determining the uranium daughter (spontaneous tracks)-parent (induced tracks) ratios, an age that indicates when the sample cooled through the AFT closure temperature can be assigned. If a sample cooled relatively slowly, the fission tracks will be short (8-13μm) due to partial annealing, but if a sample cooled rapidly the tracks will be longer (13-15μm). Track-length data, therefore, can be used to constrain complex thermal histories related to denudation or thermal reheating events. The tectonic history can be constrained by the thermal history.

By examining AFT ages of samples from equal elevations on either side of the Montosa fault, fault motion and timing of faulting with respect to cooling below 60-120°C has been determined. This approach has been successfully applied previously in several other areas. For example, AFT thermochronology was used to constrain the timing of fault movement on the Vesle Fiord Thrust in the Canadian Arctic Archipelago (Arne et al., 1998) and the Bullfrog Hills and Bare Mountain area detachment faults of southwest Nevada (Hoisch et al., 1997). This method was also used to constrain timing of faulting during the Laramide orogeny in Colorado and New Mexico (Abbott, 1995; Kelley and Chapin, 1997).

AFT ages of samples along the Montosa fault are used to constrain the timing of cooling and faulting relative to cooling of the lower elevations of the Manzano and Los Piños Mountains. In this paper, I examine previous AFT analyses from the Los Piños and Manzano Mountains, as well as AFT ages, track lengths, and tectonic histories of sample transects across the Montosa fault. These data will be integrated in an evaluation of the thermal history of the Montosa fault and its tectonic significance.

PREVIOUS WORK

Previous fission-track work in the Los Piños and Manzano Mountains was regional in extent and focused on constraining the cooling histories of the Rio Grande rift flank mountain ranges (Kelley et al., 1992). AFT data determined that the various ranges and fault blocks cooled in "complex spatial and temporal patterns" with different ranges cooling during early and late Laramide orogeny in addition to early, and late, Rio Grande rift formation (Kelley et al., 1992). The Los Piños and Manzano Mountains revealed an AFT record of Laramide uplift and Eocene erosion, as well as early stages of extension associated with development of the Rio Grande rift (Kelley et al., 1992; Fig. 2-4). Higher elevations within the Manzano Mountains record cooling from 47±7 Ma to 29±3 Ma which suggests cooling during Laramide uplift and subsequent, late Eocene- early Oligocene erosion. Samples from the lower elevations within the Manzano Mountains reflect the early stages of Rio Grande rift formation, but the AFT ages have large margins of error due to low apatite and uranium content. The apatite fission-track ages of an age-elevation transect in the Los Piños Mountains range from 44±7 to 60±20 Ma indicating that cooling occurred during Laramide uplift and subsequent Eocene erosion.

INTERPRETING FISSION-TRACK DATA

Fission track stability depends on time, temperature, and chlorine-fluorine ratios within the apatite crystals (Gleadow and Duddy, 1981; Green et al., 1985; Green et al., 1986; Wagner and Van Den Haute, 1992). When fission tracks initially form they are about 16.5 μm long (Wagner and Van Den Haute, 1992). At temperatures above 120°C, tracks form but anneal quickly and therefore are not retained. The partial annealing zone (PAZ), a zone of partial stability in which some tracks are retained, ranges from about 120 to 60°C (Gleadow and Duddy, 1981). Within the PAZ, tracks shorten through partial
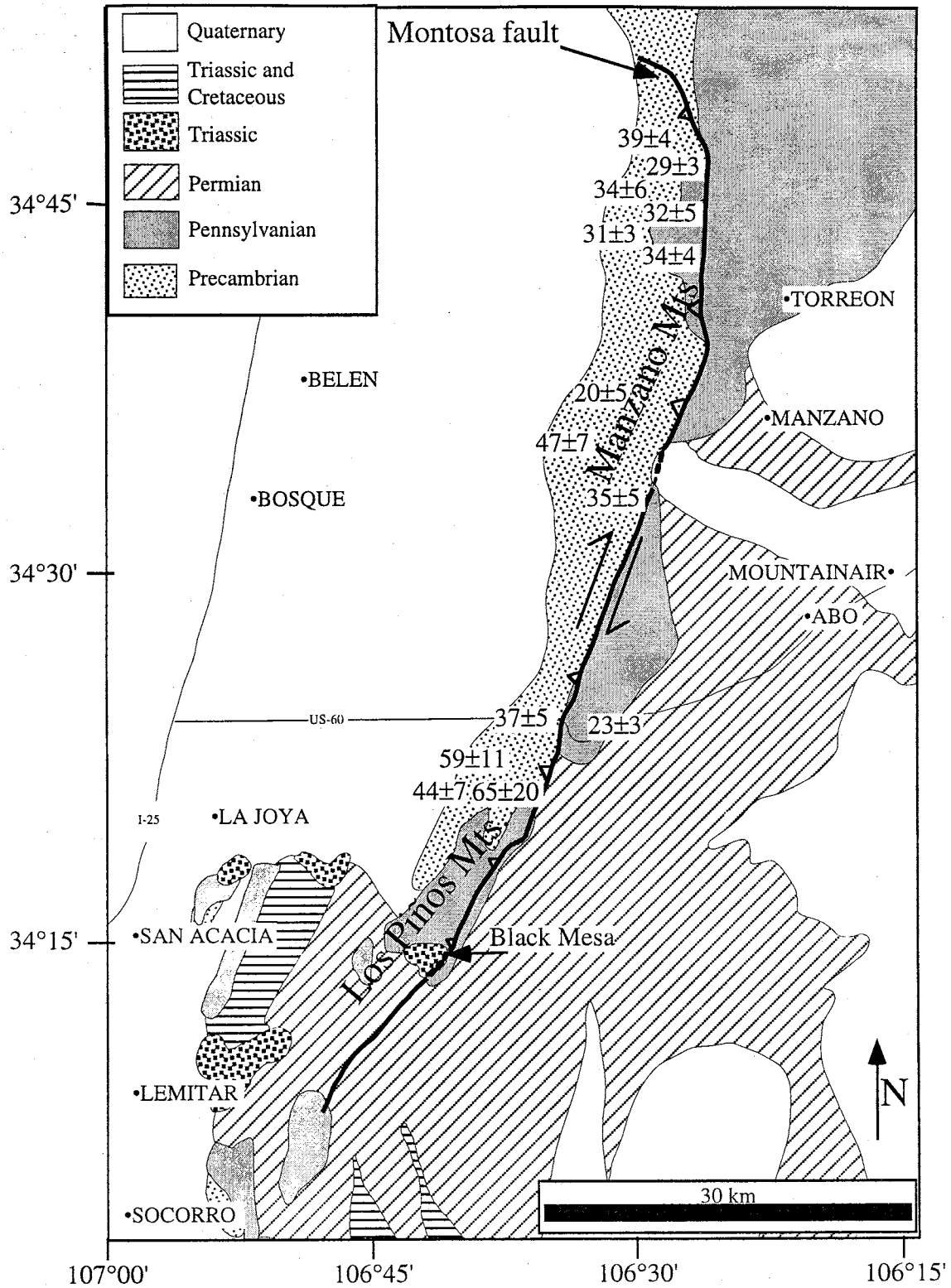
Figure 2-4. Previous apatite fission-track ages determined in the Los Piños and Manzano Mountains. Ages are in millions of years. Data from Kelley et al. (1992). Base map after New Mexico Geological Society Map of New Mexico (1982).

annealing. Below 60°C, annealing is minor, hence tracks are largely retained. The age and track-length distribution of a population of fission tracks from a given sample can be measured and used to determine a qualitative thermal history for that sample (Naeser, 1979). Fission track age is usually correlated with elevation. Because rocks at higher elevations passed through the PAZ and cooled before those at lower elevations, rocks from higher elevations should record older ages.

Surface uplift, an increase in a rock's elevation with respect to sea level, does not necessarily result in cooling, but uplift combined with denudation does. Tectonic denudation can cause rapid cooling by fault removal of overlying rock. Erosion, removal of a heat source, a decrease in the geothermal gradient, and/or the cessation of a hydrothermal system will also result in cooling. The timing of these events is recorded by apatite fission tracks, which can then be used to constrain the tectonic history.

A sample age and track-length distribution can be used to determine a qualitative thermal history. Tracks that are induced in a reactor have a mean length of 16.3±0.9 μm and the track-length distribution will be narrow and symmetrical (Gleadow et al., 1986), whereas a sample that experienced slow cooling through the PAZ will have an average track length of 13-14 μm and track-length distribution will be skewed towards longer tracks (Fig. 2-5a; Gleadow et al., 1986). Tracks will average 14-15.5 μm long with a unimodal, symmetrical track-length distribution in a sample which cooled quickly (Fig. 2-5b). Where a sample remained in the PAZ for tens of millions of years the track-length distribution will be broad and multimodal with an average track length of 10-12 μm (Fig. 2-5c). If a sample experienced a mild reheating event, it will give a mixed age, reflecting neither the heating nor the cooling event (Fig. 2-5d). Short pulses of heat will not completely erase previous tracks, but will significantly shorten them. Track-length distribution will be bimodal with shorter tracks forming before, and shortening during, a thermal event, and longer tracks forming after the event (Fig. 2-5d). The time-temperature
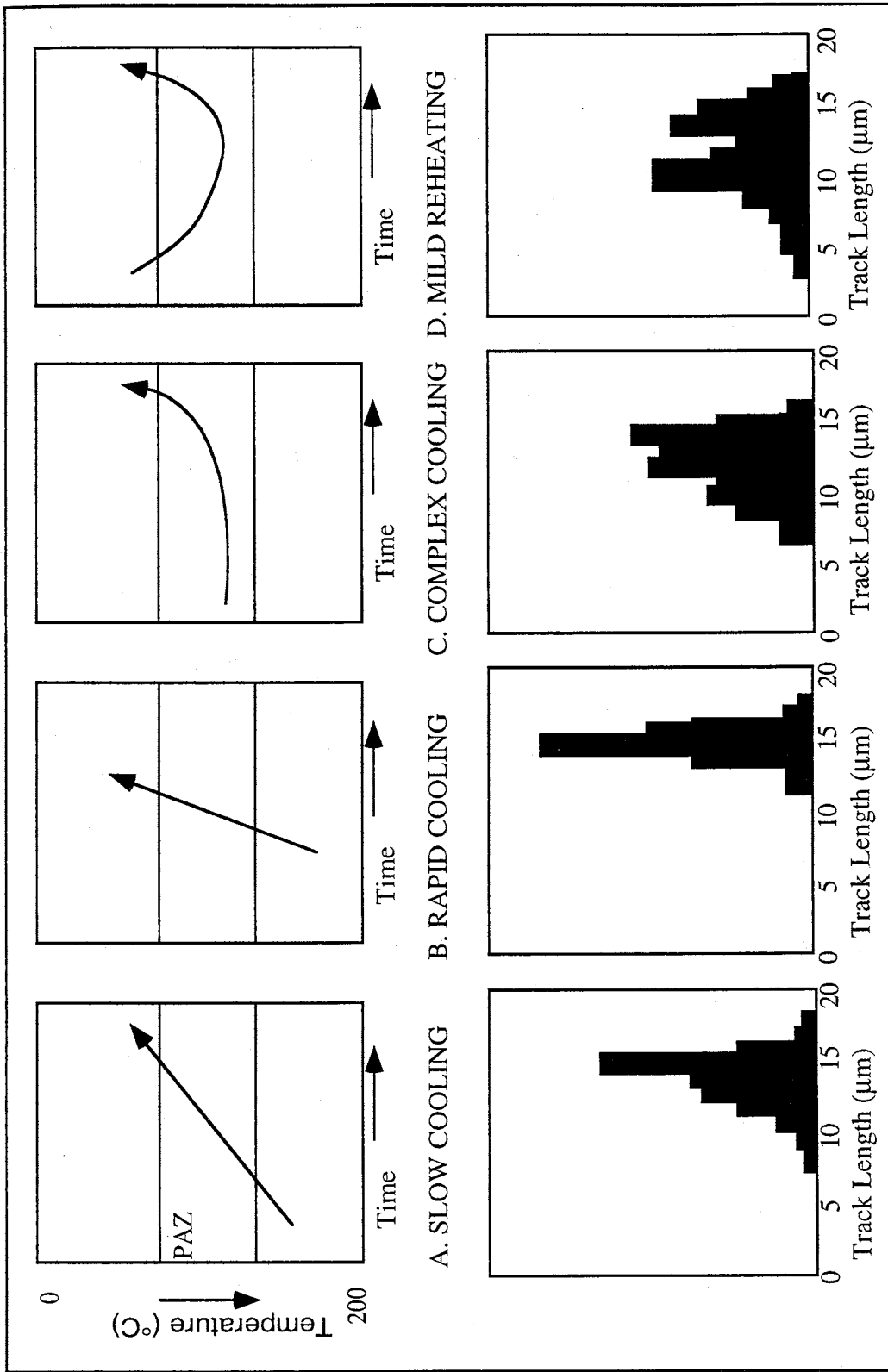
Figure 2-5. AFT time-temperature curves and track length distributions. See text for explanation. After Kelley (1990).

curve can therefore be used to constrain the tectonic history of a sample based on the timing and rate of cooling and reheating events.

Quantitative models have been developed to create potential temperature histories using AFT track-length and age data. AFT annealing experiments have been conducted in the laboratory and then projected to geologic time scales (Green et al., 1986; Laslett et al., 1987; Duddy et al., 1988; Green, 1988; Green et al., 1988). Mathematical formulations were also used to examine the behavior of fission-track annealing (e.g. Laslett et al., 1987). Models were tested and successfully verified against other methods of dating.

PROCEDURES

Twenty samples of conglomerate, sandstone, quartzite, granite, and greenstone were collected in eight transects across the fault (Fig. 2-6). Samples were crushed, and apatite was separated using standard heavy liquid and magnetic techniques. Apatite grains were mounted on glass slides with epoxy, polished, and etched for 25 seconds in a 5M solution of nitric acid. Muscovite detectors, which are used for induced track counts in the external detector method, were attached to each grain mount (Hurford and Green, 1983). Samples were assembled in a reactor package with Durango apatite (accepted age: 31.4 ± 0.5 Ma) and Corning glass (CN 6) standards and irradiated at the nuclear reactor at Texas A&M University.

Glass standards were counted to determine the neutron fluence in the reactor. Durango apatite standards were used to calculate zeta, a correction factor that takes into account fluence, procedures, and analyst observation skills (Hurford and Green, 1982; Hurford and Green, 1983). Ages for each sample were determined using the grain by grain method where the number of spontaneous and induced fission tracks are counted to determine the uranium parent-daughter ratio (Galbraith, 1984; Galbraith and Laslett, 1985). Errors in age were determined using the methods of Galbraith (1984) and Galbraith and
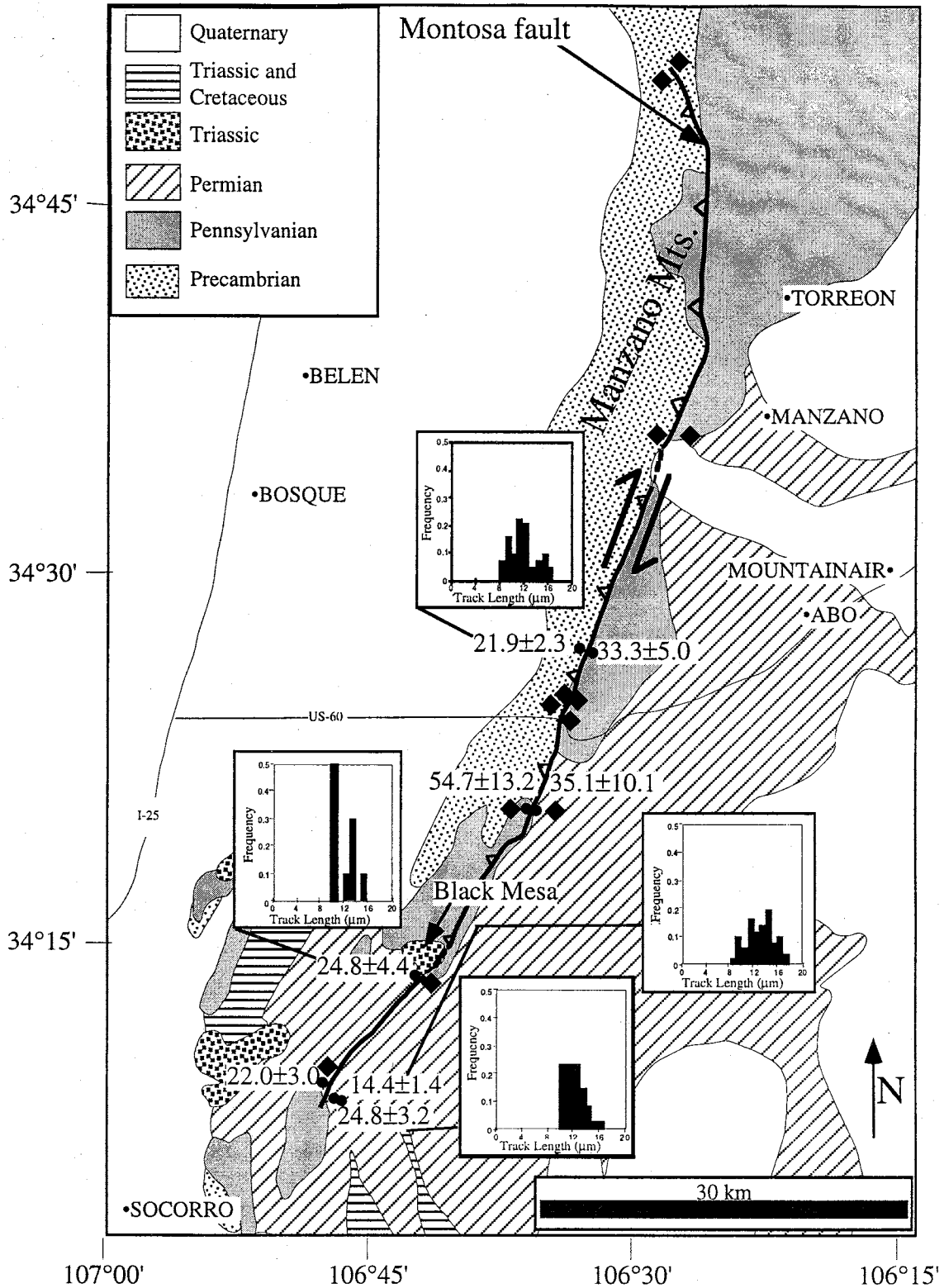
Figure 2-6. AFT ages and track length distributions of samples along the Montosa fault. Locations of samples with no apatite are shown with black diamonds. Ages are in millions of years. Base map after New Mexico Geological Society Map of New Mexico (1982).

Laslett (1985). All samples passed the chi squared test, which indicates that only one grain population exists in each sample (Galbraith, 1981; Green, 1981).

Track-length distributions were determined using a microscope with 100x dry objective, drawing tube, and digitizing tablet. Only horizontal, well etched, confined tracks were measured.

Apatite fission-track ages and track-length distributions can be modeled to give a quantitative time-temperature curve. Where significant numbers of confined tracks were measured, AFTSolve© forward and inverse computer models were used to create time-temperature curves compatible with observed age and track lengths (Donelick et al., in review).

DATA

Of the twenty samples collected, eight contained adequate apatite to date (Appendix E). In the southern Manzano Mountains, two samples collected within three meters of the fault on the hanging wall and footwall, respectively, gave an age range of 33±5 (1 standard error) to 22±2 Ma (Samples 97PT1 and 97PT2; Table 2-1; Fig 2-6). Significant numbers of apatite grains in the Priest pluton of the hanging wall made dating easy (Sample 97PT2). The footwall Sandia sandstone sample contained 13 grains with sufficient tracks to date (Sample 97PT1). Four samples were collected on an age-elevation traverse from Cerro Montoso across the Montosa fault in the northern Los Piños Mountains. Two of these contained sufficient grains to date and gave ages of 55±13 and 35±10 Ma (Samples 97CM2 and 97CM3, Table 2-1). Low uranium and apatite content made dating these two samples (97CM2, 97CM3) difficult and consequently the errors are quite large. A sample transect across the fault south of Black Mesa yielded one sample on the hanging wall with sufficient apatite to date (97BW2, Table 2-1), which gave an AFT age of 25±4 Ma. Three datable samples, collected at the southern fault tip, yielded an age range of 14-25 Ma (97GW1, 97GW2, and 97GW3, Table 2-1). In transects with samples on both sides of

Table 2-1. Apatite fission-track data from the Los Pinos and Manzano Mountains.

Sample Number	Rock Type	Latitude Longitude	Elevation (m)	Number of Grains Dated	ρ_s x10^5 t/cm^2	ρ_i x10^6 t/cm^2	ρ_d x10^5 t/cm^2	Central Age (Ma) (±1 S.E.)	P(χ)^2 (%)	Uranium Content (ppm)	Mean Track Length (μm) (±1 S.E.)	Standard Deviation Track Length
97PT1	Penn. Sandia sandstone	34°29'50" 106°28'16"	1975	13	1.1 (53)	2.4 (575)	1.484 (4600)	33.3 ± 5.0*	99	19		
97PT2	Proterozoic Priest Granite	34°29'50" 106°28'16"	1975	20	1.12 (81)	3.33 (1198)	1.493 (4600)	24.6 ± 3.0*	40	26		
				29	0.78 (95)	1.66 (2003)	1.7	21.9 ± 2.3#	43	17	12.0 ± 0.6 (44)	2.2
97CM2	Proterozoic Blue Springs schist	34°21'23" 106°31'43"	1975	20	0.43 (20)	0.57 (134)	1.508 (4600)	54.7 ± 13.2*	99	4.4		
97CM3	Permian Abo fine sandstone	34°21'49" 106°31'19"	1960	9	1.69 (26)	2.97 (228)	1.47 (4600)	40.8 ± 8.6*	30	24		
				8	0.62 (13)	0.82 (171)	1.7	35.1 ± 10.1#	52	8		
97BW2	Permian Yeso conglomerate	34°13'04" 106°37'50"	1765	20	0.46 (31)	1.12 (379)	1.436 (4600)	28.6 ± 5.4*	93	9		
				20	0.5 (34)	0.93 (634)	1.7	24.8 ± 4.4#	88	9	12.0 ± 1.3 (10)	2.0
97GW1	Permian Bernal fine sandstone	34°09'10" 106°41'52"	1730	20	1.52 (74)	4.69 (1141)	1.569 (4600)	24.8 ± 3.2*	96	35	12.3 ± 0.6 (34)	1.6
97GW2	Permian Bernal arkose	34°09'12" 106°41'50"	1710	20	1.03 (112)	4.71 (2564)	1.559 (4600)	16.6 ± 1.8*	85	36	13.1 ± 0.6 (51)	2.3
				26	0.693 (134)	2.38 (4276)	1.7	14.4 ± 1.4#	99	26		
97GW3	Permian Abo mud peb. Cong.	34°09'28" 106°42'41"	1710	20	1.16 (63)	3.96 (1078)	1.545 (4600)	22.0 ± 3.0*	80	30		

ρ_s - spontaneous track density

Number in parenthesis is the number of tracks counted for ages and fluence calibration or the number of track measured for lengths.

ρ_d - track density in muscovite detector covering CN-6 (1.05 ppm); Reported value determined from interpolation of values for detectors covering standards at the top and bottom of the reactor packages (fluence gradient correction)

ρ_i - induced track density (reported induced track density is twice the measured density)

S.E. = standard error   P(χ)^2 = Chi-squared probability   N.D. = no data

$\lambda_f = 1.551 \times 10^{-10}$ yr^{-1}, g=0.5   * analyst SK; zeta = 4882.3 ± 307 for apatite   # analyst RB; zeta = 5420

Mean track lengths not corrected for length bias (Laslett and others, 1982)

the fault, ages on either side were the same within error (Fig. 2-6). The samples from the Manzano Mountains yielded AFT ages indicative of cooling in early Oligocene to early Miocene time. AFT ages from the northern and central Los Piños Mountains indicate cooling in early Eocene to Oligocene time. The samples from the southern Los Piños Mountains were located in a region of broad valleys, mesas, and cuestas. They record more recent cooling, in late Oligocene to mid-Miocene.

Track lengths were measured in four samples (97GW1, 97GW2, 97BW2, and 97PT2; Fig. 2-6). These samples show broad and multimodal track-length distributions, with significant populations of shorter tracks. Ten confined tracks were measured in sample 97BW2 with a mean track length of 12.0 ± 2.0 μm, which is nearly identical to the mean track length of the forty-four confined tracks measured in 97PT2. The two samples collected at the southern tip of the fault have slightly longer mean track lengths. Thirty four confined tracks measured in 97GW1 have a mean track length of 12.3 ± 1.6 μm, and fifty-one measured in 97GW2 have a mean track length of 13.1 ± 2.3 μm.

DISCUSSION

AFT dates of rocks of nearly equal elevations across the Montosa fault can be used to determine if faulting predated or postdated cooling below the closure temperature. If faulting postdated cooling, there would be a significant age difference across the fault (Fig. 2-7A). A thrust fault that postdated cooling would have a hanging wall with a younger age than the footwall, because the thrust would have brought up hanging wall rocks with younger AFT ages. If faulting predated cooling, there would be no significant age difference across the fault in rocks at equal elevations (Fig. 2-7B). This is because faulting would have occurred when samples were at depths below the base of the PAZ, followed by cooling due to uplift and denudation. In this case, samples at the same elevation on both sides of the fault would pass through the PAZ at the same time and have the same age. If vertical motion on the fault was not significant, there would not be a significant
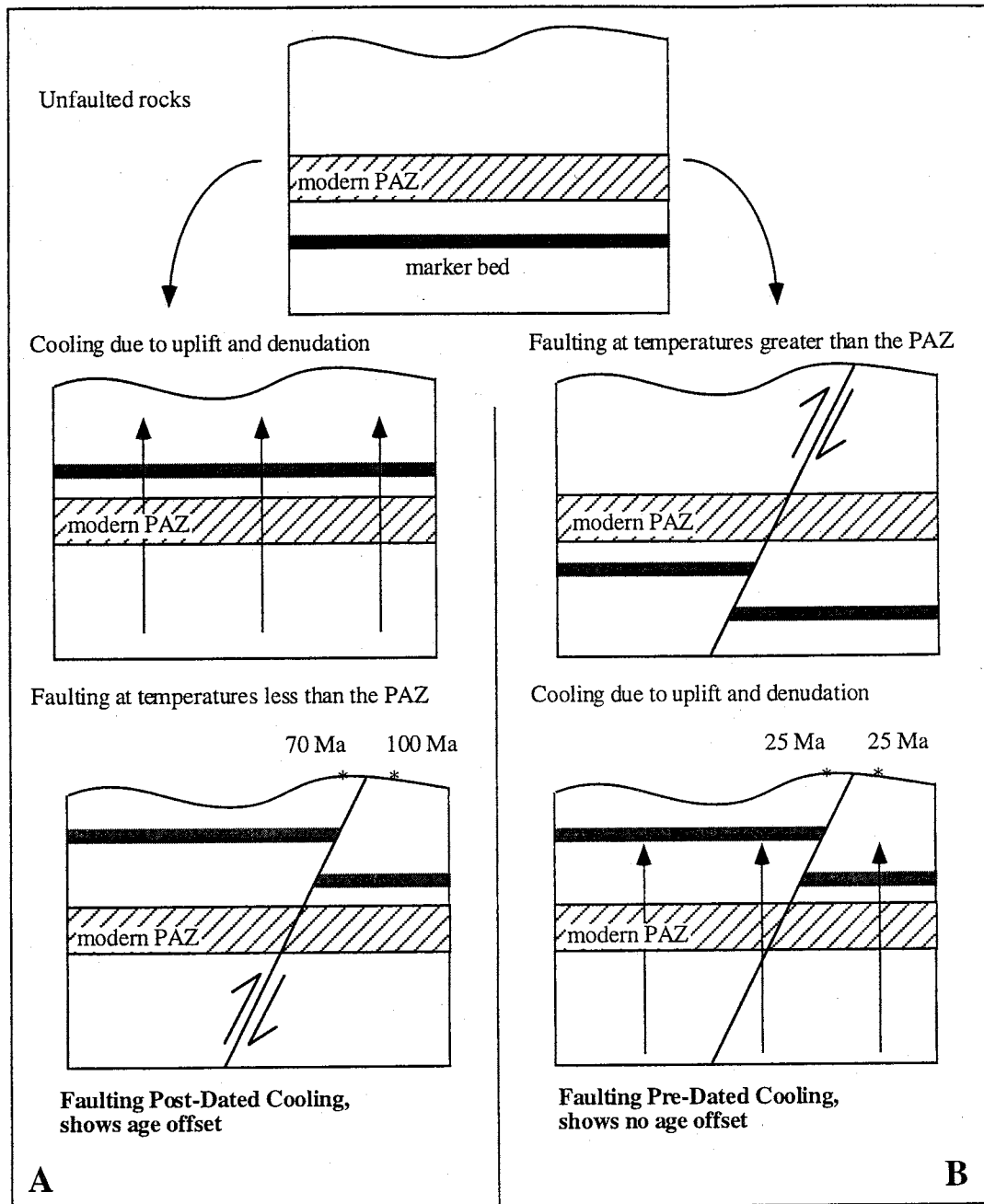
Figure 2-7. A) If faulting post-dated cooling, there will be an AFT age offset in rocks of equal elevation on either side of the fault. B) If faulting pre-dated cooling, rocks of equal elevation came through the PAZ at the same time and therefore show the same age. After Abbott (1995).

difference in ages across the fault, even if faulting postdated cooling. This is not the case during reverse faulting along the Montosa fault, because stratigraphic evidence indicates more than 600 m vertical separation across the fault at Cerro Montoso in the northern Los Piños Mountains (Part I).

Apatite fission-track data across the Montosa fault do not show significant age disparities, which suggests that initial dextral-reverse faulting occurred before cooling. Therefore rocks currently at the surface were at temperatures greater than 120°C during the Laramide orogeny. Normal reactivation would also have occurred before faulting, or normal offset was not significant enough to be recorded by AFT. The Los Piños fault, a normal fault located on the west side of the Los Piños and Manzano Mountains, likely accommodated a large portion of the normal offset resulting from Rio Grande rift formation, and the Montosa fault only accommodated a few hundred meters of normal offset. Track-length distributions and ages were modeled using the computer program AFTSolve© to create best-fit temperature histories (Fig. 2-8; Appendix E). The AFT data primarily record post-Eocene cooling, providing little information about Laramide deformation. Models assuming uplift and erosion during the Laramide orogeny followed by post-Laramide burial or reheating yield similar results to models assuming simple post-Eocene cooling (Fig. 2-8B).

Samples 97PT2, 97BW2, and 97GW2 have broad multimodal track-length distributions, suggesting that they remained in the PAZ for long periods of time (Fig. 2-6). The models of 97GW2 indicate that the sample cooled to temperatures below the PAZ after 20 Ma. The history before 20 Ma is poorly constrained by AFT (Fig. 2-8A). Sample 97PT2 cooled to temperatures within the PAZ at 35 Ma, where it remained until approximately 10 Ma, when it cooled to near-surface temperatures. The thermal history of 97PT2 before 35 Ma is poorly constrained by AFT data, as is indicated by the model's broad range of potential thermal histories prior to 35 Ma (Fig. 2-8B). Track-length distributions are probably skewed towards shorter tracks because the tracks partially

55
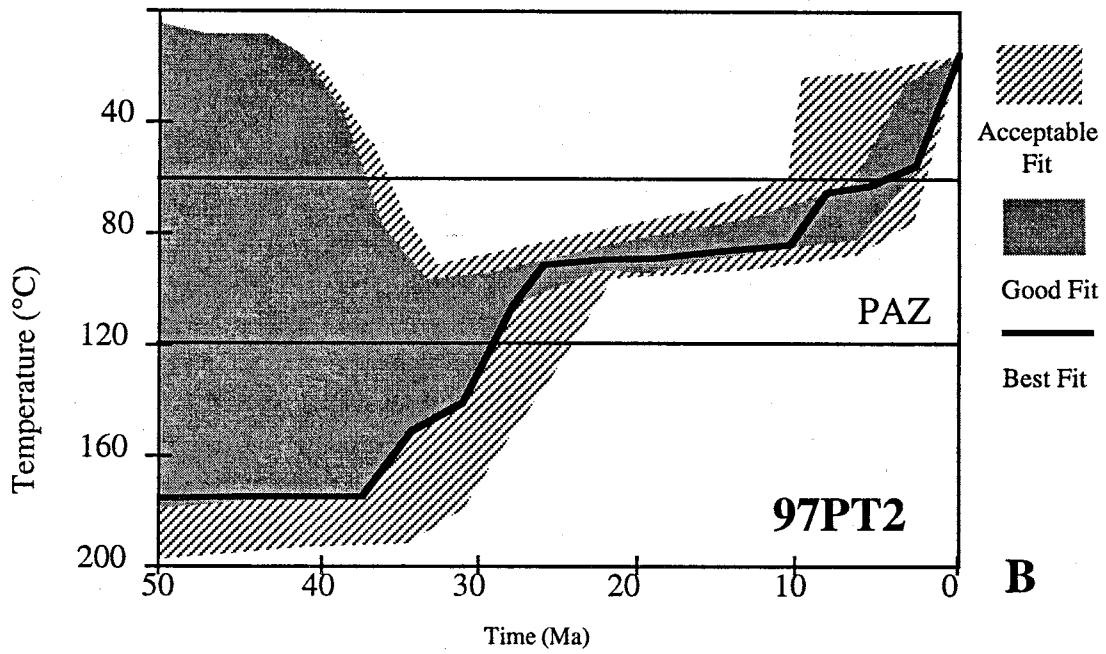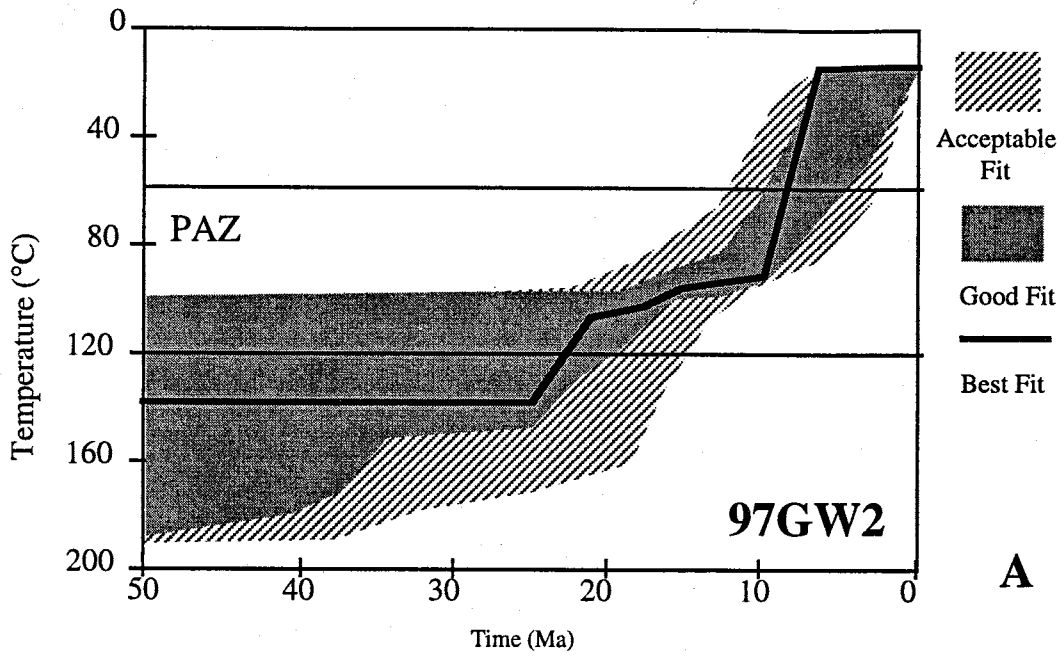
Figure 2-8. Temperature histories of samples 97GW2 (A) and 97PT2 (B) determined from

equations by Donelick et al. (in review) in AFTSolve program. For areas labeled

"acceptable fit", the model and data do not disagree. In a "good fit", the model supports

the data. Where the temperature range is broad, AFT does not closely constrain the thermal

history. Where the temperature range is narrow, AFT data constrains the thermal history

well. A) 97GW2 remained at temperatures greater than or within the PAZ until 20 Ma.

From 10-20 Ma, the sample was at temperatures within the PAZ, then cooled quickly to

near surface temperatures. B) Before 30 Ma, the history of 97PT2 is poorly constrained

by AFT. From 30-10 Ma the sample was within the PAZ, then cooled to near surface

temperatures.

annealed in the elevated temperatures of the PAZ. Sample 97GW1 has a broad unimodal track-length distribution which is skewed towards shorter tracks, indicating that this sample cooled slowly (Compare Figs. 2-5 and 2-6).

The AFT ages for lower elevations within the Manzano Mountains indicate that uplift and denudation occurred in early Oligocene to late Eocene time. Track-length distributions, when modeled with these ages, indicate that the samples remained in the PAZ from at least 25-10 Ma, and then rose quickly to the surface (Fig. 2-8). These data agree with the previous interpretation that lower elevations within the Manzano Mountains cooled early in rift formation (Kelley et al., 1992).

AFT ages from lower elevations within the Los Piños Mountains reflect uplift and denudation during early Eocene to early Oligocene time. Lower elevations within the Los Piños Mountains cooled due to uplift and erosion during the Laramide orogeny and subsequent Rio Grande rift extension. Heat generated by the Pliocene Black Mesa basalt flow near sample 97BW2 (Fig. 2-6) does not seem to have affected the sample age or fission-track lengths.

Samples from the southern tip of the fault reveal younger ages. They reflect cooling in the late Oligocene to mid-Miocene. Farther west a hydrothermal anomaly active from 12-18 Ma reset apatite fission-track ages in the Eocene Baca Formation (Kelley et al., in press). The samples at the south end of the fault probably did not experience the hydrothermal anomaly because, in contrast to the Baca Formation, there is no evidence, such as mineralization or bleaching of the rock, suggesting hydrothermal alteration. Time-temperature models indicate that these samples remained in the PAZ from about 40-10 Ma, when they then cooled quickly to surface temperatures in the late Oligocene and Miocene (Fig. 2-8).

Kelley (1982) thought that most of the uplift of the Los Piños and Manzano Mountains occurred during Neogene Rio Grande rift formation. However, the AFT data in this study suggest a different interpretation. AFT ages of upper elevations within the

Manzano Mountains reflect cooling in the Eocene to Oligocene, whereas rocks of the lower elevations were not cooled until the Oligocene to Miocene (Kelley et al., 1992). Samples from upper elevations within the Los Piños Mountains reveal Laramide ages, indicating they cooled to near-surface conditions during the Laramide orogeny (Kelley et al., 1992). Lower elevation samples have ages which indicate cooling during the early Eocene to late Eocene. The Los Piños Mountains have less relief and gentler slopes than the Manzano Mountains, because they are more mature and have been exposed longer. The young AFT ages of the southern Los Piños Mountains indicate that they remained at higher temperatures longer than the other samples, during which the Laramide thermal history was overprinted. The precise cause of the elevated temperatures in the southern Los Piños Mountains at present is not known, but may be related to the projection of the Socorro Accommodation Zone, which separates west-tilted blocks north of the boundary from east-tilted blocks to the south (Chapin, 1988; Kelley et al., in press).

Overall, the apatite fission-track data reflect denudation and cooling of the Manzano and Los Piños Mountains in the early Eocene to mid-Miocene due to post-Laramide exhumation and Rio Grande rift extension. Fission-track data across the Montosa fault indicate that fault movement predated cooling, and cooling of both the hanging wall and footwall occurred at the same time.

CONCLUSIONS

1. AFT analysis of samples along the Montosa fault in the lower elevations of the Manzano and Los Piños Mountains indicates cooling in the Eocene to mid-Miocene time due to exhumation during the Laramide orogeny and Rio Grande rift extension. This interpretation agrees with previous work. Samples from the southern tip of the fault show a 14-25 Ma age range indicating cooling in the late Oligocene to mid-Miocene. Any possible Laramide history recorded by the apatite fission tracks has been obliterated by the later thermal effects of Rio Grande rift formation.

2. AFT transects do not show significant age variations across the Montosa fault. Reverse faulting during the Laramide orogeny is not recorded in the AFT data because 1) faulting occurred when the rocks were at depths below the base of the PAZ, or 2) the rocks were reheated during post-Laramide reburial. Normal faulting due to Rio Grande rift extension also occurred below or within the PAZ, and is not recorded in the ages across the fault, or displacement was too minimal to see.

REFERENCES

Abbott, J. C. 1995. Constraints on the deformation history of the Tijeras-Cañoncito fault system, north central New Mexico. Unpublished Masters thesis, New Mexico Institute of Mining and Technology.

Allmendinger, R. W. 1995. Stereonet v. 4.9.5a.

Allmendinger, R. W., Marrett, R. A. and Cladouhos, T. 1992. FaultKin v. 3.8.3.

Anderson, E.M., 1951, The dynamics of faulting and dyke formation, with applications to Britain, ed. 2. Oliver and Boyd, Edinburgh. 206 pp.

Armstrong, A.K., 1962. Stratigraphy and paleontology of the Mississippian System in southwestern New Mexico and adjacent southeastern Arizona. *New Mexico Bureau of Mines and Mineral Resources Memoir 8.* 99 pp.

Arne, D. C., Zentilli, M., Grist, A. M. and Collins, M. 1998. Constraints on the timing of thrusting during the Eurekan orogeny, Canadian Arctic Archipeligo: an integrated approach to thermal history analysis. *Canadian Journal of Earth Sciences* v.35, p.30-38.

Baltz, E. H. 1967. Stratigraphic and regional tectonic implications of part of the Upper Cretaceous and Tertiary rocks, east central San Juan Basin, New Mexico. *USGS Professional Paper 552,* p.101.

Bauer, P. and Ralser, S. 1995. The Picuris-Pecos fault repeatedly reactivated, from Proterozoic(?) to Neogene. *New Mexico Geological Society Guidebook, 46th field conference,* p.111-115.

Beck, W.C. and Chapin, C.E., 1994. Structural and tectonic evolution of the Joyita Hills, central New Mexico: Implications of basement control on Rio Grande rift. *Geological Society of America, Special Paper 291.* p.187-205.

Beck, W.C. and Johnson, D.B., 1992. New fusulinid data and multiple episodes of ancestral Rocky Mountain deformation in the Joyita Hills, Socorro County, New Mexico. *New Mexico Geology,* v.14, p.53-59.

Behr, R.-A., Part I. Structural constraints on the Laramide movement history of the Montosa fault, central New Mexico.

Behr, R.-A., Part II. Apatite fission-track thermochronological constraints on the movement history of the Montosa fault, central New Mexico.

Broadhead, R. F., 1997. Subsurface geology and oil and gas potential of Estancia Basin, New Mexico. *New Mexico Bureau of Mines and Mineral Resources Bulletin 157.* 54 pp.

Brown, K. B. 1987. Geology of the southern Cañoncito de la Uva area, Socorro County, New Mexico. Unpublished Masters thesis, New Mexico Institute of Mining and Technology.

Brown, W. G. 1981. Surface and subsurface examples from the Wyoming foreland as evidences of a regional compressional origin for the Laramide orogeny (abst). *Rocky Mountain foreland basement tectonics: Univ. Wyoming Contributions to Geology* v.19, p.175-177.

Cabezas, P. 1987. Stratigraphie et tectonique des deux bordures de rift du Rio Grande dans la region de Socorro. Unpublished Doctorate thesis, L'Universite de Nice.

Cabezas, P. 1991. The southern Rocky Mountains in west-central New Mexico-Laramide structures and their impact on the Rio Grande rift extension. *New Mexico Geology* v.13, p.25-37.

Castillo, D.A., Hickman, S.H., Choi, X., 1997. High shear stress segment along the San Andreas fault: Near-field stress observations in the Carrizo Plain Area. *Eos*, v.78, n.46 Suppl., p.677.

Cather, S. M. 1992. Suggested revisions to the Tertiary tectonic history of north-central New Mexico. In: *New Mexico Geological Society Guidebook San Juan IV, 43rd Field Conference*, p.109-122.

Cather, S. M. 1997. Constraints of Mesozoic piercing lines on magnitude of northward Laramide translation of Colorado Plateau in north-central New Mexico. *New Mexico Geological Society Annual Spring Meeting*, p.15.

Chapin, C. E. 1971. The Rio Grande rift, Part I: Modifications and additions. *New Mexico Geological Society Guidebook: San Luis Basin* v.22, p.191-201.

Chapin, C. E. 1983. An overview of Laramide wrench faulting in the southern Rocky Mountains with emphasis on petroleum exploration. *Rocky Mountain Association of Geologists*, p.169-179.

Chapin, C.E., 1988. Axial basins of the northern and central Rio Grande rift. In: Sloss, L.L., ed.,*Sedimentary cover - North American craton*: U.S. Geological Society of America, the geology of North America, v. D-2., p.165-170.

Chapin, C. E. and Cather, S. M. 1981. Eocene tectonics and sedimentation in the Colorado Plateau-Rocky Mountain area. In: *Relations of tectonics to ore deposits in the southern Cordillera: Arizona Geol. Soc. Digest* (edited by Dickenson, W. R. and Payne, M. D.) v.14, p.173-198.

Cladouhos, T. T. and Allmendinger, W. 1993. Finite strain and rotation from fault-slip data. *Journal of Structural Geology*, v. 15, no. 6, p.771-784.

Colpitts, R. M., Jr. 1986. Geology of the Sierra de la Cruz area, Socorro County, New Mexico. Unpublished Masters thesis, New Mexico Institute of Mining and Technology.

de Voogd, B., Brown, L. D. and Merely, C. 1986. Nature of the eastern boundary of the Rio Grande rift from COCORP surveys in the Albuquerque Basin, New Mexico. *Journal of Geophysical Research* v.91(B6), pp. 6305-6320.

Donelick, R. A., Ketcham, R. A. and Carlson, W. D. in review. Calibration of fission-track annealing in apatite. In: *Fission-Track Thermochronology: Geological Applications* (edited by Naeser, C. W., Dokka, R. K. and Naeser, N. D.).

Duddy, I. R., Green, P. F. and Laslett, G. M. 1988. Thermal annealing of fission tracks in apatite, 3. Variable temperature behavior. *Chemical Geology (Isotope Geoscience Section)* v.73, p.25-38.

Erslev, E. A. 1993. Thrust, back-thrusts, detachment of Rocky Mountain foreland arches. In: *Laramide basement deformation in the Rocky Mountain Foreland of the Western United States* (edited by Schmidt, C. J., Chase, R. B. and Erslev, E. A.) Special Paper 280.

Erslev, E. A. 1997. Multi-directional Laramide compression in the Durango area-why? In: *Natural Fracture Systems*. Four Corners Geological Society, p.1-5.

Erslev, E. A. 1998. Multi-stage, multi-directional Laramide shortening and compression in north-central New Mexico. *New Mexico Geological Society, Annual Spring Meeting*, p.32.

Fleuty, M. J. 1975. Slickensides and slickenlines. *Geology Magazine* v.112(n.3), p.319-322.

Galbraith, R. F. 1981. On statistical models for fission-track counts. *Math. Geol.* v.16, p. 471-438.

Galbraith, R. F. 1984. On statistical estimation of fission-track dating. *Math. Geol.* v.16, p. 653-669.

Galbraith, R. F. and Laslett, G. M. 1985. Some remarks on statistical estimation of fission-track dating. *Nucl. Tracks* v.10, p. 361-363.

Gleadow, A. J. W. and Duddy, I. R. 1981. A natural long-term track annealing experiment for apatite. *Nucl. Tracks* v.5, p. 169-174.

Gleadow, A. J. W., Duddy, I. R., Green, P. F. and Lovering, J. F. 1986. Confined fission-track lengths in apatite: a diagnostic tool for thermal history analysis. *Contrib. Mineral. Petrol.* v.94, p. 405-415.

Green, P. F. 1981. A new look at statistics in the fission-track dating. *Nucl. Tracks* v.5, p. 77-86.

Green, P. F. 1988. The relationship between track shortening and fission track age reduction in apatite: combined influence of inherent instability, annealing anisotropy, length bias, and system calibration. *Earth and Planetary Letters* v.89, p.335-352.

Green, P. F., Duddy, I. R., Gleadow, A. J. W., Tingate, P. R. and Laslett, G. M. 1985. Fission-track annealing in apatite: track length measurements in the form of the Arrhenius plot. *Nucl. Tracks* v.10, p. 323-328.

Green, P. F., Duddy, I. R., Gleadow, A. J. W., Tingate, P. R. and Laslett, G. M. 1986. Thermal annealing of fission tracks in apatite: 1. A qualitative description. *Chem. Geol. (Isot. Geosci. Sect.)* v.59, p. 237-253.

Green, P. F., Duddy, I. R. and Laslett, G. M. 1988. Can fission track annealing in apatite be described by first-order kinetics? *Earth and Planetary Sciences* v.87, p.216-228.

Gregson, J. D. and Erslev, E. A. 1997. Heterogeneous Laramide deformation in the Uinta Mountains, Colorado and Utah. In: *Fractured Reservoirs: Characterization and Modeling Guidebook.* Rocky Mountain Association of Geologists, p.137-154.

Gries, R. 1983. North-South Compression of Rocky Mountain Foreland Structures. *Rocky Mountain Association of Geologists,* p.9-32.

Gries, R. A. 1982. North-south compression of Rocky Mountain foreland structures. *AAPG Bulletin* v.66(n.5), p.574.

Hayden, S. N. 1991. Dextral oblique-slip deformation along the Montosa fault Zone at Abo Pass, Valencia and Socorro Counties, New Mexico. *New Mexico Geology* v.13(n.3), p.64.

Heidrick, T. L. and Titley, S. R. 1982. Fracture and dike pattern in Laramide plutons and their structural and tectonic implications: American southwest. In: *Advances in geology of porphyry copper deposits, southwestern North America* (edited by Titley, S. R.). University of Arizona Press, Tucson, AZ, p.73-91.

Hoisch, T. D., Heizler, M. T. and Zartman, R. E. 1997. Timing of detachment faulting in the Bullfrog Hills and Bare Mountain area, southwest Nevada: Inferences from 40Ar/39Ar, K-Ar, U-Pb, and fission track thermochronology. *Journal of Geophysical Research* v.B2 (n.102), p.2815-2833.

Hurford, A. J. and Green, P. F. 1982. A user's guide to fission-track dating calibration. *Earth Planet. Sci. Lett.* v.59, p. 343-354.

Hurford, A. J. and Green, P. F. 1983. The zeta age calibration of fission-track dating. *Isotope Geosci.* v.1, p. 285-317.

Jurista, B. K., Fryer, S. L. and Erslev, E. A. 1995. Laramide faulting and tectonics of south-central Colorado. *AAPG Bulletin* v. 76(n. 6), p.920.

Karlstrom, K. E. and Daniel, C. G. 1993. Restoration of Laramide right-lateral strike slip in northern New Mexico by using Proterozoic piercing points: Tectonic implications from the Proterozoic to the Cenozoic. *Geology* v.21, p.1139-1142.

Keith, S. B. 1978. Paleosubduction geometries inferred from Cretaceous and Tertiary magmatic patterns in southwestern North America. *Geology* v.6, p.516-521.

Keith, S. B. 1982. Evidence for late Laramide southwest vergent underthrusting in southeast California, southern Arizona, and northeast Sonora. *GSA Abstracts* v.14(n.4), p.177.

Kelley, S. A. 1990. Late Cenozoic cooling history of the Sangre de Cristo Mountains, Colorado and New Mexico. In: *Tectonic Development of the Southern Sangre de Cristo Mountains, New Mexico* (edited by Bauer, P. W., Lucas, S. G., Mawer, C. K. and McIntosh, W. C.) v.41. New Mexico Geological Society, p.123-132.

Kelley, S. A. and Chapin, C. E. 1997. Internal structure of the southern Front Range, Colorado, from an apatite fission-track thermochronology perspective. In: *Colorado Front Range Guidebook*. Rocky Mountain Association of Geologists, p.19-30.

Kelley, S. A., Chapin, C. E., Cather, S. M. and Person, M. in press. Thermal history and paleohydrology of the Eastern Socorro Basin, Socorro County, New Mexico, based on apatite fission-track thermochronology. *New Mexico Geology*.

Kelley, S. A., Chapin, C. E. and Corrigan, J. 1992. Late Mesozoic to Cenozoic cooling histories of the flanks of the northern and central Rio Grande rift, Colorado and New Mexico. *New Mexico Bureau of Mines and Mineral Resources Bulletin 145*, p. 38.

Kelley, V. C. 1977. Geology of the Albuquerque Basin, New Mexico. *New Mexico Bureau of Mines and Mineral Resources* Memoir 33, pp. 60.

Kelley, V. C. 1982. Diverse geology of the Hubbell Bench, Albuquerque Basin, New Mexico. *New Mexico Geological Society Guidebook, 33rd Field Conference, Albuquerque County II*, p.159-160.

Keyes, C. R. 1903. Geological sketch of New Mexico. *Ores and Metals* v.12, p.48.

Knepper, D. H. and Maars, R. W. 1971. Geological development of the Bonanza-San Luis Valley-Sangre de Cristo area, south central Colorado. *New Mexico Geological Society Guidebook, San Luis Basin*, p.249-264.

Laslett, G.M., Kendall, W.S., Gleadow, A.J.W., and Duddy, I.R., 1982. Bias in measurement of fission-track length distributions. *Nucl. Tracks*, v.6, p.79-85.

Laslett, G. M., Green, P. F., Duddy, I. R. and Gleadow, A. J. W. 1987. Thermal annealing of fission tracks in apatite, 2. A quantitative analysis. *Chemical Geology (Isotope Geoscience Section)* v. 65, p.1-13.

Lisenbee, A. L., Woodward, L. A. and Connolly, J. R. 1979. Tijeras-Cañoncito fault system-A major zone of recurrent movement in north-central New Mexico. *New Mexico Geological Society Guidebook, 30th Field Conference, Santa Fe County*, p.89-99.

Livaccari, R. F. 1991. Role of crustal thickening and extensional collapse in the tectonic evolution of the Sevier-Laramide orogeny, western United States. *Geology* v.19, p.1104-1107.

Lowell, J. D. 1974. Plate tectonics and foreland basement deformation. *Geology* v.2, p.275-278.

Lucas, S. G. 1997. Stratigraphically defined piercing lines indicate minimal right slip on eastern margin of Colorado Plateau during Laramide time. *New Mexico Geological Society, Annual Spring Meeting*, p.16.

Marrett, R. and Allmendinger, R. W. 1990. Kinematic analysis of fault slip-data. *Journal of Structural Geology*, v.12, no.8, p.973-986.

Maxson, J. and Tikoff, B. 1996. Hit-and-run collision model for the Laramide orogeny, western United States. *Geology*, v.24, no.11, p.968-972.

McEachran, D. B. 1994. Rosy 2-D orientation analysis for the Macintosh.

Michael, A. J. 1984. Determination of stress from slip data: faults and folds. *Journal of Geophysical Research.*, v. 89, no. B13, p.11,517-11,526.

Miller, J. P., Montgomery, A. and Sutherland, P. K. 1963. Geology of part of the Southern Sangre de Cristo Mountains, New Mexico. *New Mexico Bureau of Mines and Mineral Resources Memoir 11.*

Mount, V.S and Suppe, J., 1992. Present-day stress orientations adjacent to active strike-slip faults: California and Sumatra. *Journal of Geophysical Research*, v.97, pgs. 11,995-12,013.

Myers, D. A. 1973. The late Paleozoic Madera Group in the Manzano Mountains, New Mexico. *U.S. Geological Survey Bulletin* 1372-F, p.F1-F13.

Myers, D. A. 1977. Geologic map of the Scholle Quadrangle, Socorro, Valencia, and Torrance Counties, New Mexico.

Myers, D. A. and McKay, E. J. 1971. Geologic map of the Bosque Peak Quadrangle, Valencia and Bernallio Counties, New Mexico.

Myers, D. A. and McKay, E. J. 1972. Geologic map of the Capilla Peak Quadrangle, Torrance and Valencia Counties, New Mexico.

Myers, D. A. and McKay, E. J. 1974. Geologic map of the southwest quarter of the Torreon 15-minute quadrangle, Torrance and Valencia Counties, New Mexico.

Myers, D. A., McKay, E. J. and Sharps, J. A. 1981. Geologic map of the Becker Quadrangle, Valencia and Socorro Counties, New Mexico.

Myers, D. A., Sharps, J. A. and McKay, E. J. 1986. Geologic map of the Becker SW and Cerro Montoso Quadrangles, Socorro County, New Mexico.

Naeser, C. W. 1979. Fission-track dating and geologic annealing of fission tracks. In: *Lectures in Isotope Geology* (edited by Jager, E. and Hunziker, J. C.). Springer-Verlag, Heidelberg, p. 154-169.

Naeser, C. W. and Faul, H. 1969. Fission-track annealing in apatite and sphene. *J. Geophys. Res.* v.74, p. 705-710.

New Mexico Geological Society 1982. New Mexico Highway Geologic Map.

Osburn, G. R. 1983. Geology of Socorro County. New Mexico Bureau of Mines and Mineral Resources.

Peterson, J.A., 1980. Permian paleogeography and sedimentary provinces, west-central United States. In: Fouch, T.D. and Magathan, E.R., eds., *Paleozoic paleogeography of west-central United States*: Society of Economic Paleontologists and Mineralogists, Rocky Mountain Section, Symposium 1, p.271-292.

Petit, J. P. 1987. Criteria for sense of movement on fault surfaces in brittle rocks. *Journal of Structural Geology* v.9, p.509-608.

Rehrig, W. A. and Heidrick, T. L. 1976. Regional tectonic stress during the Laramide and late Tertiary intrusive periods, Basin and Range province, Arizona. *Arizona Geological Society Digest* v.10(March), p.205-228.

Reiches, P. 1949. Geology of the Manzanita and North Manzano Mountains, New Mexico. *Bulletin of the Geological Society of America* v.60, p.1183-1212.

Rodgers, J. 1987. Chains of basement uplifts within cratons marginal to orogenic belts. *American Journal of Science*, v.287, p.661-692.

Seager, W. R. and Mack, G. H. 1983. Laramide paleotectonics of southern New Mexico. In: *Paleotectonics and sedimentation in the Rocky Mountain region of the United States* (edited by Patterson, J. A.) v.41. AAPG Memoir, p.669-685.

Selvig, B. W. 1994. Kinematics and structural models of faulting adjacent to the Rocky Flats Plant, central Colorado, Colorado State University.

Slack, P. B. and Campbell, J. A. 1976. Structural geology of the Rio Puerco fault zone and its relationship to central New Mexico tectonics. In: *Tectonics and mineral resources of southwestern North America: New Mexico Geological Society Special Publication 6* (edited by Woodward, L. A. and Northrop, S. A.), p.46-52.

Stark, J. T. 1956. Geology of the South Manzano Mountains, New Mexico. *New Mexico State Bureau of Mines and Mineral Resources, Bulletin 34*, 48 pp.

Stark, J. T. and Dapples, E. C. 1946. Geology of the Los Piños Mountains, New Mexico. *Bulletin of the Geological Society of America* v.57, p.1121-1172.

Stearns, C. E. 1953. Tertiary geology of the Galisteo-Tonque area, New Mexico. *Geological Society of America Bulletin* v.64, p.459-506.

Stewart, K. G. and Hibbard, J. P. 1992. Late Cretaceous thrust faulting and the eastern edge of the San Juan, New Mexico. *New Mexico Geological Society Guidebook, San Juan Basin IV* v.43, p.7-9.

Stone, D. S. 1969. Wrench faulting and Rocky Mountain tectonics. *The Mountain Geologist* v.6(n.2), p.67-79.

Stone, D. S. 1975. A dynamic analysis of subsurface structures in northwestern Colorado. In: *Symposium on deep drilling frontiers in the central Rocky Mountains* (edited by Bolyard, D. W.). Rocky Mountain Association of Geologists, p.33-40.

Tavarnelli, E., 1998. Tectonic evolution of the northern Salient Block, California. USA: Paleogene to Recent shortening in a transform fault-bounded continental fragment. *In* Holdsworth, R.E., Strachan, R.A., and Dewey, J.F. (eds) 1998. *Continental Transpressional and Transtensional Tectonics*. Geological Society, London, Special Publications, 135. P. 107-118.

Teyssier, C, Tikoff, B., and Markley, M., 1995. Oblique plate motion and continetal tectonics. *Geology*, v.23, n. 5, p.447-450.

Thompson, A.G., Grambling, J.A., Karlstrom, K.E., Dallmeyer, R.D. 1996. Mesoproterozoic metamorphism and ^{40}Ar/^{39}Ar thermal history of the 1.4Ga Priest pluton, Manzano Mountains, New Mexico. *Journal of Geology.* v.104, no. 5, p.583-598.

Wagner, G. A. 1968. Fission-track dating of apatites. *Earth Planet. Sci. Lett.* v.4, p. 411-415.

Wagner, G. A. 1972. The geological interpretation of fission-track ages. *Trans. Amer. Nucl. Soc.* v.15, p.117.

Wagner, G.A. and Van Den Haute, P. 1992. *Fission-track dating.* Kluwer Academic Publishers, Dordrecht, The Netherlands.

Wilpolt, R. H. and Wanek, A. A. 1951. *Geology of the Region from Socorro and San Antonio east to Chupadera Mesa, Socorro County, New Mexico.* New Mexico Bureau of Mines and Mineral Resources.

Woodward, L. A. 1976. Laramide deformation of Rocky Mountain Foreland: Geometry and mechanics. In: *Tectonics and Mineral Resources of southwestern North America* (edited by Woodward, L. A. and Northrop, S. A.) n.6. New Mexico Geological Society Special Publication, p.11-17.

Woodward, L.A., Anderson, O.J., and Lucas, S.G., 1997. Mesozoic stratigraphic constraints on Laramide right slup on the east side of the Colorado Plateau. *Geology,* v.25, no.9, p.843-846.

Zoback, M.D., Zoback, M.L., Mount, V.S, Suppe, J., Eaton, J.P., Healy, J.H., Oppenheimer, D., Reasenberg, P., Jones, L., Ra;eigh, C.B., Wong, I.G., Scotti, O., and Wentworth, C., 1987. New evidence on the stat of stress of the San Andreas fault system. *Science,* v.238, p.1105-1111.

APPENDIX A

Minor fault, slickenside, and slickenline data collected along the Montosa fault in ten

different areas (Plate 1). Fault plane orientations are recorded with strike, dip, and dip

direction. Rake was measured from the end of strike line recorded in the strike column

(i.e. if strike is 20, then rake is to the north, but if strike is 200, then rake is to the south).

Sense of slip is recorded if known. T=thrust, N=Normal, D=Dextral strike-slip,

S=Sinistral strike-slip. Sense of shear is inferred where fault planes and lineations are

parallel to those with known sense of shear. The sense of shear was determined using

criteria outlined by Petit (1987) or stratigraphic separation. Sense of slip criteria include:

secondary fractures, slickenfibers, and stratigraphic separation.

General Area	Rock Type	Strike	Dip	Rake	Trend	Plunge	Sense of Shear Known	Inferred	Criteria
Cañon Colorado	sandstone	90	32 S	12	100	5		S	
Cañon Colorado	sandstone	90	32 S	10	110	3		S	
Cañon Colorado	sandstone	90	32 S	12	100	9		S	
Cañon Colorado	sandstone	135	57 N	20	123	16		DN	
Cañon Colorado	sandstone	265	60 N	20	275	17			
Cañon Colorado	sandstone	145	69 N	2	144	2		DN	
Cañon Colorado	sandstone	145	69 N	20	138	19		DN	
Cañon Colorado	sandstone	130	78 N	20	126	20		DN	
Cañon Colorado	sandstone	125	76 N	40	114	39			
Cañon Colorado	sandstone	134	43 N	13	124	9		DN	
Cañon Colorado	sandstone	134	43 N	0	134	0		DN	
Cañon Colorado	sandstone	305	58 N	0			D		secondary fractures
Cañon Colorado	sandstone	325	67 N	0				D	
Cañon Colorado	sandstone	145	67 N	20					
Cañon Colorado	sandstone	265	72 N	70			T		secondary fractures
Cañon Colorado	sandstone	94	65 N	5					
Cañon Colorado	sandstone	281	84 N	75			T		secondary fractures
Cañon Colorado	sandstone	105	26 S	0-5			S		secondary fractures
Cañon Nuevo	limestone	340	15 N		355	7			
Cañon Nuevo	schist	210	72 E	85	135	71			
Cañon Nuevo	schist	30	72 E	85	104	71			
Cañon Nuevo	schist	225	5 N	40	264	3			
Gallina Well	conglomerate	195	68E	80			N		slickenfibers
Gallina Well	conglomerate				285	26			
Gallina Well	conglomerate	190	44 W	85	273	43		T	
Gallina Well	conglomerate	355	38 W	60 N	301	32	ST		secondary fractures
Gallina Well	limestone	190	46 N	70			T		slickenfibers
Gallina Well	limestone	170	26 W	60				T	
Gallina Well	limestone	15	46 W	90				T	
Gallina Well	limestone	315	13 S	40	290	8		ST	slickenfibers
Gallina Well	limestone	10	35 W	90				T	
Gallina Well	limestone	205	19 W	80			N		slickenfibers
Gallina Well	limestone	220	20 W	60			N		slickenfibers
Gallina Well	limestone	194	15 W	60			N		slickenfibers
Gallina Well	limestone	225	25 W	60			N		slickenfibers
Gallina Well	limestone	225	20 W	55			N		slickenfibers
Gallina Well	limestone	45	70 E	80					
Gallina Well	limestone	205	7 N	60			N		slickenfibers
Gallina Well	limestone	3	44 N	85			T		slickenfibers
Gallina Well	limestone	190	56 W	85			T		slickenfibers
Gallina Well	limestone	8	35 E	90					
Gallina Well	limestone	170	28 E	75					
Gallina Well	limestone	173	31 E	70					
Gallina Well	limestone	208	17 N	60			T		secondary fractures
Gallina Well	limestone	193	35 E	55	143	28		N	
Gallina Well	limestone				100	60			
Gallina Well	limestone	235	40 S	60	182	34			
Gallina Well	limestone	42	46 S	60	92	29		N	
Gallina Well	limestone	80	23 S	65	143	20			
Gallina Well	limestone	301	25 S	30	273	12	ST		slickenfibers
Gallina Well	limestone	280	24 N	0	280	0			slickenfibers
Gallina Well	limestone	222	20 E	78	144	20	ST		slickenfibers
Gallina Well	limestone	345	85 N	20					
Gallina Well	limestone	165	56 NE	60					
Gallina Well	limestone	335	61 NE	0			S		slickenfibers
Gallina Well	limestone	170	30 E	40			DN		slickenfibers
Gallina Well	limy mudstone	38	66 S	90			N		slickenfibers
Gallina Well	limy mudstone	10	38 S	65			N		slickenfibers
Gallina Well	limy mudstone	37	45 E	75			N		slickenfibers
Gallina Well	limy mudstone	220	30 W	50	266	22			
Gallina Well	limy mudstone	210	70 W	85	285	70		N	
Gallina Well	limy mudstone	355	30 W	90	265	30		T	
Gallina Well	limy mudstone	210	71 W	70	251	63		N	

Gallina Well	limy mudstone	243	87 S	37	240	37		DN	
Gallina Well	limy mudstone	224	76 W	65	251	62		N	
Gallina Well	limy mudstone	61	75 W	90	331	75			
Gallina Well	limy mudstone	225	56 E	65	174	48		N	
Gallina Well	limy mudstone	45	42 E	90	135	42		N	
Gallina Well	limy mudstone	245	70 W	60	276	54			
Gallina Well	limy mudstone	65	70 W	70	21	62			
Gallina Well	limy mudstone	220	30 W	50	266	22			
Gallina Well	limy mudstone	355	35 W	90	266	35		T	
Gallina Well	limy mudstone	210	71 W	70	251	62		N	
Gallina Well	limy mudstone	6	32 W	60	310	27		T	
Gallina Well	limy mudstone	18	37 N	80	300	36		T	
Gallina Well	limy mudstone	22	20 N	80	302	20		T	
Gallina Well	limy mudstone	26	22 W	84	302	22		T	
Gallina Well	limy mudstone	45	27 E	80	124	27		T	
Gallina Well	limy mudstone	5	26 W	80	286	26		T	
Gallina Well	limy mudstone	185	26 W	70	253	24		T	
Gallina Well	limy sandstone	275	60 S	60					
Gallina Well	limy sandstone	210	85 E	35					
Gallina Well	limy sandstone	35	85 E	90				LT	
Gallina Well	limy sandstone	200	87 W	60					
Gallina Well	mudstone	152	25 N	55	116			N	
Gallina Well	mudstone	204	24 W	75				T	
Gallina Well	mudstone	168	28 N	55				N	
Gallina Well	mudstone	339	29 N	90					
Gallina Well	mudstone	158	15 N	70					
Gallina Well	mudstone	140	60 N	55					
Gallina Well	mudstone	142	38 N	45					
Gallina Well	mudstone	38	34 SE	65	85	27	T		secondary fractures
Gallina Well	mudstone	290	9 S	30					
Gallina Well	mudstone	170	26 N	80					
Gallina Well	mudstone	80	34 N	15					
Gallina Well	mudstone	95	11 N	25					
Gallina Well	mudstone	190	25 W	60			T		secondary fractures
Gallina Well	mudstone	209	11 W	50					
Gallina Well	mudstone	225	11 N	10					
Gallina Well	mudstone	200	6 N	45					
Gallina Well	mudstone	300	75 S	90					
Gallina Well	mudstone	65	40 S	70			N		secondary fractures
Gallina Well	mudstone	218	15 E	85					
Gallina Well	mudstone	190	20 E	70					
Gallina Well	mudstone	31	32 E	75					
Gallina Well	mudstone	104	64 N	40					
Gallina Well	mudstone	245	18 N	60				N	
Gallina Well	mudstone	229	11 N	60				N	
Gallina Well	mudstone	170	22 E	60					
Gallina Well	mudstone	151	34 E	70					
Gallina Well	mudstone	180	35 E	80			N		secondary fractures
Gallina Well	mudstone	135	61 W	50					
Gallina Well	mudstone	55	25 S	70					
Gallina Well	mudstone	163	75 S	50					
Gallina Well	mudstone	160	71 S	55					
Gallina Well	mudstone	185	77 W	35					
Gallina Well	mudstone	185	23 W	60				N	
Gallina Well	mudstone	170	58 E	80					
Gallina Well	mudstone	7	85 E	88					
Gallina Well	mudstone	20	26 W	35					
Gallina Well	mudstone	14	68 E	75					
Gallina Well	mudstone	0	45 E	75					
Gallina Well	mudstone	163	35 E	75					
Gallina Well	mudstone	150	30 E	60					
Gallina Well	mudstone	175	34 E	80					
Gallina Well	mudstone	2	30 E	80			T		secondary fractures
Gallina Well	mudstone	10	60 E	60			T		secondary fractures
Gallina Well	mudstone	36	75 E	90	126	75			

Gallina Well	mudstone				105	19			
Gallina Well	mudstone	225	32 S	60	169	27			
Gallina Well	mudstone	20	25 S	80	99	24	N		secondary fractures
Gallina Well	mudstone	306	14 N	0	306	14	S		secondary fractures
Gallina Well	mudstone				130	39			
Gallina Well	mudstone	232	78 N	85	299	77		N	
Gallina Well	mudstone	147	42 N	25	127	16	DN		secondary fractures
Gallina Well	mudstone	205	10 S	80	229	4	N		secondary fractures
Gallina Well	mudstone	313	35 N	NEAR 0	313	0			
Gallina Well	mudstone				110	0			
Gallina Well	mudstone				140	55			
Gallina Well	mudstone	168	45 E	60	117	38			
Gallina Well	mudstone				108	45	T		secondary fractures
Gallina Well	mudstone				116	48	T		secondary fractures
Gallina Well	mudstone				120	21	T		secondary fractures
Gallina Well	mudstone				148	40	N		secondary fractures
Gallina Well	mudstone				145	50			
Gallina Well	mudstone	165	76 N	60	142	57			
Gallina Well	mudstone	200	64 S	50	172	43			
Gallina Well	mudstone	200	64 S	90	110	64			
Gallina Well	mudstone	175	64 S	70	225	57			
Gallina Well	mudstone	355	71 W	70	313	63			
Gallina Well	mudstone	6	82 W	75	338	73			
Gallina Well	mudstone	35	75 W	70	359	65			
Gallina Well	mudstone	200	14 S	85	115	14			
Gallina Well	mudstone	249	88 S	38			DN		slickenfibers
Gallina Well	mudstone	245	75 NE	40			DT		slickenfibers
Gallina Well	mudstone	230	65 N	45			DT		slickenfibers
Gallina Well	mudstone	245	71 N	35			DT		slickenfibers
Gallina Well	mudstone	220	55 SE	90			N		slickenfibers
Gallina Well	mudstone	200	70 N	85			SN		slickenfibers
Gallina Well	sandstone	241	78 N	60				T	
Gallina Well	sandstone	51	80 N	70			N		secondary fractures
Gallina Well	sandstone	52	76 N	85			N		secondary fractures
Gallina Well	sandstone	58	55 S	90					
Gallina Well	sandstone	46	66 N	70					
Gallina Well	sandstone	86	56 S	55					
Gallina Well	sandstone	78	38 S	90					
Gallina Well	sandstone	271	70 S	85					
Gallina Well	sandstone	75	72 N	80					
Gallina Well	sandstone	285	74 N	70					
Gallina Well	sandstone	186	26 W	65	248	23		T	
Gallina Well	sandstone	178	20 W	70	246	18		T	
Gallina Well	sandstone	358	20 W	80	279	20		T	
Gallina Well	sandstone	55	64 S	80	123	62			
Gallina Well	sandstone	230	21 N	60	288	18			
Gallina Well	sandstone				132	0			
Gallina Well	sandstone	330	23 E	90	60	23			
Gallina Well	sandstone	18	18 N	40	340	12			
Gallina Well	sandstone	18	18E	75	92	17			
Gallina Well	sandstone				145	30			
Gallina Well	sandstone				120	25			
Gallina Well	sandstone				305	16	N		secondary fractures
Gallina Well	sandstone	311	45 N	20	325	14			
Gallina Well	sandstone	289	64 N	20				DT	
Gallina Well	sandstone	248	82 N	40			DT		slickenfibers
Gallina Well	sandstone	345	22 SW	60				T	
Gallina Well	sandstone	290	65 N	30			DT		slickenfibers
Gallina Well	sandstone	235	72 S	0					
Gallina Well	sandstone	235	72 S	90					
Gallina Well	sandstone	246	89 S	0					
Gallina Well	sandstone	254	84 S	0					
Gallina Well	sandstone	265	90	0					
Gallina Well	sandstone	245	67 N	25			D		secondary fractures
Gallina Well	sandstone	242	67 N	23			DT		secondary fractures

Location	Rock								Notes
Gallina Well	sandstone	230	34 N	40					
Gallina Well	sandstone	242	77 N	75 W			N		slickenfibers
Gallina Well	sandstone	238	74 N	85				N	
Gallina Well	sandstone	186	25 W	70					
Gallina Well	sandstone	6	25 W	80					
Gallina Well	sandstone	230	71N	80				N	
Gallina Well	siltstone	201	44 W	60				T	
Gallina Well	siltstone	238	30 N	40				SN	
Gallina Well	siltstone	246	40 N	35				SN	
Gallina Well	siltstone	195	53 W	50			T		slickenfibers
Gallina Well	siltstone	185	56 W	55				T	
Isletta Reservation	sandstone				25	13			
Isletta Reservation	sandstone				30	4			
Isletta Reservation	sandstone	55	90	65	55	65			
Isletta Reservation	sandstone	160	63 S	70	211	57			
Parker Ranch	pegmatite	80	19 S	10					
Parker Ranch	quartzite	182	44 W	75				T	
Parker Ranch	quartzite	2	38 W	80				T	
Parker Ranch	quartzite	6	46 W	75				T	
Parker Ranch	quartzite	190	47 W	80				T	
Parker Ranch	quartzite	5	35 W	75				T	
Parker Ranch	quartzite	50	28 E	55				T	
Parker Ranch	quartzite	60	18 E	70				T	
Parker Ranch	quartzite	30	43 E	25					
Parker Ranch	quartzite	4	24 E	40					
Parker Ranch	quartzite	186	70 W	75					
Parker Ranch	quartzite	210	86 W	75					
Parker Ranch	quartzite	330	13 S	30				ST	
Parker Ranch	quartzite	185	60 E	80					
Parker Ranch	quartzite	245	45 N	40			DT		secondary fractures
Parker Ranch	quartzite	76	12 S	10					
Parker Ranch	sandstone	160	88 N	20					
Parker Ranch	sandstone	112	48 s	60			T		secondary fractures
Parker Ranch	sandstone	120	44 S	50				T	
Parker Ranch	sandstone	160	85 N	< 10					
Parker Ranch	sandstone	150	30 W	65					
Parker Ranch	sandstone	170	18 N	30					
Parker Ranch	sandstone	180	34 E	70				T	
Parker Ranch	sandstone	125	48 S	45					
Parker Ranch	sandstone	5	47 E	90				T	
Parker Ranch	sandstone	158	35 E	65				N	
Parker Ranch	sandstone	150	36 N	50				N	
Parker Ranch	sandstone	125	54 N	30				DN	
Parker Ranch	sandstone	160	45 E	65				N	
Parker Ranch	sandstone	155	60 N	45				N	
Parker Ranch	sandstone	126	30 N	15				DN	
Parker Ranch	sandstone	214	67 S	70				T	
Parker Ranch	sandstone	215	28 S	50			N		secondary fractures
Parker Ranch	sandstone	210	67 S	65				T	
Parker Ranch	sandstone	210	54 E	85				T	
Parker Ranch	sandstone	24	75 E	90				T	
Parker Ranch	sandstone	9	82 E	85				T	
Parker Ranch	sandstone	5	46 E	90				T	
Parker Ranch	sandstone	260	14 N	45					
Parker Ranch	sandstone	203	44 E	65				T	
Parker Ranch	sandstone	203	58 E	65				T	
Parker Ranch	sandstone	175	50 E	55			T	T	secondary fractures
Parker Ranch	sandstone	310	4 S	20	286	1			
Parker Ranch	sandstone	204	80 E	80				T	
Parker Ranch	sandstone	200	64 E	85				T	
Parker Ranch	sandstone	160	29 N	70					
Parker Ranch	sandstone	197	58 E	80				T	
Parker Ranch	sandstone	195	12 E	90	105	13		N	
Parker Ranch	sandstone	208	26 E	80	110	27		N	
Parker Ranch	sandy limestone	24	55 E	50					

Location	Rock type								
Quarry	quartzite	35	44 E	15			S		secondary fractures
Quarry	quartzite	215	44 E	10			S		secondary fractures
Quarry	quartzite	228	51 S	5	224	4	S		secondary fractures
Quarry	quartzite	75	47 S	40					
Quarry	quartzite	250	19 S	30					
Quarry	quartzite	50	50 E	80			TD		secondary fractures
Quarry	quartzite	70	52 E	60			TD		secondary fractures
Quarry	quartzite	55	50 E	34			DT		secondary fractures
Quarry	quartzite	68	61 E	20			DT		secondary fractures
Quarry	quartzite	58	55 E	20			DT		secondary fractures
Quarry	quartzite	45	66 E	30			DT		secondary fractures
Quarry	quartzite	40	50 E	40			DT		secondary fractures
Quarry	quartzite	60	79 E	30-50					
Quarry	quartzite	60	75 E	50					
Quarry	quartzite	50	78 E	40					
Quarry	quartzite	50	78 E	70					
Quarry	quartzite	60	90	55			TD		secondary fractures
Quarry	quartzite	35	55 S	45			TD		secondary fractures
Quarry	quartzite	45	46 S	40			TD		secondary fractures
Quarry	quartzite	20	65 S	70			TD		secondary fractures
Quarry	quartzite	50	73 S	50			TD		secondary fractures
Quarry	quartzite	45	50 S	45					
Quarry	quartzite	74	86 S	40					
Quarry	quartzite	75	88 N	40					
Quarry	quartzite	40	70 W	85-90			N		secondary fractures
Quarry	quartzite	30	68 W	80					
Quarry	quartzite	65	50 N	55			ND		secondary fractures
Quarry	quartzite	335	90	45					
Quarry	quartzite	342	72 S	45			ND		secondary fractures
Quarry	quartzite	345	85 N	30					
Quarry	quartzite	325	80 S	30					
Quarry	quartzite	160	75 S	90					
Quarry	quartzite	345	75 S	80					
Quarry	quartzite	350	61 S	90			N		secondary fractures
Quarry	quartzite	145	50 N	30					
Quarry	quartzite	200	74 S	70			ND		stratigraphic separatio
Quarry	quartzite	63	79 E	75			NS		stratigraphic separatio
Quarry	quartzite	20	86 W	75			ND		stratigraphic separatio
Railway cut	limestone	280	88 S	40	278	40		SN	
Railway cut	limestone	110	38 N	50	67	28		N	
Railway cut	limestone	290	88 N	40	292	40		DN	
Railway cut	limestone	350	54 W	25	335	20			
Railway cut	limestone	120	41 N	85	37	41		N	
Railway cut	limestone	180	70 E	70	137	62			
Railway cut	limestone	170	68 W	65	209	57	T		secondary fractures
Railway cut	limestone	127	86 N	50	122	50	N		slickenfibers
Railway cut	limestone	150	85 N	50	144	50	N		slickenfibers
Railway cut	limestone	102	37 S	50	145	27	N		secondary fractures
Railway cut	limestone	130	58 S	30	147	25	N		secondary fractures
Railway cut	limestone	188	74 W	60	213	56	T		secondary fractures
Railway cut	limestone	120	50 S	60	168	41	N		slickenfibers
Railway cut	limestone	200	20 W	70	268	18	N		secondary fractures
Railway cut	limestone	200	85 W	60	208	60	N		secondary fractures
Railway cut	limestone	190	87 W	60	195	60	N		secondary fractures
Railway cut	limestone	0	90	55	180	55	N		secondary fractures
Railway cut	limestone	285	65 S	50	258	44			
Railway cut	limestone	280	70 S	20	272	18			
Railway cut	limestone	220	16 E	85	135	16	N		secondary fractures
Railway cut	limestone	15	65 E	40	34	36	DT		secondary fractures
Railway cut	limestone	0	54 W	60	314	45	TD		secondary fractures
Railway cut	limestone	30	42 W	55	343	33	SN		secondary fractures
Railway cut	limestone	35	75 W	25	28	24	DT		secondary fractures
Railway cut	limestone	178	83 S	60	190	60			
Railway cut	limestone	178	83 S	90	268	83			
Railway cut	limestone	170	86 S	60	177	60			

Railway cut	limestone	170	86 S	90	260	86		
Railway cut	limestone	350	86 S	70	340	70		
Railway cut	quartzite	248	38 W	85	331	38		T	
Railway cut	quartzite	45	68 W	60	12	53		
Railway cut	quartzite	78	75 S	70			TD	stratigraphic separatio
Railway cut	quartzite	62	75 N	45				
Sand Canyon	granite	282	54 N	60	327	45	NS	secondary fractures
Sand Canyon	granite	290	50 N	80	5	49	NS	secondary fractures
Sand Canyon	granite	280	85 N	45	285	45	NS	secondary fractures
Sand Canyon	granite	280	72 N	45	297	42		NS	
Sand Canyon	granite	268	56 N	40	293	32		
Sand Canyon	granite	76	44 W	30	53	20		
Sand Canyon	granite	140	34 N	40	105	21		DN	
Sand Canyon	granite	99	41 N	50	57	30		
Sand Canyon	granite	104	46 N	35	114	24		
Sand Canyon	granite	134	88 S	60	137	60		
Sand Canyon	granite	314	88 S	90	224	88		
Sand Canyon	granite	298	42 N	50	339	31	TD	stratigraphic separatio
Sand Canyon	granite	114	22 N	30	86	11		
Sand Canyon	granite	224	25 E	@45	90	23		
Sand Canyon	limestone	220	76 S	40	208	39	ST	slickenfibers
Sand Canyon	limestone	215	88 E	35	213	35	ST	slickenfibers
Sand Canyon	limestone	210	80 E	10	208	10	ST	slickenfibers
Sand Canyon	limestone	210	70 E	10	207	10	ST	slickenfibers
Sand Canyon	limestone	211	66 E	85	133	65	T	slickenfibers
Sand Canyon	limestone	215	90	35	215	35	ST	slickenfibers
Sand Canyon	limestone	215	72 E	15	210	14	ST	slickenfibers
Sand Canyon	limestone	208	72 E	40	194	38	ST	slickenfibers
Sand Canyon	limestone	212	68 E	30	200	28	ST	slickenfibers
Sand Canyon	limestone	215	79 E	25	210	25	ST	slickenfibers
Sand Canyon	limestone	215	78 E	85	150	77	T	slickenfibers
Sand Canyon	limestone	215	70 E	25	206	23	ST	slickenfibers
Sand Canyon	limestone	215	70 E	30	203	28	ST	slickenfibers
Sand Canyon	limestone	215	78 E	40	205	39	ST	slickenfibers
Sand Canyon	limestone	219	72 E	20	212	19	ST	slickenfibers
Sand Canyon	limestone	205	61 E	75	143	58	T	slickenfibers
Sand Canyon	limestone	180	48 E	10	173	7	S	slickenfibers
Sand Canyon	limestone	205	65 E	80	138	63		T	
Sand Canyon	limestone	285	90	45	285	45		
Sand Canyon	limestone	35	17 E	65	99	15	N	secondary fractures
Sand Canyon	limestone	95	50 N	45	62	32		
Sand Canyon	limestone	220	70 E	80	157	68	T	secondary fractures
Sand Canyon	limestone	215	70 E	80	152	68		T	
Sand Canyon	limestone	226	88 E	85	204	85		
Sand Canyon	limestone	51	19 S	85	135	19		T	
Sand Canyon	limestone	90	85 N	85	45	89		
Sand Canyon	limestone	110	76 N	85	40	75		
Sand Canyon	limestone				310	38		
Sand Canyon	limestone	205	64 W	90	245	64		T	
Sand Canyon	limestone	210	58 W	80	282	57	T	secondary fractures
Sand Canyon	limestone	227	79 W	60	245	58	T	secondary fractures
Sand Canyon	limy sandstone	198	75 W	65	227	61		
Sand Canyon	phyllite	140	74 S	40	153	38		
Sand Canyon	phyllite	310	65 S	50	283	44		
Sand Canyon	phyllite	320	73 S	60	293	56		
Sand Canyon	phyllite	319	80 S	40	310	39		
Sand Canyon	phyllite	104	40 N	45	66	27		
Sand Canyon	phyllite	310	75 N	80	6	72		
Sand Canyon	phyllite	310	75 N	40 W	322	38		
Sand Canyon	phyllite	154	67 S	60	188	52		
Sand Canyon	phyllite	119	66 S	40	137	36		
Sand Canyon	quartzite	210	52 E	80	136	51		
Sand Canyon	quartzite	245	57 S	88	159	57		
Sand Canyon	quartzite	139	76 W	60	116	57		
Sand Canyon	quartzite	240	46 W	35	266	24		DT	

Sand Canyon	quartzite	115	50 N	70	55	46	ND		secondary fractures
Sand Canyon	quartzite	145	90	75	145	75			
Sand Canyon	quartzite	42	62 E	@58	98	52			
Sand Canyon	quartzite	246	80 W	30	252	30	DT		secondary fractures
Sand Canyon	quartzite	358	82 W	50	349	49			
Sand Canyon	quartzite	20	68 E	42	39	38			
Sand Canyon	quartzite	258	86 S	10	257	1	DN		secondary fractures
Sand Canyon	quartzite	24	82 W	5	23	5			
Sand Canyon	quartzite	218	78 E	70	188	67			
Sand Canyon	quartzite	40	74 E	90	130	74			
Sand Canyon	quartzite	40	75 E	90	130	75			
Sand Canyon	quartzite	35	88 E	80	46	80			
Sand Canyon	quartzite	318	74 S	80	260	71			
Sand Canyon	quartzite	240	32 N	50	285	24			
Sand Canyon	quartzite	135	17 N	15	121	4			
Sand Canyon	quartzite	197	8 W	85	282	8			
Sand Canyon	sandstone	72	67 W	30	53	27	ST		slickenfibers
Sand Canyon	sandstone	42	42 E	85	125	41	TD		slickenfibers
Sand Canyon	sandstone	222	32 E	50	176	24			
Sand Canyon	sandstone	5	26 E	90	95	26			
Sand Canyon	sandstone	219	54 E	40	193	31			
Sand Canyon	sandstone	342	9 E		350	0			
Sand Canyon	sandstone	215	37 E	50	171	28			
Sand Canyon	sandstone	331	55-62 E	0	331	0			
Sand Canyon	sandstone	226	30 S	70	160	28			
Sand Canyon	sandstone	172	45 E	20	157	14		DN	
Sand Canyon	sandstone	135	49 E	40	106	29	DN		secondary fractures
Sand Canyon	sandstone	255	25 N	85	339	25		T	
Sand Canyon	sandstone	325-335	35-50 E	0	325	0	S		secondary fractures
Sand Canyon	sandstone	70	25 W	0	70	0		DN	
Sand Canyon	sandstone	240	33 W	40	275	21	DT		secondary fractures
Sand Canyon	sandstone	178	52 E	80	104	51			
Sand Canyon	sandstone	236	33 W	30	262	16	DT		secondary fractures
Sand Canyon	sandstone	232	21 N	30	260	10		DT	
Sand Canyon	sandstone	274	52 N	40	301	30			
Sand Canyon	sandstone	16	38 W	90	286	38			
Sand Canyon	sandstone	145	20 N	@30	120	22			
Sand Canyon	sandstone	52	19 W		65	2			
Sand Canyon	sandstone	154	38 N	30	130	18	DN		secondary fractures
Sand Canyon	sandstone	155	10 E	50	105	8			
Sand Canyon	sandstone	132	44 N	65	75	39	N		secondary fractures
Sand Canyon	sandstone	230	45 E	85	147	45		T	
Sand Canyon	sandstone	130	15 N	20	105	1			
Sand Canyon	sandstone	164	34 N	50	119	25			
Sand Canyon	sandstone	140	24 S	45	206	17			
Sand Canyon	sandstone	61	46 N	60	10	39	T		secondary fractures
Sand Canyon	sandstone	81	35 N	83	359	35	T		secondary fractures
Sand Canyon	sandstone	175	31 E	35	144	17		DN	
Sand Canyon	sandstone	258	36 W	60	312	30			
Sand Canyon	sandstone	153	52 N	10	146	8	DN		secondary fractures
Sand Canyon	sandstone	292	52 N	40	320	30			
Sand Canyon	sandstone	175	51 N	35	151	27		DN	
Sand Canyon	sandstone	44	44 W	90	314	44			
Sand Canyon	sandstone	255	47 W	65	311	41			
Sand Canyon	sandstone	31	19 W	60	332	16			
Sand Canyon	sandstone	215	46 W	50	254	33			
Sand Canyon	sandstone	218	39 W	70	295	38			
Sand Canyon	sandstone	6	11 W	45	321	9			
Sand Canyon	sandstone	264	35 N	63	322	31			
Sand Canyon	sandstone	46	75 E	50	63	47		T	
Sand Canyon	sandstone	184	35 E	50	139	26			
Sand Canyon	sandstone	125	60 N	55	89	45		N	
Sand Canyon	sandstone	122	45 N	30	100	20	DN		secondary fractures
Sand Canyon	sandstone	148	19 N	50	100	14	T		secondary fractures
Sand Canyon	sandstone	33	25 S	55	85	20	N		secondary fractures

Sand Canyon	sandstone	20	42 E	90	110	42		T	
Sand Canyon	sandstone	185	58 E	80	113	57		T	
Sand Canyon	sandstone	180	10 E	80	100	10			
Sand Canyon	schist	322	54 W	60-70	316	8			
Sand Canyon	schist	322	54 W	10	176	24			
Sand Canyon	schist	140	45 N	20	125	14			
Sand Canyon	schist	318	74 S	40	305	38			
Sand Canyon	schist	145	70 S	80	207	68			
Sand Canyon	schist	325	70 S	45	306	42			
Sand Canyon	schist	88	44 S	@70	155	36			
Sand Canyon	schist	335	70 S	80	272	68			
Sand Canyon	schist	285	76 S	83	222	75			
Sand Canyon	schist	283	77 S	85	214	76			
Sand Canyon	schist	269	74 S	78	217	70			
Sand Canyon	schist	173	45 W	80	250	44			
Sand Canyon	schist	198	34 W	70	264	32			
Sand Canyon	schist	85	8 N	24	108	4	DN		secondary fractures
Sand Canyon	schist	178	15 E	35	143	9			
Sand Canyon	schist	145	19 E	35	112	11	DN		secondary fractures
Sand Canyon	schist	311	53 N	0	311	0			
Sand Canyon	schist	140	35 N	82	60	35			
Sand Canyon	schist	170	35 E	80	92	34		N	
Sand Canyon	schist	166	38 N	60	112	32		N	
Sand Canyon	schist	150	44 N	65	93	39		N	
Sand Canyon	schist	140	35 N	38	107	21		DN	
Sand Canyon	schist	125	26 N	20	107	9		DN	
Sand Canyon	schist	38	16 S	65	102	15			
Sand Canyon	schist	60	80 N	80	15	76			
Sand Canyon	schist				165	47			
Sand Canyon	schist	151	26 S	60	208	22			
Sand Canyon	schist	331	26 S	90	241	26			
Sand Canyon	schist	295	58 S	25	281	21			
Sand Canyon	schist	340	19 N	90	70	16			
Sand Canyon	schist	230	13 W	15	245	3			
Sand Canyon	schist	116	28 N	45	74	19			
Sand Canyon	schist	10	9 S	30	43	3			
Sand Canyon	schist	310	46 S	35	284	24			
Sevilleta	dolomite	285	60 N	30					
South Spring	mudstone	92	63N-29N	10					
South Spring	mudstone	95	84 N	5					
South Spring	mudstone	286	55 N	25			D		secondary fractures
South Spring	mudstone	235	80 N	20					
South Spring	mudstone	280	85 N	22			S		secondary fractures
South Spring	mudstone	280	85 S	20			S		secondary fractures
South Spring	mudstone	270	85 S	20			S		secondary fractures
South Spring	sandstone	80	68 S	20			D		secondary fractures
South Spring	sandstone	88	90	22			D		secondary fractures
South Spring	sandstone	100	88 S	10			D		secondary fractures
South Spring	sandstone	85	78 S	40			D		secondary fractures

APPENDIX B

Hand sample and thin section descriptions for samples with enigmatic sense of slip collected along the Montosa fault. In addition to the sample number, the formation and general area that sample was collected are listed (refer to Plate 1).

Sample number: 7-10-3A

Location: Sand Canyon

Formation: Pennsylvanian Wild Cow

Orientation of slickenside and slickenlines: 72, 67 W rake 30 N

Hand Sample:

Slickenlines are thin and delicate, buff to green color on fine green micaceous sandstone. There are slickenlines on both the top and the bottom of the sample on parallel surfaces.

Thin Section:

In thin section, the sample is noted to be very fine-grained arkose. Quartz, microcline, mica, oxides, sericite, green biotite/stained mica, hornblende, and amphibole are noted. Porosity is low to nonexistent. This sample is poorly sorted in the very fine grained range. The slickensides are possibly finer grained but this could be the typical range of grain sizes in the sample. There are possibly some aligned grains, but it is not clear. Poorly developed calcite slickenfibers show shallow oblique sinistral reverse fault movement.

Sample number: 7-10-3B

Location: Sand Canyon

Formation: Pennsylvanian Wild Cow

Orientation of slickenside and slickenlines: 42, 42 E rake 85 N
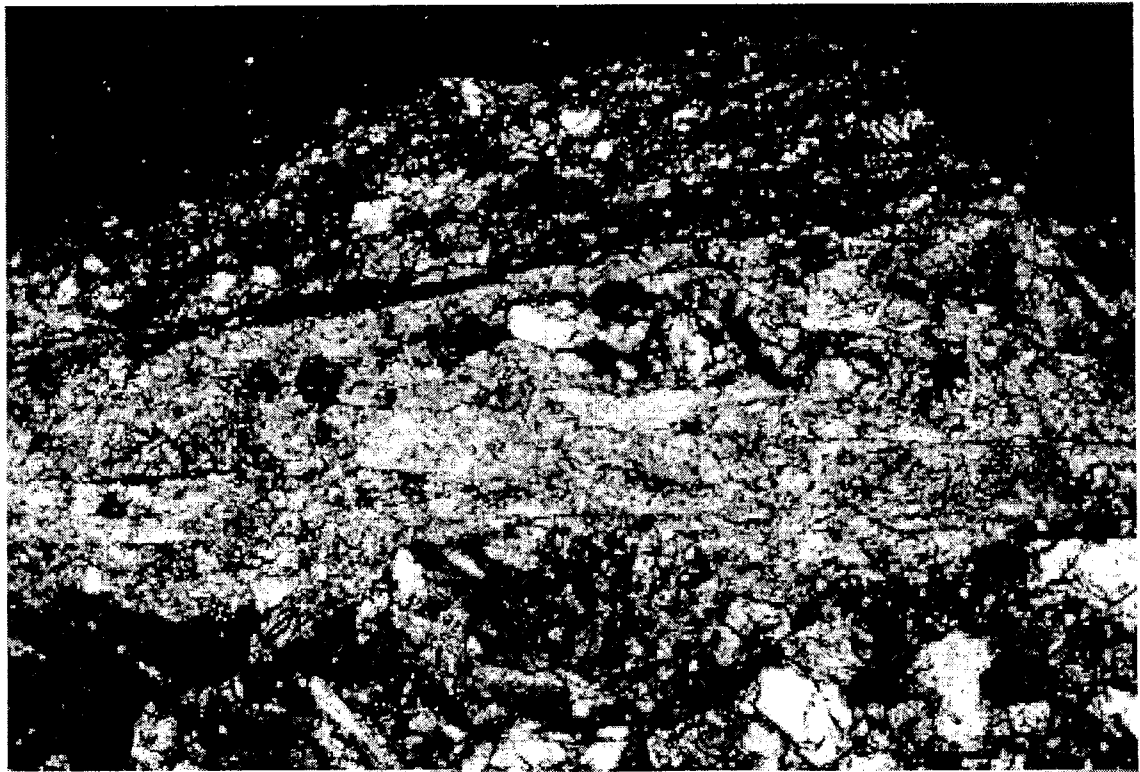
Hand Sample:

      Very fine-grained greenish-gray micaceous sandstone of quartz, epidote, and minor oxides. Slickenfibers indicate thrust motion. Sample is fractured along bedding planes with high mica content.

Thin Section:

      Thin section reveals fine-grained, closely packed immature sandstone with angular quartz, albite, kinked and pitted biotite, oxides, and clay. Chlorite and biotite are more concentrated on certain layers, often parallel to macroscopic fractures, probably bedding. A preferred orientation of biotite, chlorite, and quartz is noted parallel to bedding. Most of the slickenside was destroyed in thin section polishing, but where they remain, it is fine grained, fibrous, with some host material included. Two layers of carbonate fibers exist. The upper layer is foliated and contains host material. The lower layer is clean, fibrous carbonate. Sense of slip is reverse with a minor component of dextral slip.

Photomicrographs of the two layers of slickenfibers in sample 7-10-3B. Field of view is 2.6 mm. Photo on top was taken with plane polarized light, and on the bottom with crossed polars.

Sample number: 7-11-3A

Location: Sand Canyon

Formation: Precambrian Sais Quartzite

Orientation of slickenside and slickenlines: 295, 50 N rake 70 S

<u>Hand Sample</u>:

In hand sample this appears to be a quartzite but is actually a foliated quartz-rich schist. The slickensides are oriented 325, 51 N with slickenlines that rake 35 S. A poorly developed veneer of quartz marks the slickensides. The hand sample is predominantly quartz and oxides.

<u>Thin Section:</u>

In thin section this quartz-rich schist has variable grain size. The quartz grains show undulatory extinction and exist in a matrix of fine-grained quartz, mica, oxides, and clays. Micas and quartz grains appear to be aligned. Sense of slip appears to be dextral normal, but is poorly constrained.

Sample number: 7-11-6D

Location: Sand Canyon

Formation: Pennsylvanian Wild Cow

Orientation of slickenside and slickenlines: 315, 49 E rake 55 S
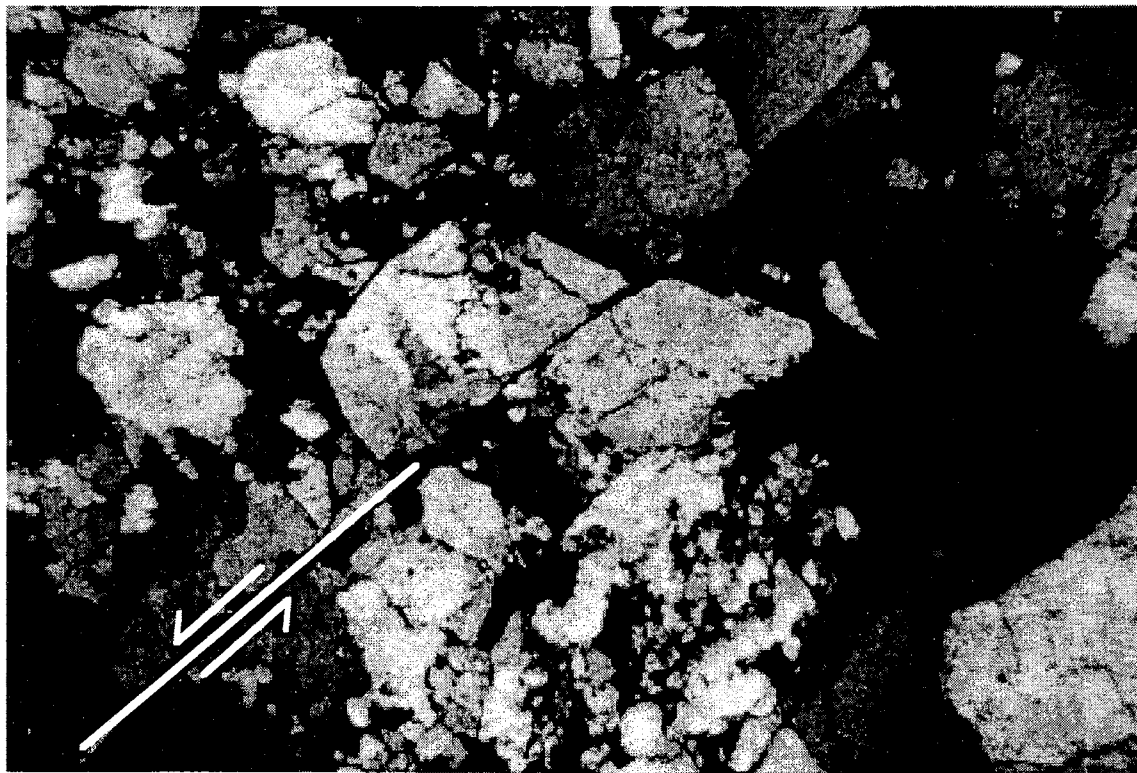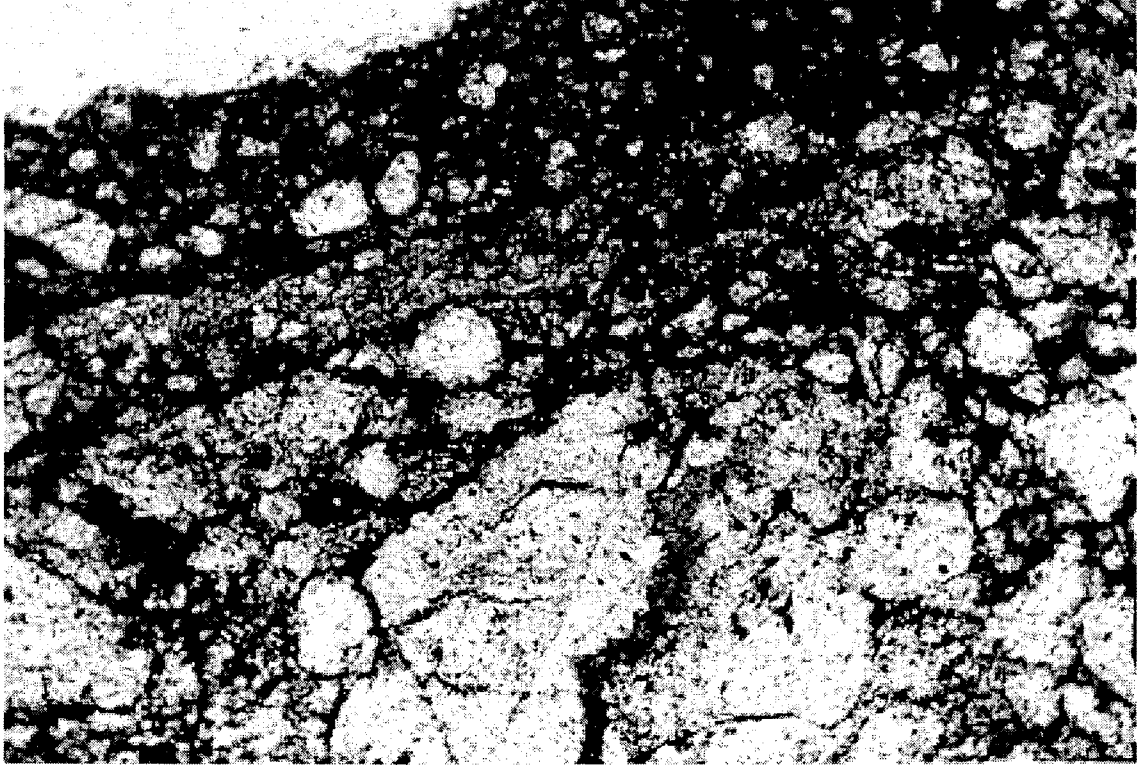
Hand Sample:

A coarse-grained sandstone with quartz, feldspar, and clay. Iron staining on the well developed slickensides. Two sets of lineations exist. The first set, raking 55S, shows normal dextral motion and is marked by crescent fractures and slickenlines on the uphill side of the ridges. The second set is not a slickenside set, but a set of orange-red ridges, possibly R shears.

Thin Section:

Sample is predominantly quartz sand. Grains are coarse, show undulatory extinction, are closely packed with linear margins and quartz overgrowths. Porosity has been reduced to 5% or less. There are zones of reduced grain size along the slickensides. In the reduced grain size areas there are clasts of iron oxide and quartz in a gray matrix. There are lots of fractured grains near these surfaces. One fractured grain shows left-lateral offset on minor planes. Overall the sample records dextral normal motion.

Photomicrographs of zone of reduced grain size in cross section of slickensides on sample 7-11-6D taken in plane light with a field of view of 2.6 mm., and a fractured grain showing sinistral offset along a minor fracture taken in cross polarized light with a 5.2mm field of view.

Sample number: 7-19-2C

Location: Sand Canyon

Formation: Precambrian schist

Orientation of slickenside and slickenlines: 355, 22 E raking 70 S

<u>Hand Sample</u>:

This fine-grained foliated schist has quartz, mica, and iron staining on the surface. Foliation has centimeter spacing.

<u>Thin Section:</u>

The thin section reveals very fine-grained quartz, oxides, and feldspar (?) interlayered with micaceous layers. The layers seem to be single long mica crystals. Two foliations are noted in thin section: the first is defined by aligned mica crystals, and the second by minor chlorite crystals. There are carbonate veins within the schist that are also crenulated. Sense of shear remains ambiguous.

Sample number: 7-19-5A

Location: Sand Canyon

Formation: Pennsylvanian Sandia

Orientation of slickenside and slickenlines: 62, 33 W raking 40 and 20 S

Hand Sample:

Sample is a coarse-grained sandstone with quartz, feldspar, mica, and clays. It has a greenish tint and slickensides on both the top and the bottom. Slickenside striae indicate dextral reverse motion.

Thin Section:

The thin section reveals 60% angular quartz grains that are deformed showing undulatory extinction and internal cracking. 30% of the rock is feldspar, which is also cracked and deformed and shows undulatory extinction. There is minor clay and biotite, and white mica. The carbonate cement is coarse- to fine-grained and locally twinned. Porosity is about 30% and seems to be reduced near the sample edges. The edges are in most places polished off.

Sample number: 7-19-5B

Location: Sand Canyon

Formation: Pennsylvanian Sandia

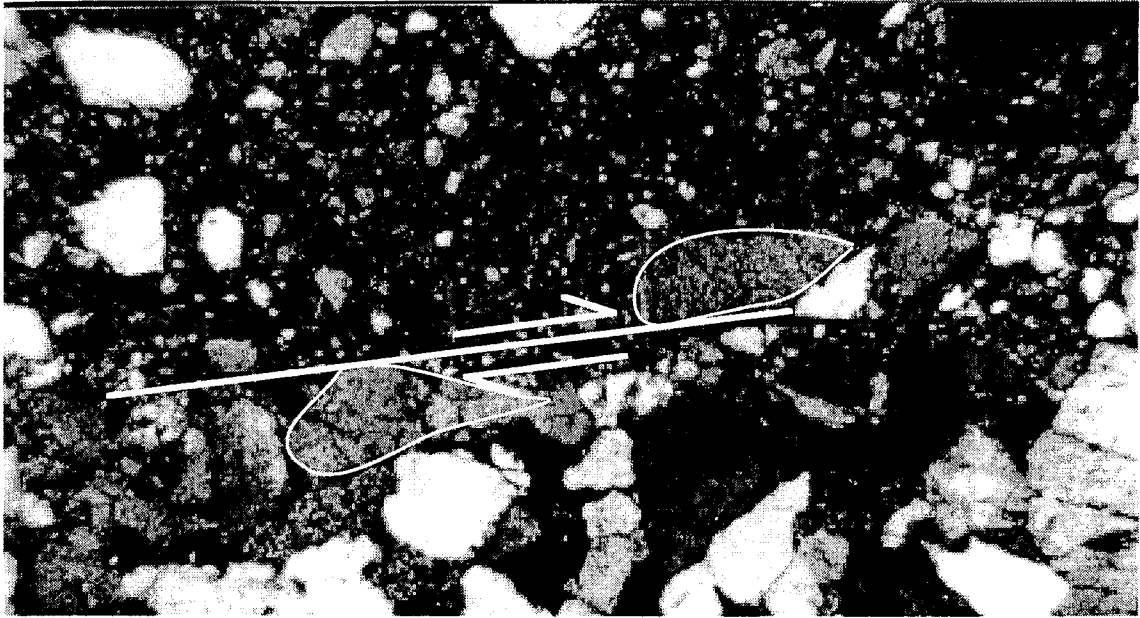Orientation of slickenside and slickenlines: 355, 51 E rake 35 S

<u>Hand Sample:</u>

This sample has well developed slickensides on a buff-colored, coarse- to medium-grained, quartz- feldspar sandstone of the Sandia formation. There are some dark bands and light bands in the rock that may be bedding, healed fractures, or solution fronts. The slickensides are 1-3mm thick veneers of white and orange cataclasite with very distinct slickenlines.

<u>Thin Section:</u>

In thin section there is a variation in grain size with proximity to the slip surfaces. Two centimeters from the slickensides the rock is predominantly dirty quartz sandstone. Porosity is about 10%. Grain boundaries are parallel, probably due to quartz overgrowths on the sedimentary grains. Some quartz shows undulatory extinction. Many grains are fractured internally. The cement is carbonate and clay. There is very minor iron staining along grain boundaries. Large grains are $1mm^2$, small grains are $0.1mm^2$. Near the slickenside, porosity decreases and carbonate increases. The veneer zone is composed of quartz grains ($< 0.25mm^2$) in an iron-stained carbonate matrix. The zone thickness varies from 0.25 to 1.25 mm wide in thin section. A subsidiary grain is fractured, showing dextral offset. There is evidence of dextral normal movement on the veneer surface: a large grain harboring smaller grains at the edge of the cataclasite, subsidiary grain-size reduced zones, and dragged grains at the coarse-fine boundary.

Photomicrograph of sample 7-19-5B in cross-polarized light showing a dextrally offset quartz grain at the margin of undeformed host and cataclasite. Field of view is 5.2mm.

Sample number: 8-10-1A

Location: Sand Canyon

Formation: Pennsylvanian Wild Cow

Orientation of slickenside and slickenlines: 328 19 N rake 50 S

Hand Sample:

Dark gray very fine-grained sandstone with thin carbonate coating defining slickenlines. Overall it has a greenish buff color.

Thin Section:

In thin section, angular quartz, feldspar, and lithics exist in a matrix of brown clay with minor mica. A preferred orientation of grains and cracks is noted. There are several fractured and offset grains. The slickenlines in hand sample are poorly developed. In thin section they appear to be very fine cataclasite layers of tiny quartz grains. Sense of shear appears to be thrust based on offset grains.

Sample number: 8-12-6A

Location: Railway cut

Formation: Pennsylvanian Wild Cow

Orientation of slickenside and slickenfibers: unknown

Hand Sample:

This sample is a coarse-grained fossiliferous gray limestone with veins of calcite and visible crinoid stems

Thin Section:

Sample contains 90% carbonate, mostly fine grained and some coarse grained. A few quartz grains that are deformed, showing grain boundary migration, exist in the matrix of carbonate. Several fossils are noted. In a few places, surfaces show millimeter offset, due to faulting or dissolution. Some quartz grains show extension fractures. Sense of shear is ambiguous.

Sample number: 8-15-1A

Location: Gallina Well

Formation: Permian Bernal

Orientation of slickenside and slickenside striae: 332, 25 N rake 55 S
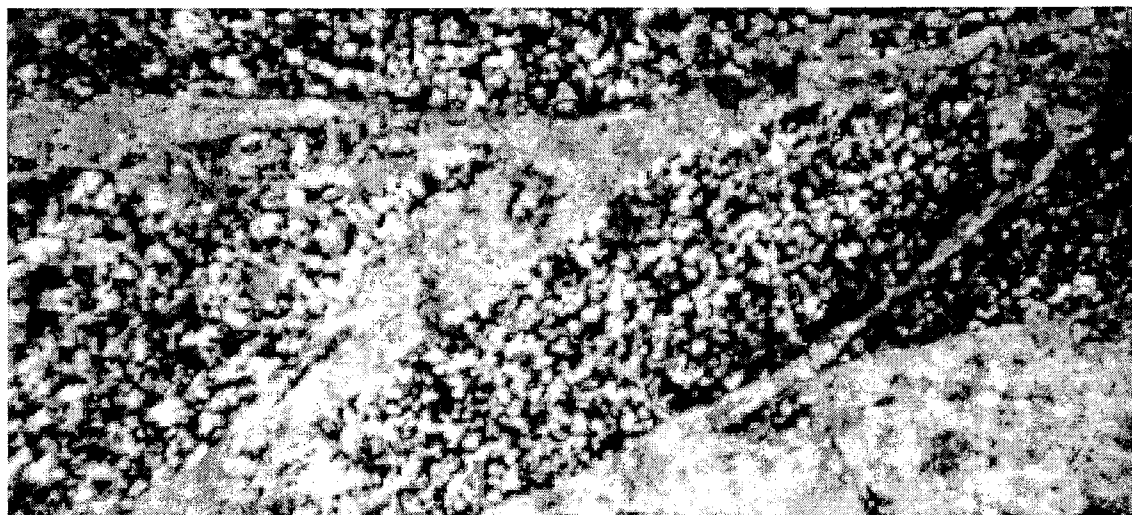
Hand Sample:

     This red, fine-grained mudstone with calcite veins and patches shows slickenlines on three surfaces that are parallel in transport direction and probably were formed at the same time. The slickensides are polished/veneer with the slickenside most poorly developed on the short surface. On the cut face there are visible white calcite veins, in a sigmoidal shape.

Thin Section:

     The rock is very -grained quartz, mica, oxides, and iron-stained cement. There is no noted grain size reduction on the veneer surface. There are lopsided rectangular features that indicate dextral motion on the largest surface, which would be, overall, dextral normal motion. There are offsets in the veins in the material. One shows distinct dextral movement, and another, nearly parallel, shows sinistral motion. The sigmoidal veins give a dextral sense of motion, which supports the normal motion.

     Photomicrograph of the fine-grained host siltstone with calcite veins in sample 8-15-1A. Photo was taken in cross-polarized light. Field of view is 5.2 mm.

Sample number: 8-15-1B
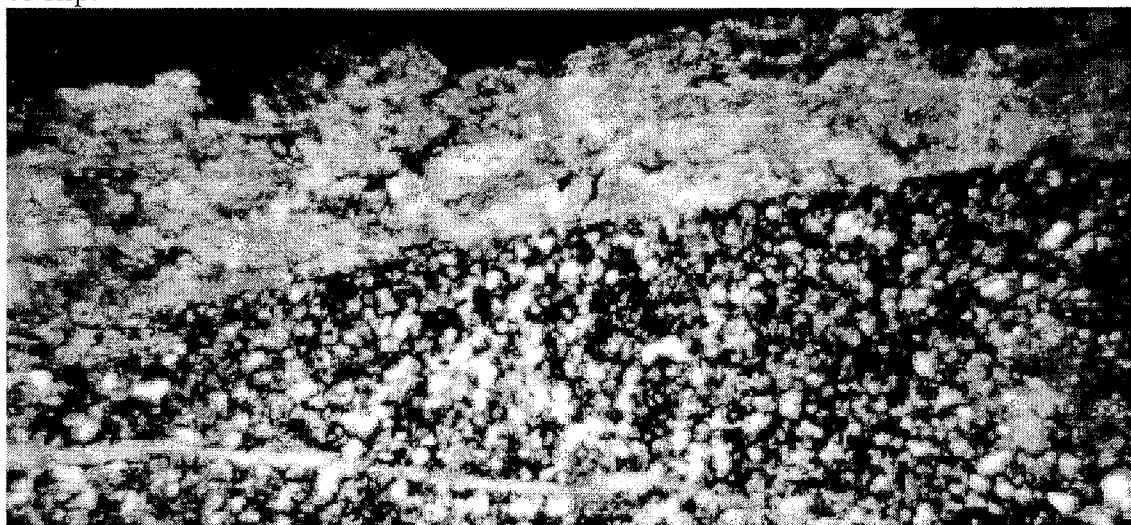
Location: Gallina Well

Formation: Permian Bernal

Orientation of slickenside and slickenlines: 38, 34 S rake 65 N

Hand Sample:

Slickenside striae are well developed, forming a thin veneer on the red, fine-grained sand to mudstone. There are calcite vein surfaces perpendicular to the slickensides. There is a little patch of buff-colored calcite slickenfibers on the slickensides.

Thin Section:

The thin section shows a very fine-grained subangular quartz, mica, feldspar , oxides, and organic material mudstone. The red color is iron staining of the cement. Porosity is very low. There is no grain-size reduction near the slickenside. A protective protrusion of coarse grains within the cataclasite with smaller grains next to it may indicate sense of slip. Calcite vein material appears to be fibrous, indicating dextral normal sense of slip.

Photomicrograph in cross-polarized light of the slickenfibers and fine-grained host mudstone of sample 8-15-1B. Field of view is 5.2 mm.

Sample number: 8-15-6A

Location: Gallina Well

Formation: Permian Bernal

Orientation of slickenside and slickenfibers: 66, 40 N rake 35 S

Hand Sample:

Hand sample is a red mudstone with gray limestone clasts. The slickenlines on top are patchy with buff-colored calcite slickenfibers. There is a vein shown on the cut face in side view. Examining the little bit exposed on another face reveals slickenfibers on that face. A clast (19mm across) is dextrally offset 9mm along the vein. In geographic coordinates this is interpreted as a thrust.

Thin Section:

In thin section there are gray and red areas. The gray areas are about 25% clastic sediments, angular to subrounded quartz, feldspar, mica, oxides, coral, shells, and amphibole. 75% is microcrystalline calcium carbonate. Dark curvy lines may represent solution seams which have concentrated clay material. The red areas are fine-grained sand consisting of angular quartz, mica, and feldspar. Everything is cemented with fine-grained, iron-stained calcite cement. There is no grain-size reduction along the slickensides. There is coarse calcite along the surface, which shows fibers in some places. They appear to indicate a dextral reverse sense of motion.

Sample number: 8-16-1A

Location: Gallina Well

Formation: Permian Abo

Orientation of slickenside and slickenlines: 51, 80 NW, 70 E

Hand Sample:

This type of slickenside striae is common in the field area. Looking at the hand sample a light and dark rind are noted on the edge. This may be carbonate and algae, or some other weathering rind.

Thin Section:

This sample is a very fine-grained quartz, oxides, minor mica, and carbonate mudstone. There is a possible mineral alignment. No grain-size reduction or porosity change is noted at the margins. The thin section does not reveal much about the slickenlines.

Sample number: 8-16-2A

Location: Gallina Well

Formation: Permian Abo

Orientation of slickenside and slickenlines: 000, 35 E rake 80 S

Hand Sample:

Competent, fine-grained red brown sand to mudstone. Primary sedimentary structures are evident on the cut face showing ripple laminations. The slickensides appear to be parallel to the ripple faces and have bleached white spots. Slickensides rake steeply south, and there appear to be Riedel shears indicating normal motion.

Thin Section:

The thin section reveals a very fine-grained angular quartz sandstone with red clay. Bedding is visible and distinguishable because of grain-size variations and concentrations of dark material, either clays or organic material. Tension (?) fractures are evident in thin section, often open or filled with carbonate cement. They seem to show a slight offset of bedding. They have synthetic sense of shear so they aren't R', and have too high of an angle to be P shears. Slickensides are locally parallel to ripple marks in bedding. The R fractures are visible but don't show offset.

Sample number: 8-16-6A

Location: Gallina Well

Formation: Permian Bernal

Orientation of slickenside and slickenlines: 28, 17 N rake 60 S

Hand Sample:

Hand sample is white to gray, sandy limestone with veins. There are two well developed slickenline sets on both the top and the bottom. Set 1 is on a good white veneer, with local 0.5 cm tall ridge and groove, and locally occurs on the red-brown iron-stained surface. Set 2 is mostly an iron-coated, patchy veneer on multiple surfaces. I believe these also have associated ridge and groove slickenside striae, but they have a greater amplitude and wavelength such that only one asymmetrical ridge exists on the sample. One broken face reveals that there are multiple movement surfaces in this rock.

Thin section:

There are coarse "new grains" of quartz, and fractured quartz, in a fine-grained carbonate mass with intense iron staining. The iron staining in hand sample is very red, fine-grained carbonate and quartz fragments in a cataclasite. A possible pulled-apart grain is noted near the boundary. It seems to be rotated counterclockwise, indicating purely reverse motion on a near vertical minor fault surface. There is not much for microscopic evidence of which direction or timing of movement. I suspect that set 2 came first, since it has the larger wavelength ridge and groove, and set 1 came later, built its own ridge and groove on smaller scale which would have been wiped out if set 1 occurred before set 2.

Sample number: 8-17-4A

Location: Gallina Well

Formation: Permian Bernal

Orientation of slickenside and slickenlines: 285, 74 N rake 70 W

Hand Sample:

Host rock is a sandstone with quartz, altered feldspar, and tension fractures. The slickenlines are calcite, epidote, and iron stained. There are two sets of slickenlines: the less prominent one is noted in the epidote and is 30° away from the main set. Slickensides are a distinct veneer, buff-colored, about one millimeter thick. The slickenlines are distinct.

Thin Section:

The thin section contains 80% closely packed, fine-grained quartz, brown clay stringers parallel to bedding, and carbonate-lined open fractures. The slickensides show up as a veneer of reduced grain-size in the host sandstone. No foliation is noted within the veneer, but fractures are noted.

Photomicrograph of iron-stained cataclasite of the slickensides in sample 8-17-4A. Photo was taken in cross-polarized light. Field of view is 5.2mm.
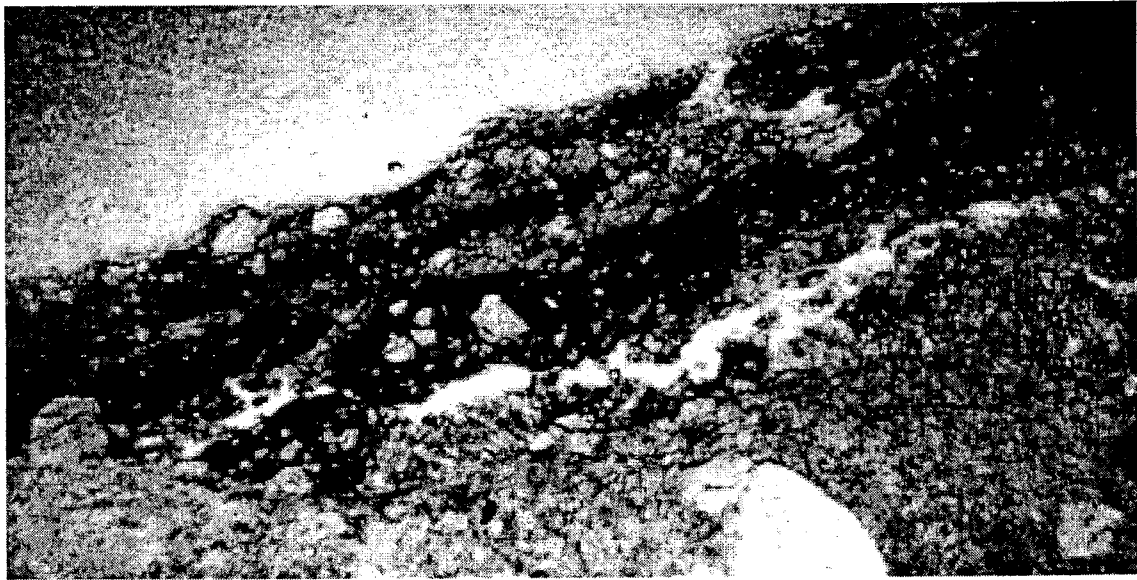
APPENDIX C

The trends of fold hinge traces and fold hinges were measured in the field and from the maps of other workers (Wilpolt and Wanek, 1951; Myers and McKay, 1974; Myers et al., 1981; Osburn, 1983; Colpitts, 1986; Myers et al., 1986; Brown, 1987; Cabezas, 1987). The general location of each fold hinge and the orientation of the Montosa fault at each location are listed. The internal angle of the fold and whether the fold is an anticline (A) or a syncline (S) is noted. If the fold is overturned, the letter O precedes A or S. Trend and plunge are listed, as is the reference to the map from which the measurements were taken.

Area	MF Orientation	Angle of fold	Anti or Syn	Trend	Plunge	Reference
Abo Pass	35	50	S	70 to 26		Myers, McKay, and Sharp, 1981
Abo Pass	30	90	A	5 to 70		Myers, McKay, and Sharp, 1981
Abo Pass	30	120	S	45		Myers, McKay, and Sharp, 1981
Abo Pass	5	113	A	25		Myers, McKay, and Sharp, 1981
Black Mesa	50		A	26		Wilpolt and Wanek, 1951
Black Mesa	40	120	S	15		Wilpolt and Wanek, 1951
Black Mesa	40		S	30		Wilpolt and Wanek, 1951
Black Mesa	40		S	340		Wilpolt and Wanek, 1951
Black Mesa	40		S	350		Wilpolt and Wanek, 1951
Black Mesa	40		A	4		Wilpolt and Wanek, 1951
Black Mesa	15	147	S	10		Cabezas, 1987
Black Mesa	15	140	A	25		Cabezas, 1987
Black Mesa	15	154	A	10		Cabezas, 1987
Black Mesa	35		A	55		Osborn, 1983
Black Mesa	15	135	S	35		Myers, Sharp, and McKay, 1986
Black Mesa	15	130	A	35-50		Myers, Sharp, and McKay, 1986
Black Mesa	15	150	S	30		Myers, Sharp, and McKay, 1986
Black Mesa	15	60	S	35		Myers, Sharp, and McKay, 1986
Black Mesa	15	35 (?)	A	30		Myers, Sharp, and McKay, 1986
Black Mesa	15	135	S	65		Myers, Sharp, and McKay, 1986
Black Mesa	40		S	8		Wilpolt and Wanek, 1951
Black Mesa	40		A	10		Wilpolt and Wanek, 1951
Black Mesa	40		A	26		Wilpolt and Wanek, 1951
Black Mesa	35		S	20		Osborn, 1983
Black Mesa	35		A	345	NW	Osborn, 1983
Black Mesa	20	149	a	20		Myers, Sharp, and McKay, 1986
Black Mesa	35		A	27		Cabezas, 1987
Black Mesa	45	155	A	20		Cabezas, 1987
Black Mesa	30	open	A	40		Myers, Sharp, and McKay, 1986
Black Mesa	30	open	S	50 to 35		Myers, Sharp, and McKay, 1986
Black Mesa	40		A	33		Cabezas, 1987
Black Mesa	40		A	40		Cabezas, 1987
Black Mesa	40	144	A	351		Cabezas, 1987
Black Mesa	40	148	A	354		Cabezas, 1987
Black Mesa	40		OS	22		Cabezas, 1987
Black Mesa	40		OS	30		Cabezas, 1987
Black Mesa	40		OS	5		Cabezas, 1987
Black Mesa	40	26	A	350	N	Cabezas, 1987
Black Mesa	40	156	A	237	SW	Cabezas, 1987
Black Mesa	40	141	S	230	SW	Cabezas, 1987
Black Mesa	40	161	A	230	SW	Cabezas, 1987
Black Mesa	40	148	A	330		Colpitts, 1986
Black Mesa	40	127	A	350		Colpitts, 1986
Black Mesa	45		S	20		Cabezas, 1987
Black Mesa	45		A	20		Cabezas, 1987
Black Mesa	45		S	10		Cabezas, 1987
Black Mesa	45		S	12		Cabezas, 1987
Black Mesa	45		A	14		Cabezas, 1987
Black Mesa	45		A	0		Cabezas, 1987
Black Mesa	45		S	11		Cabezas, 1987

Black Mesa	45		OA	12		Cabezas, 1987	
Black Mesa	45	146	S	1		Cabezas, 1987	
Black Mesa	45	44	A	12		Cabezas, 1987	
Black Mesa	45	143	A	348		Cabezas, 1987	
Black Mesa	35	140	A	50		Wilpolt and Wanek, 1951	
Gallina Well	35	156	A	315	nw	Brown, 1987	
Gallina Well	35	147	S	341	14	Brown, 1987	
Gallina Well	35	152	A	328		Cabezas, 1987	
Gallina Well	35	152	S	325		Cabezas, 1987	
Gallina Well	35	152	A	328		Cabezas, 1987	
Gallina Well	35	152	A	340		Cabezas, 1987	
Gallina Well	35	140	A	330		Cabezas, 1987	
Gallina Well	35		S	320		Cabezas, 1987	
Gallina Well	35		A	355	5	Brown, 1987	
Gallina Well	35	123	S	0	N	Brown, 1987	
Gallina Well	35	120	S	186	7	Brown, 1987	
Gallina Well	35		A	190	29	Brown, 1987	
Gallina Well	35	139	S	18	9	Brown, 1987	
Gallina Well	35	161	A	351	N	Brown, 1987	
Gallina Well	35	162	S	0	S	Brown, 1987	
Gallina Well	35	149	A	15	N	Brown, 1987	
Gallina Well	35	121	S	34	2	Brown, 1987	
Gallina Well	35	140	A	30 and 345		Cabezas, 1987	
Gallina Well	35		A	355		Cabezas, 1987	
Gallina Well	35		A	345		Cabezas, 1987	
Gallina Well	35		A	346		Cabezas, 1987	
Gallina Well	35		S	26		Cabezas, 1987	
Gallina Well	35		A	18		Cabezas, 1987	
Gallina Well	35		S	11		Cabezas, 1987	
Gallina Well	35		A	0-15		Cabezas, 1987	
Gallina Well	35		S	344		Cabezas, 1987	
Gallina Well	35	150	A	350		Wilpolt and Wanek, 1951	
Gallina Well	35		A	9		Wilpolt and Wanek, 1951	
Gallina Well	35		S	355		Wilpolt and Wanek, 1951	
Gallina Well	35	162	?	44	s	Behr	
Gallina Well	35	98	S	20	s	Behr	
Gallina Well	35	144	S	ne		Behr	
Gallina Well	35	155	A	325		Behr	
Gallina Well	35	150	?	357	n	Behr	
Gallina Well	35	150	A	22	s	Behr	
Gallina Well	35		S	306		Osborn, 1983	
Gallina Well	35		A	340		Osborn, 1983	
Gallina Well	35		A	300		Osborn, 1983	
Gallina Well	35		S	340		Osborn, 1983	
Gallina Well	35		A	340		Osborn, 1983	
Gallina Well	35		S	345	nw	Osborn, 1983	
Gallina Well	35		A	330-350		Osborn, 1983	
Gallina Well	35		A	15	ne	Osborn, 1983	
Gallina Well	35	156	S	100&65	10S	Brown, 1987	
Gallina Well	35	153	S	170	1	Brown, 1987	
Gallina Well	35	169	A	3	n	Brown, 1987	
Gallina Well	35	165	S	345	2	Brown, 1987	

Gallina Well	35	157	A	250		Brown, 1987	
Gallina Well	35	91	A	345		Brown, 1987	
Gallina Well	35	25	OA	340		Brown, 1987	
Gallina Well	35		A	340		Brown, 1987	
Gallina Well	35	103	S	10	12	Brown, 1987	
Gallina Well	35	147	S	350	n	Brown, 1987	
Gallina Well	35	153	S	300	nw	Colpitts, 1986	
Gallina Well	35	159	A	335		Colpitts, 1986	
Gallina Well	35	162	A	345	nw	Colpitts, 1986	
Gallina Well	35	123	A	350	nw	Colpitts, 1986	
Gallina Well	35	159	A	350	nw	Colpitts, 1986	

APPENDIX D

Lower hemisphere equal area plots of kinematic analyses of fault planes near the Montosa fault. The first section contains data from planes with known sense of shear. The second contains data from fault planes with inferred sense of shear. Plots are for the seven different areas studied, from north to south: Cañon Colorado, Sand Canyon, the railway cut, Sais Santa Fe Quarry, Parker Ranch, Gallina Well, and South Spring. Plots were created using FaultKin v.3.8.3a by R.W. Allmendinger, R.A. Marrett, and T. Cladouhos. The orientation of each plane and slickenline, in addition to the sense of slip, were entered into the program. The program then calculated the orientation of an auxiliary fault plane. The angle between the real fault and the auxiliary fault plane was then bisected by the axes of shortening and extension. The axes of shortening and extension were then plotted as dots and boxes, respectively, on equal area plots.
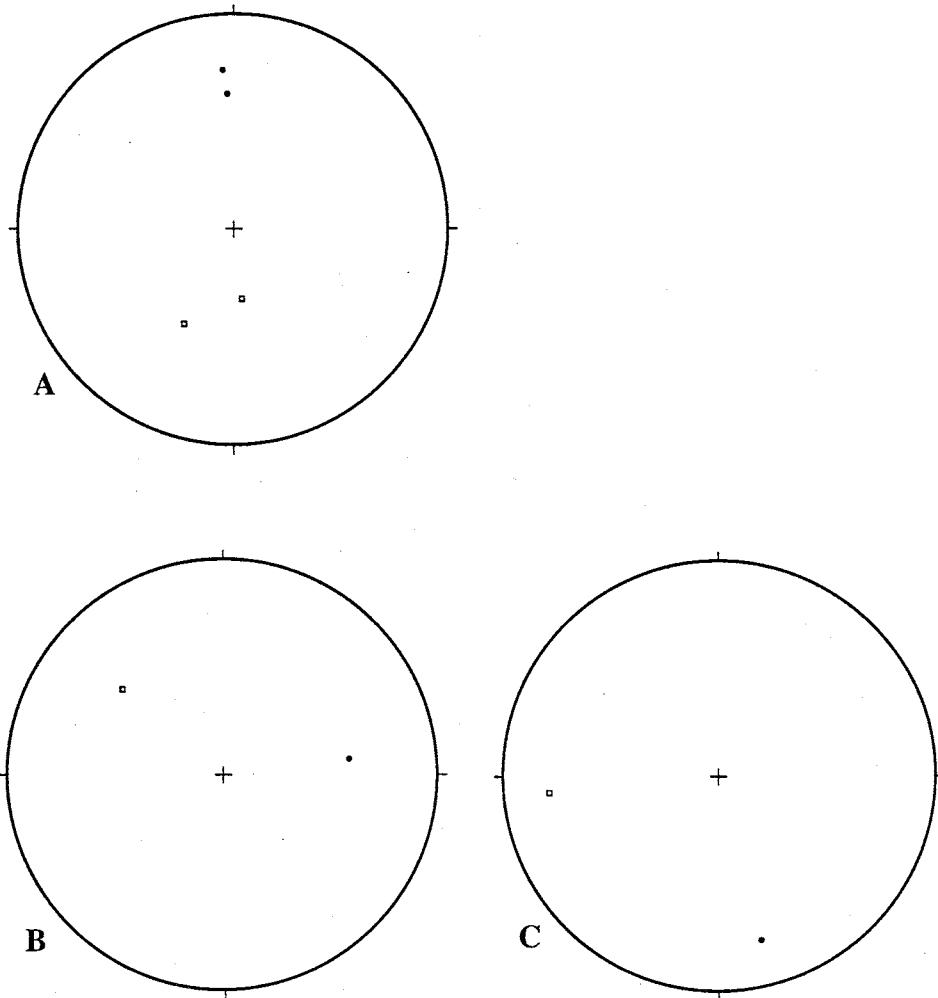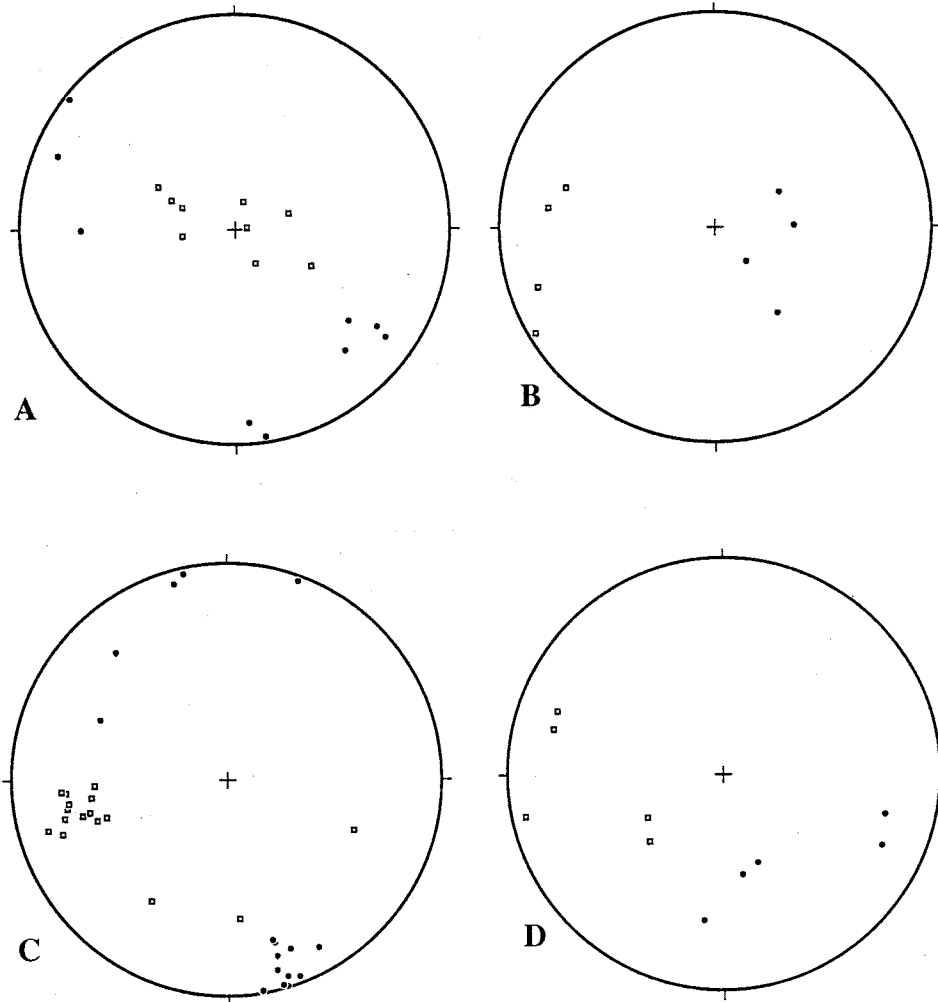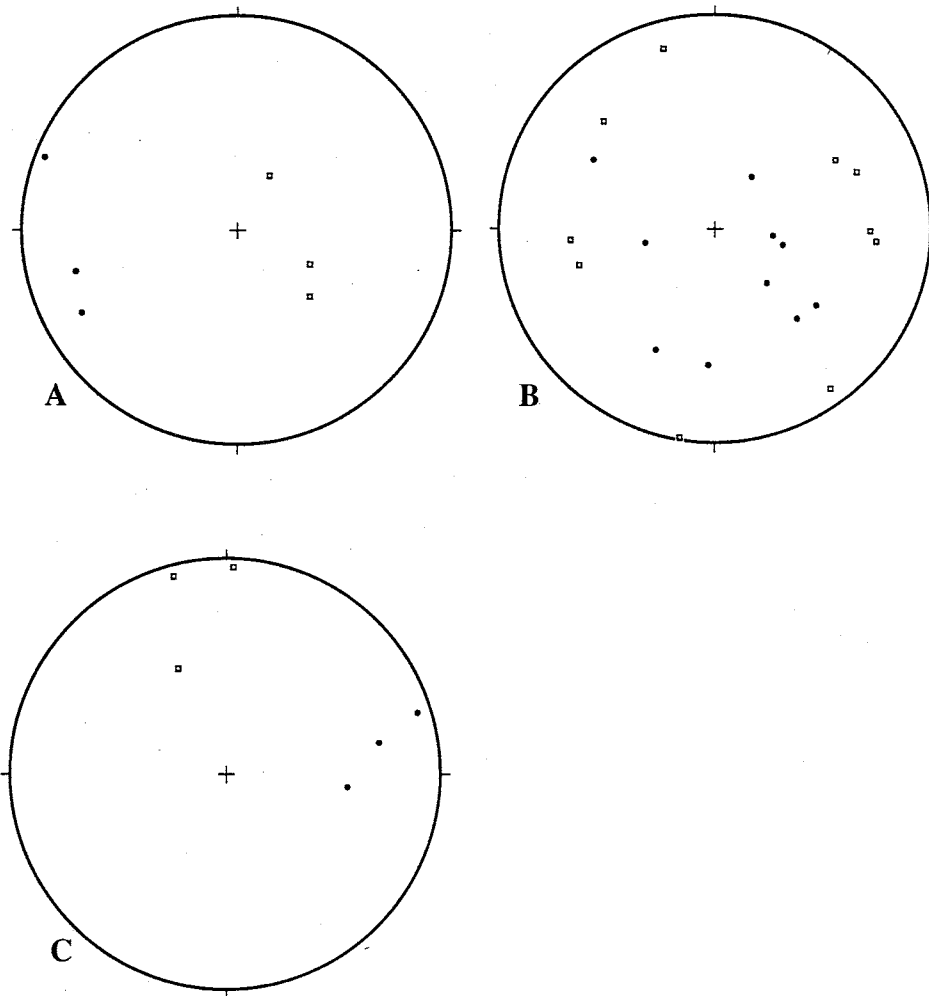
Lower hemisphere equal area plots of kinematic analysis of reverse (A), sinistral strike-slip (B), and dextral strike-slip (C) faults with known sense of slip at Cañon Colorado. Open squares are extension axes and dots are shortening axes.
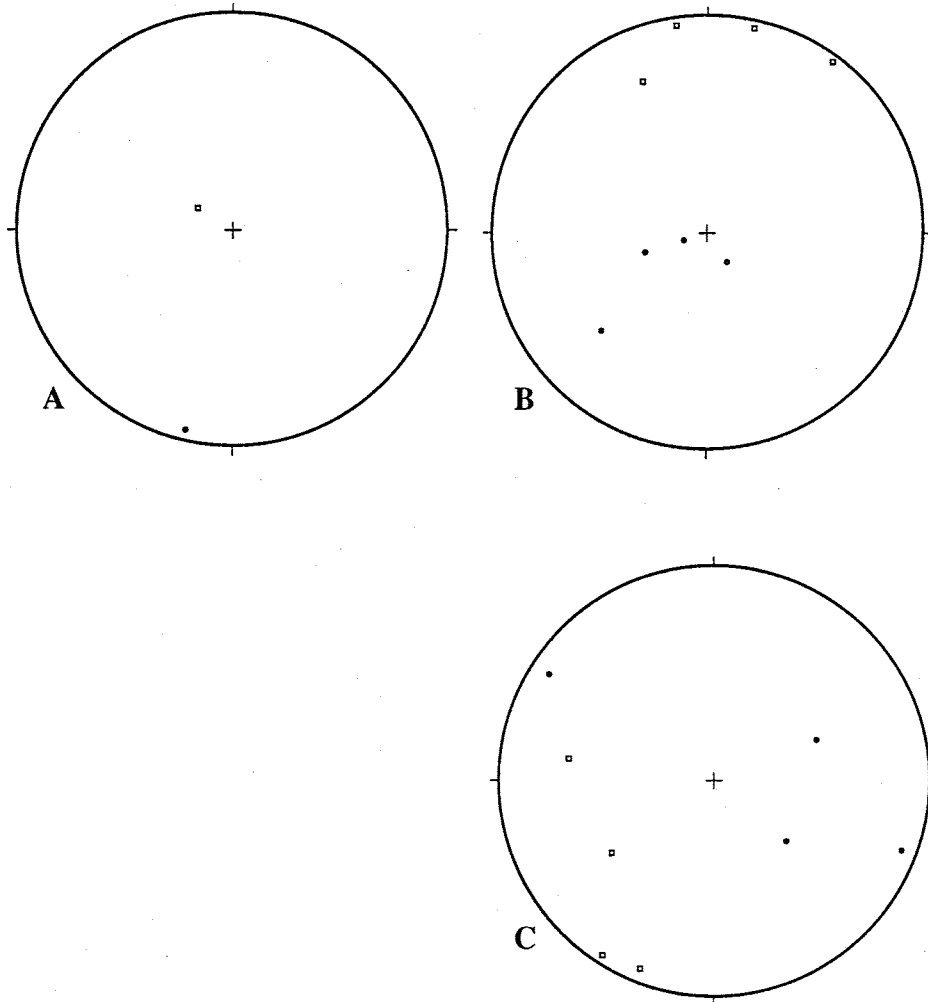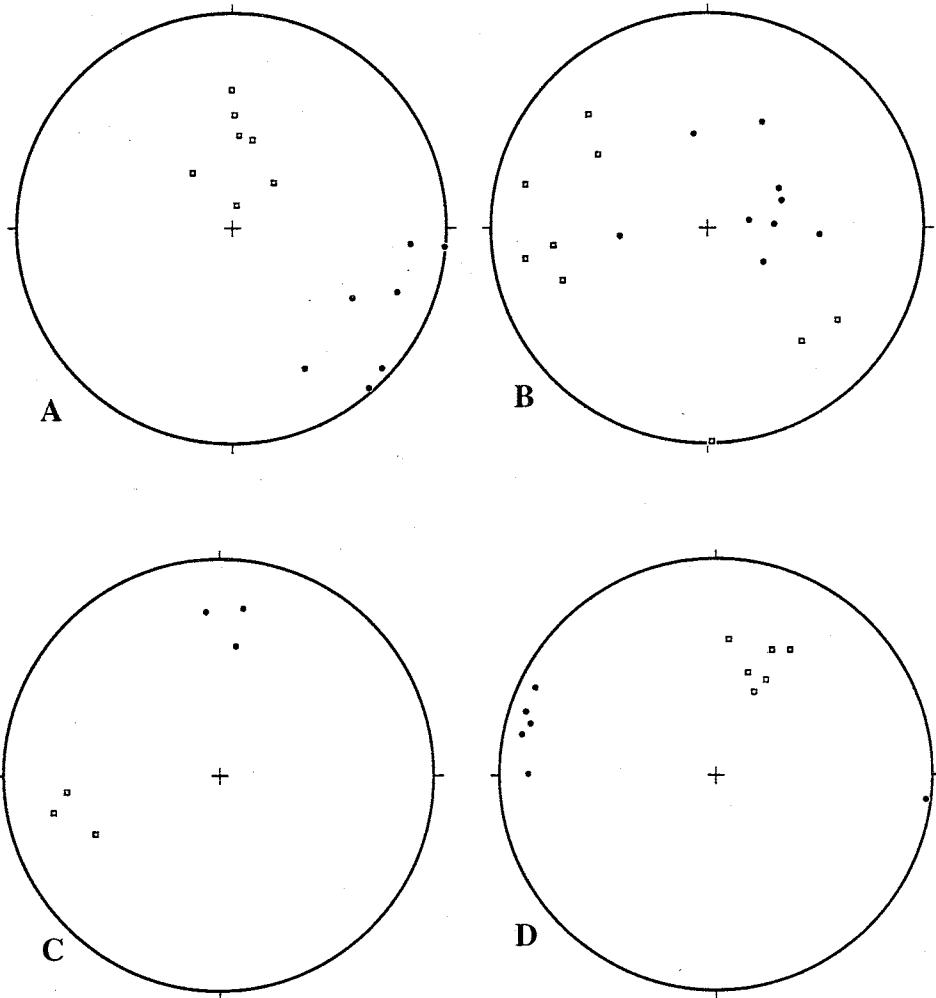
Lower hemisphere equal area plots of kinematic analysis of known reverse (A), normal (B), and dextral strike-slip (C) faults in Precambrian rocks at Sand Canyon. Open squares are extension axes and dots are shortening axes.
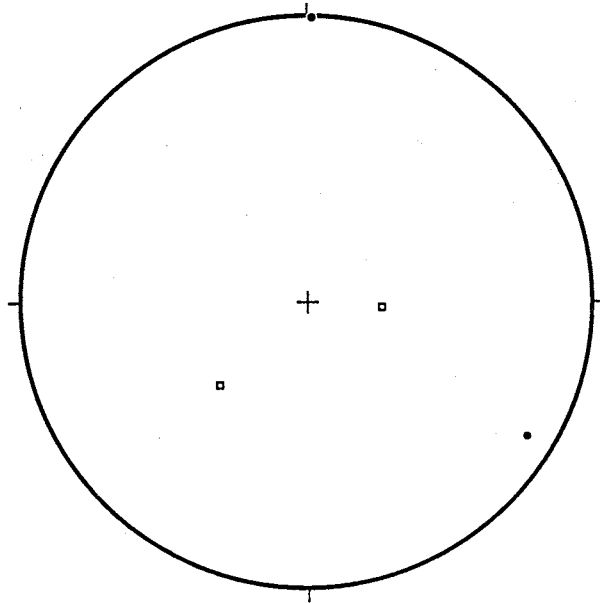
Lower hemisphere equal area plots of kinematic analysis of reverse (A), normal (B), sinistral strike-slip (C), and dextral strike-slip (D) faults with known sense of slip in Pennsylvanian rocks in Sand Canyon. Open squares are extension axes and dots are shortening axes.
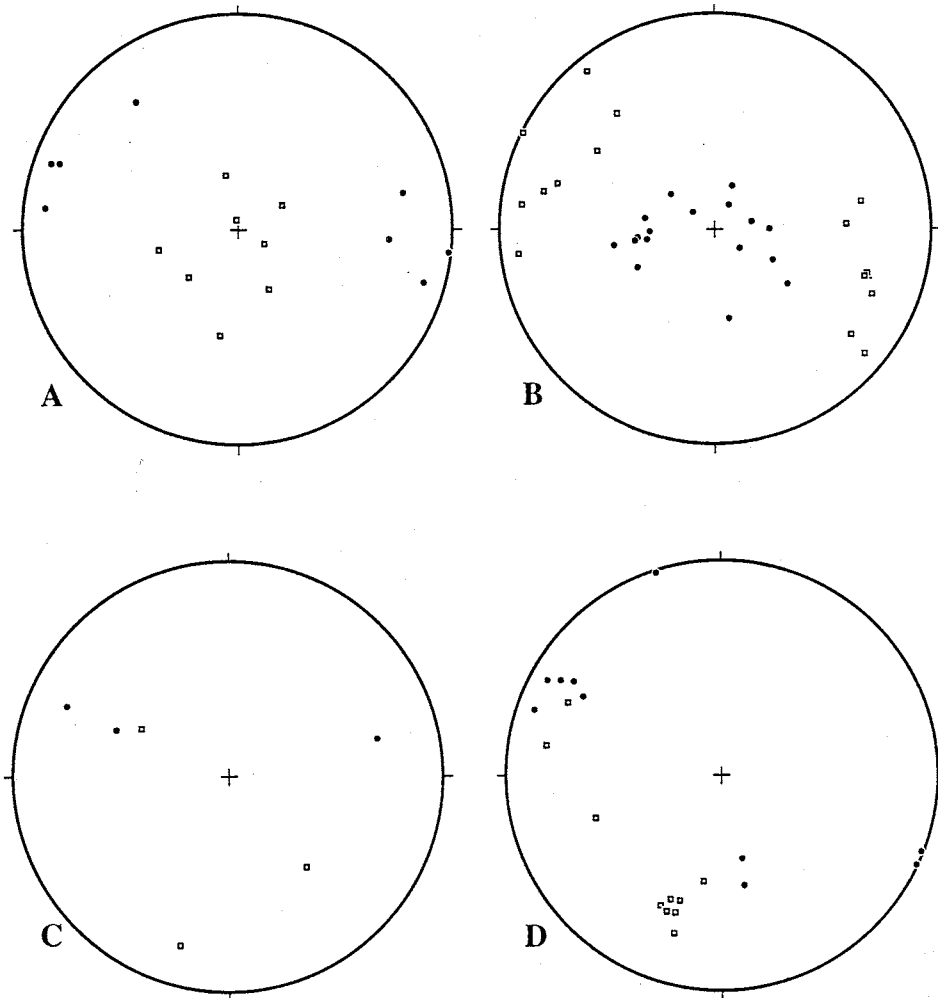
Lower hemisphere equal area plots of kinematic analysis of known reverse(A), normal (B), and sinistral strike-slip (C) faults in the railway cut. Open squares are extension axes and dots are shortening axes.
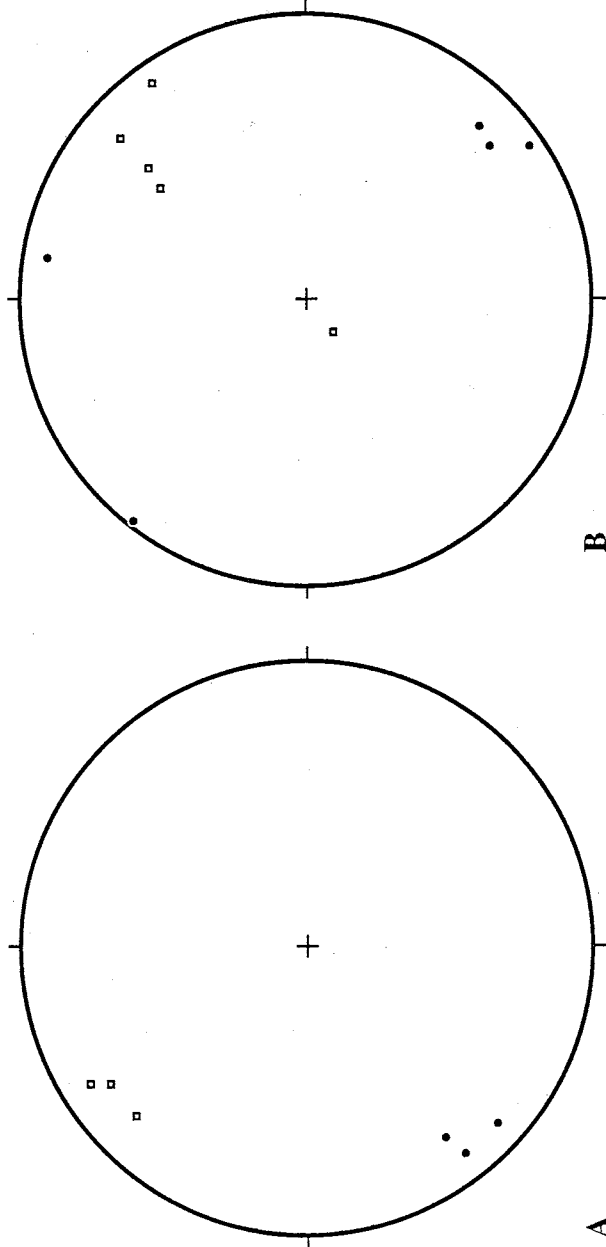
Lower hemisphere equal area plots of kinematic analysis of known reverse (A), normal (B), sinistral strike-slip (C), and dextral strike-slip (D) faults in Precambrian rocks at Sais Santa Fe Quarry. Open squares are extension axes and dots are shortening axes.

Lower hemisphere equal area plot of kinematic analysis of known reverse faults at Parker Ranch. Open squares are extension axes and dots are shortening axes.
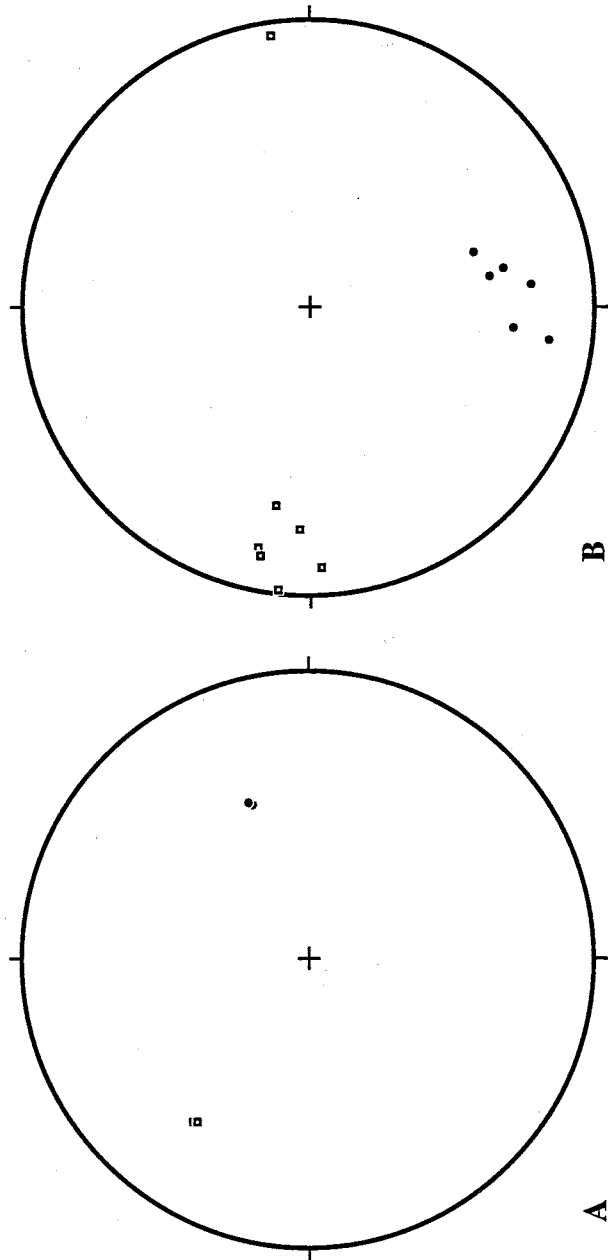
Lower hemisphere equal area plots of kinematic analysis of reverse (A), normal (B), sinistral strike-slip (C), and dextral strike-slip (D) faults at Gallina Well. Open squares are extension axes and dots are shortening axes.

Lower hemisphere equal area plots of kinematic analysis of sinistral strike-slip (A) and dextral strike-slip (B) faults at South Springs. Open squares are extension axes and dots are shortening axes.
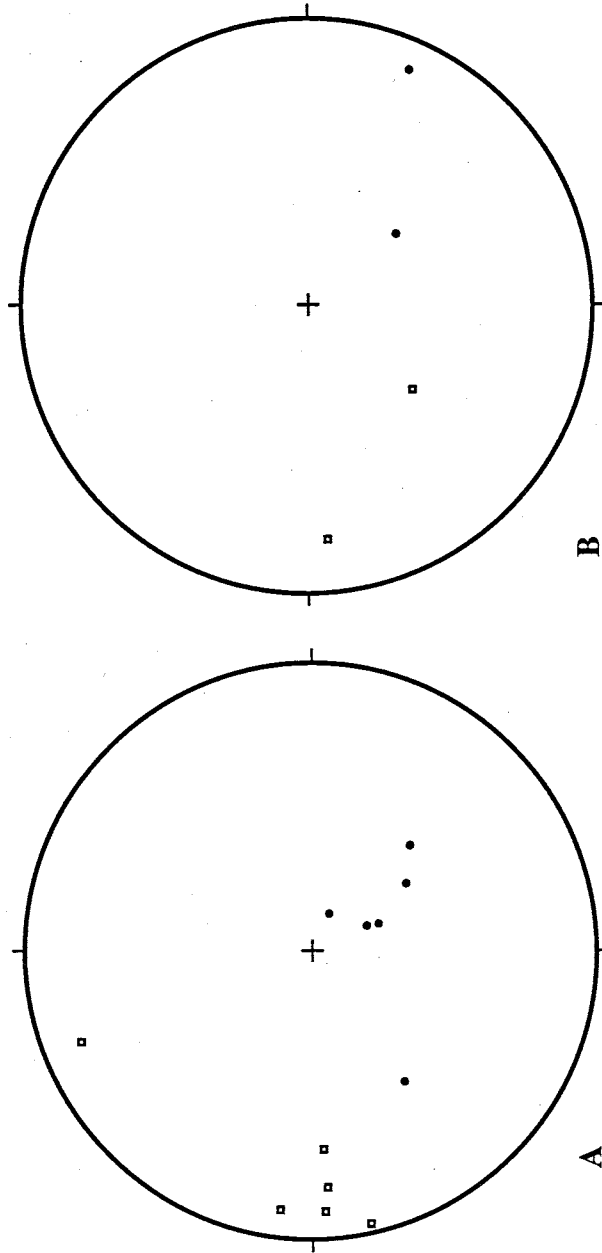
Lower hemisphere equal area plots of kinematic analysis of sinistral strike-slip (A) and dextral strike-slip (B) faults with inferred slip of shear at Cañon Colorado. Open squares are extension axes and dots are shortening axes.

Lower hemisphere equal area plots of kinematic analysis of normal (A) and dextral strike-slip (B) faults with inferred sense of slip found in Precambrian rocks in Sand Canyon. Open squares are extension axes and dots are shortening axes.
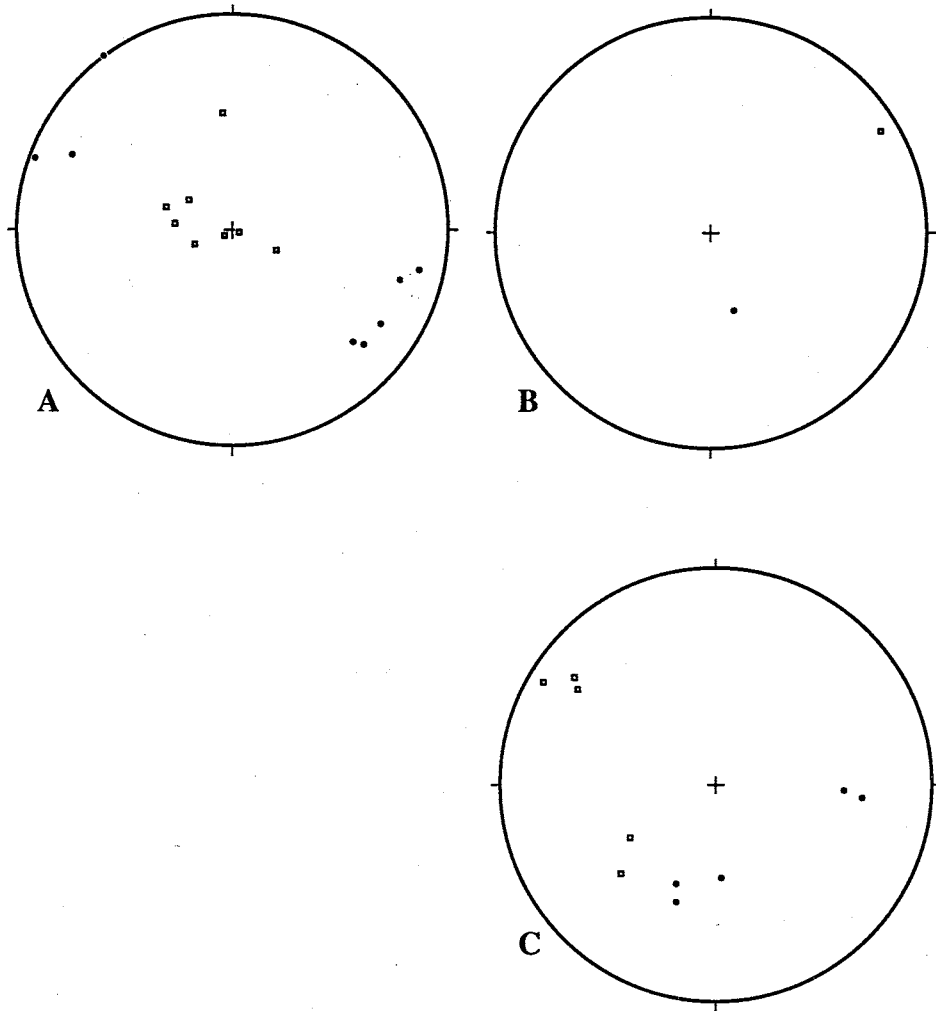
Lower hemisphere equal area plots of kinematic analysis of reverse (A), normal (B), and dextral strike-slip (C) faults with inferred sense of slip in Pennsylvanian rocks at Sand Canyon. Open squares are extension axes and dots are shortening axes.
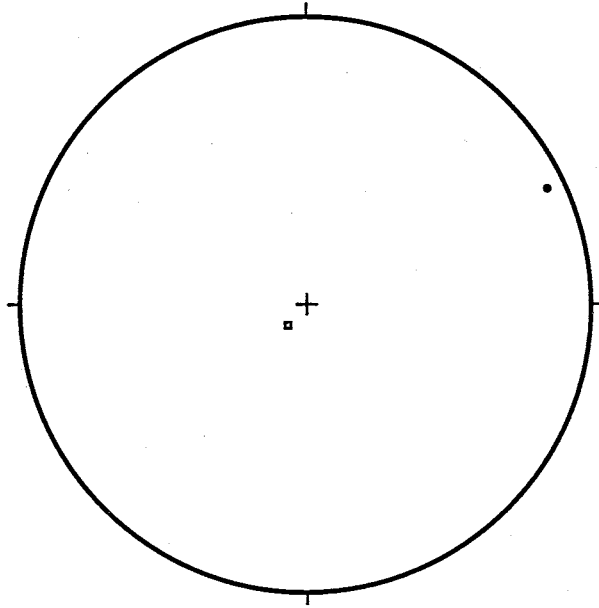
Lower hemisphere equal area plot of inferred thrust plane in Precambrain rock at the railway cut. Open squares are extension axes and dots are shortening axes.
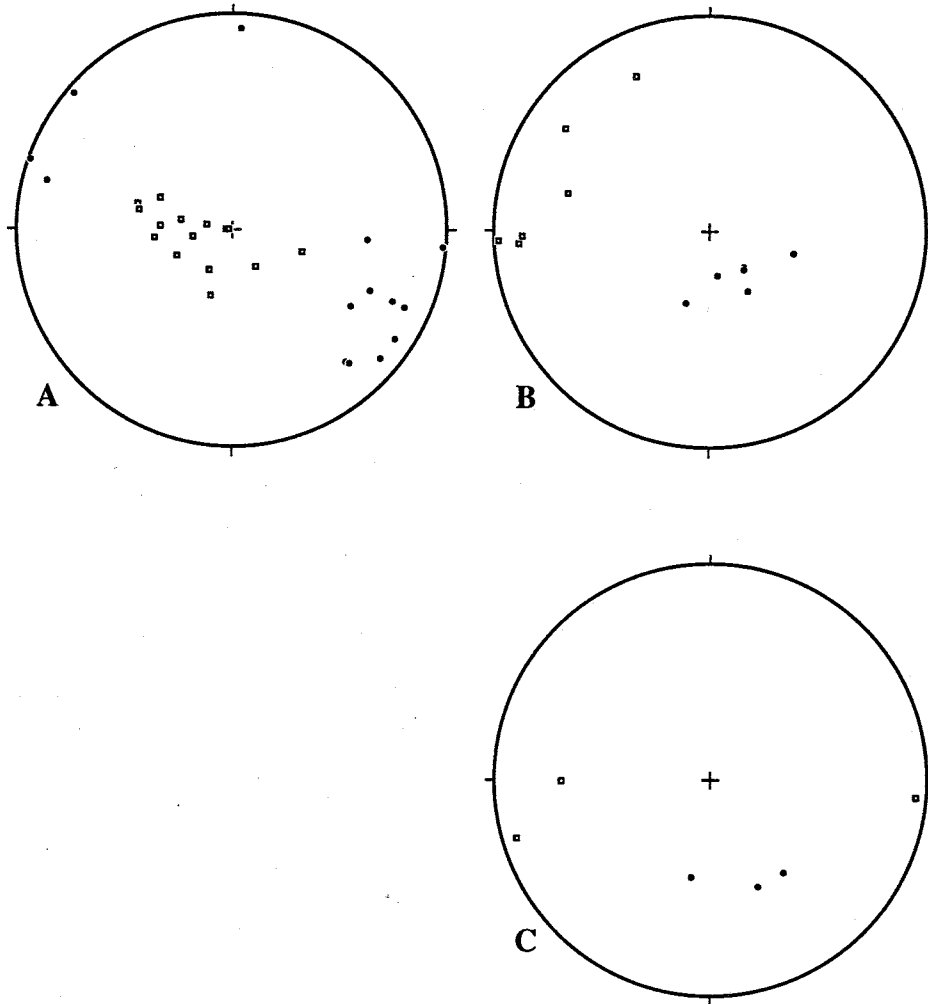
Lower hemisphere equal area plots of kinematic analysis of reverse (A), normal (B), and dextral strike-slip (C) faults with inferred sense of slip in Paleozoic rocks at Parker Ranch. Open squares are extension axes and dots are shortening axes.
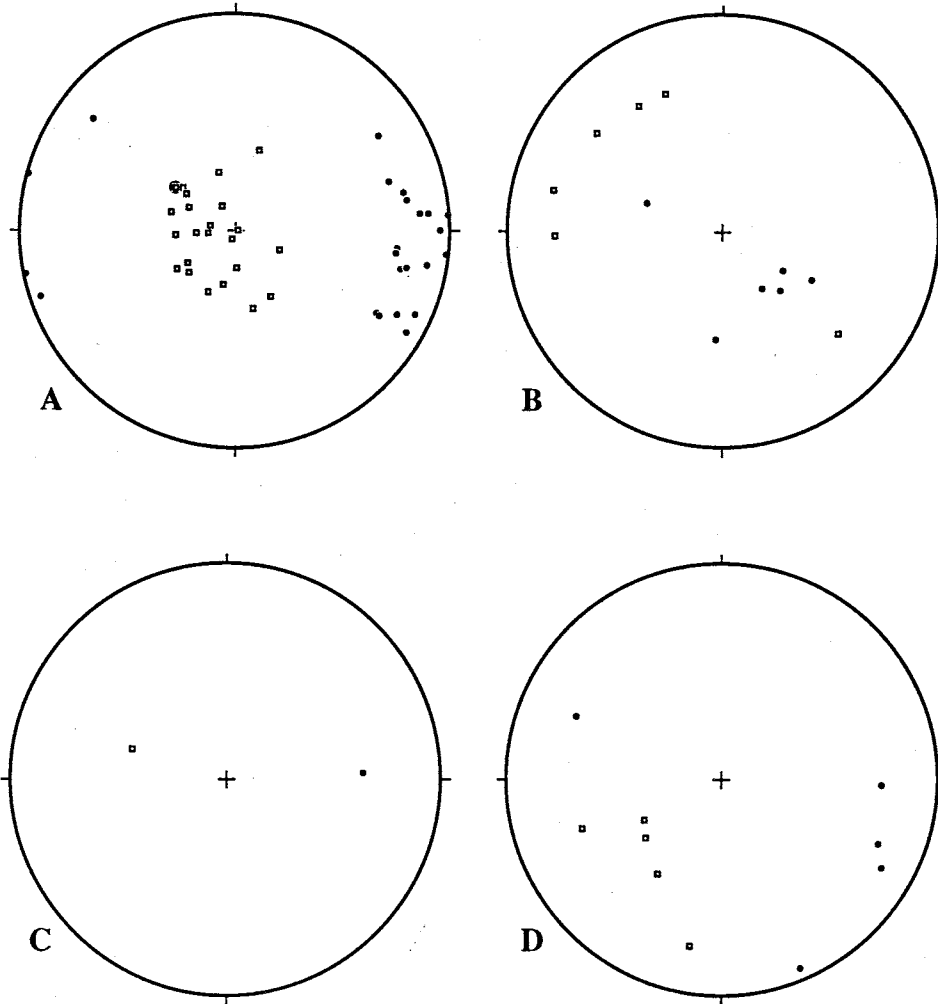
Lower hemishpere equal area plots of kinematic analysis of reverse (A), normal (B), sinistral strike-slip (C), and dextral strike-slip (D) faults with inferred sense of slip at Gallina Well. Open squares are extension axes and dots are shortening axes.

APPENDIX E

Data charts for the apatite fission-track samples collected in the Los Piños

and Manzano Mountains along the Montosa fault.

Map shows sample locations and numbers. Raw fission-track length and frequency data

are listed in the first chart. The next eight charts show fission-track age data for each

sample. Sample numbers are listed in bold in the upper left of each chart. Variables and

constants are listed below each sample number. The number of spontaneous (Ns) and

induced (Ni) fission tracks are listed per individual grain. Area counted for each grain is

also given. Age and standard deviation in millions of years are listed for each individual

grain. Pooled age is determined by summing the number of spontaneous and induced

tracks and utilizing the totals in the age equation. Mean age is determined by averaging

the individual grain ages.
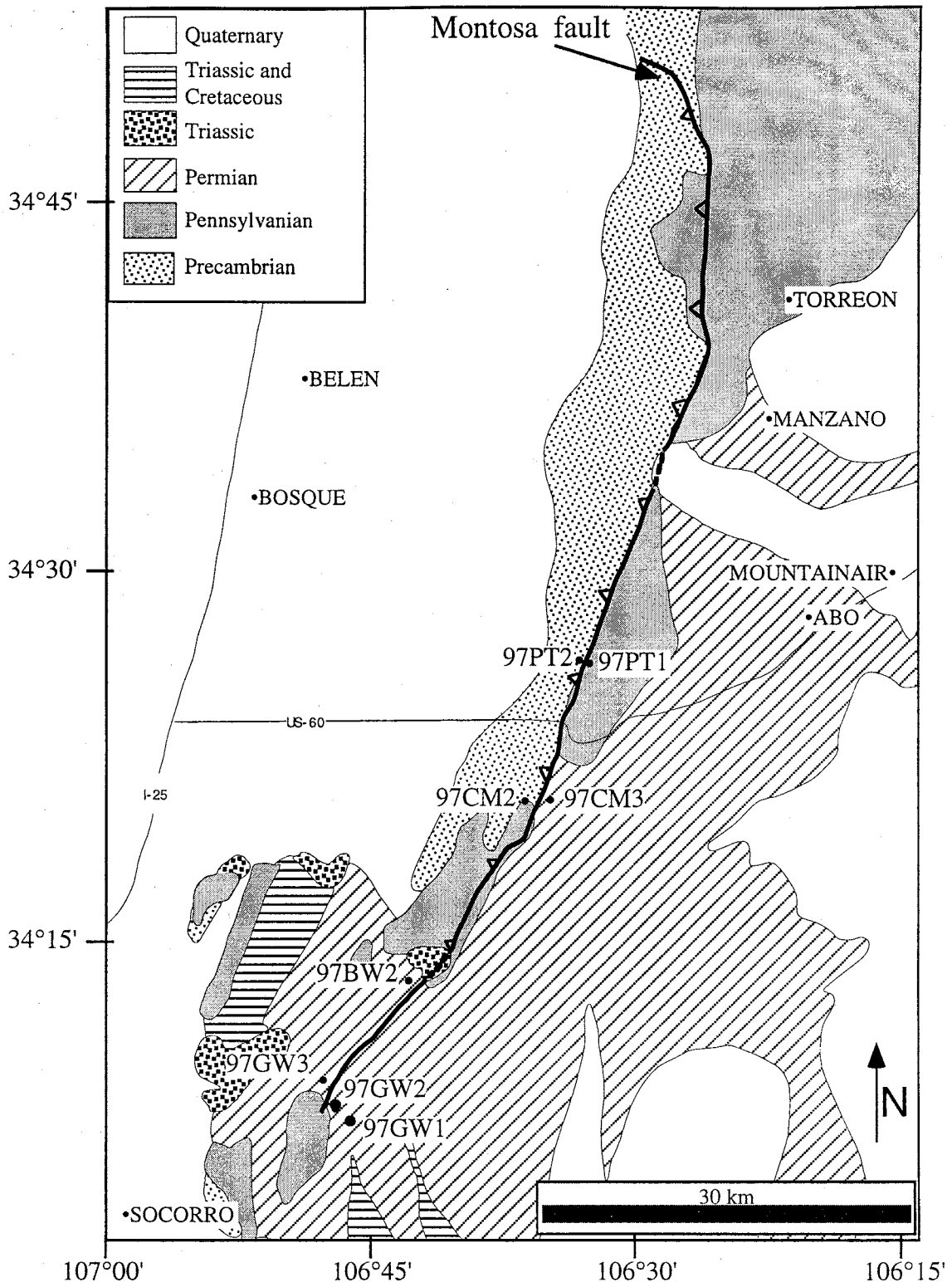
Sample numbers and locations along the Montosa fault.
Base map after New Mexico Geological Society (1982).

Sample	Frequency of fission tracks													Total number tracks	Mean track length (µm)	Stnd. Div (µm)	Std. Error (µm)
	6.5	7.5	8.5	9.5	10.5	11.5	12.5	13.5	14.5	15.5	16.5	17.5	18.5				
97BW2	0	0	0	0	5	0	1	3	0	1	0	0	0	10	12.0	2.0	1.3
97GW1	0	0	0	0	8	8	8	5	3	1	1	0	0	34	12.3	1.6	0.6
97GW2	0	0	1	5	3	8	6	7	10	4	5	2	0	51	13.1	2.3	0.6
97PT2	0	0	3	7	4	10	9	2	3	4	2	0	0	44	12.0	2.2	0.6

Raw apatite fission-track length data for the samples from the Los Piños and Manzano Mountains.

97BW2								
la	2E-10		U (ppm)=		9			
z	5420							
pm	170666							
g	0.5							
Nd	11053							
NS	Ni	area	ps	pi	age (Ma)	sdiv (Ma)		
1	9	1.40E-05	7.14E+04	6.43E+05	51.19	53.96		
0	28	4.50E-05	0.00E+00	6.22E+05	0.00	50.30		
1	12	3.00E-05	3.33E+04	4.00E+05	38.43	40.00		
1	22	1.00E-05	1.00E+05	2.20E+06	20.99	21.46		
2	31	9.20E-05	2.17E+04	3.37E+05	29.77	21.72		
2	74	1.00E-05	2.00E+05	7.40E+06	12.49	8.95		
8	86	1.10E-05	7.27E+05	7.82E+06	42.88	15.86		
2	38	2.50E-05	8.00E+04	1.52E+06	24.30	17.63		
3	28	2.50E-05	1.20E+05	1.12E+06	49.36	29.99		
0	4	3.50E-05	0.00E+00	1.14E+05	0.00	466.50		
0	13	2.80E-05	0.00E+00	4.64E+05	0.00	125.80		
1	25	1.90E-05	5.26E+04	1.32E+06	18.47	18.84		
1	39	4.30E-05	2.33E+04	9.07E+05	11.85	12.00		
3	28	5.00E-05	6.00E+04	5.60E+05	49.36	29.99		
1	23	2.80E-05	3.57E+04	8.21E+05	20.08	20.51		
1	23	3.40E-05	2.94E+04	6.76E+05	20.08	20.51		
1	21	3.20E-05	3.13E+04	6.56E+05	21.99	22.50		
2	13	3.00E-05	6.67E+04	4.33E+05	70.77	53.75		
2	96	8.00E-05	2.50E+04	1.20E+06	9.63	6.88		
2	21	4.00E-05	5.00E+04	5.25E+05	43.90	32.49		
34	634	6.81E-04	4.99E+04	9.31E+05	24.76	4.37	POOLED AGE	
					26.80	4.40	MEAN AGE	

97CM2								
la	2E-10		U (ppm)=	4				
z	4882.3							
pm	149300							
g	0.5							
Nd	11053							
NS	Ni	area	ps	pi	age (Ma)	sdiv (Ma)		
1	8	3.20E-05	3.13E+04	2.50E+05	45.80	48.70		
0	1	1.60E-05	0.00E+00	6.25E+04	0.00	2655.00		
2	18	3.20E-05	6.25E+04	5.63E+05	40.80	30.40		
1	4	3.20E-05	3.13E+04	1.25E+05	91.30	102.20		
1	5	1.60E-05	6.25E+04	3.13E+05	73.20	80.20		
1	12	1.00E-05	1.00E+05	1.20E+06	30.60	31.90		
2	7	9.60E-05	2.08E+04	7.29E+04	104.30	83.70		
1	4	3.20E-05	3.13E+04	1.25E+05	91.30	102.20		
0	2	3.20E-05	0.00E+00	6.25E+04	0.00	677.00		
1	12	1.60E-05	6.25E+04	7.50E+05	30.60	31.90		
1	5	1.60E-05	6.25E+04	3.13E+05	73.20	80.20		
0	1	3.20E-05	0.00E+00	3.13E+04	0.00	2655.00		
2	17	3.20E-05	6.25E+04	5.31E+05	43.10	32.30		
2	7	1.60E-05	1.25E+05	4.38E+05	104.30	83.70		
1	8	3.20E-05	3.13E+04	2.50E+05	45.80	48.70		
0	2	3.20E-05	0.00E+00	6.25E+04	0.00	677.00		
1	12	1.60E-05	6.25E+04	7.50E+05	30.60	31.90		
1	2	1.60E-05	6.25E+04	1.25E+05	181.40	222.30		
2	4	1.60E-05	1.25E+05	2.50E+05	181.40	157.30		
0	3	3.20E-05	0.00E+00	9.38E+04	0.00	352.00		
20	134	3.20E-05	6.25E+05	4.19E+06	54.70	13.40	POOLED AGE	
					58.60	12.40	MEAN AGE	

97CM3								
la	2E-10		U (ppm)=	8				
z	5420							
pm	170666							
g	0.5							
ND	11053							
NS	Ni	area	ps	pi	age (Ma)	sdiv (Ma)		
0	9	3.60E-05	0.00E+00	2.50E+05	0.00	189.20		
10	83	3.30E-05	3.03E+05	2.52E+06	55.48	18.58		
2	37	1.20E-05	1.67E+05	3.08E+06	24.95	18.12		
1	6	2.30E-05	4.35E+04	2.61E+05	76.63	82.77		
0	4	5.00E-05	0.00E+00	8.00E+04	0.00	466.50		
0	23	1.50E-05	0.00E+00	1.53E+06	0.00	62.50		
0	2	1.50E-05	0.00E+00	1.33E+05	0.00	1354.20		
0	7	2.50E-05	0.00E+00	2.80E+05	0.00	267.90		
13	171	2.09E-04	6.22E+04	8.18E+05	35.10	10.11	POOLED AGE	
					19.70	14.10	MEAN AGE	

97GW1								
la	2E-10		U (ppm)=	35				
z	4882.3							
pm	149300							
g	0.5							
Nd	11053							
NS	Ni	area	ps	pi	age (Ma)	sdiv (Ma)		
3	82	2.30E-05	1.30E+05	3.57E+06	14.00	8.20		
2	43	2.20E-05	9.09E+04	1.95E+06	17.80	12.90		
1	14	3.70E-05	2.70E+04	3.78E+05	27.30	28.30		
3	66	5.50E-05	5.45E+04	1.20E+06	17.40	10.30		
5	59	1.30E-05	3.85E+05	4.54E+06	32.40	15.10		
4	79	1.80E-05	2.22E+05	4.39E+06	19.40	10.00		
8	130	2.80E-05	2.86E+05	4.64E+06	23.50	8.60		
0	3	1.40E-05	0.00E+00	2.14E+05	0.00	352.00		
2	14	1.60E-05	1.25E+05	8.75E+05	54.50	41.20		
6	59	5.10E-05	1.18E+05	1.16E+06	38.80	16.70		
4	41	4.00E-05	1.00E+05	1.03E+06	37.30	19.60		
2	39	2.60E-05	7.69E+04	1.50E+06	19.60	14.20		
1	7	2.00E-05	5.00E+04	3.50E+05	54.50	58.30		
2	55	3.50E-05	5.71E+04	1.57E+06	13.90	10.00		
2	41	1.70E-05	1.18E+05	2.41E+06	18.70	13.50		
4	50	3.90E-05	1.03E+05	1.28E+06	30.60	15.90		
6	51	4.00E-05	1.50E+05	1.28E+06	44.90	19.50		
9	134	5.80E-05	1.55E+05	2.31E+06	25.70	8.90		
1	15	2.50E-05	4.00E+04	6.00E+05	25.50	26.30		
9	159	4.80E-05	1.88E+05	3.31E+06	21.60	7.50		
74	1141	6.25E-04	1.18E+05	1.83E+06	23.60	2.85	POOLED AGE	
					25.60	2.90	MEAN AGE	

97GW2							
la	1.6E-10		U (ppm)=	26			
z	5420						
pm	170666						
g	0.5						
Nd	11053						
NS	Ni	area	ps	pi	age (Ma)	sdiv (Ma)	
12	501	1.45E-04	8.28E+04	3.46E+06	11.07	3.23	
4	147	6.00E-05	6.67E+04	2.45E+06	12.57	6.37	
4	223	7.20E-05	5.56E+04	3.10E+06	8.29	4.18	
22	661	1.16E-04	1.90E+05	5.70E+06	15.38	3.34	
4	102	9.00E-05	4.44E+04	1.13E+06	18.11	9.23	
3	91	1.00E-04	3.00E+04	9.10E+05	15.23	8.94	
2	110	8.00E-05	2.50E+04	1.38E+06	8.40	6.00	
2	97	1.90E-05	1.05E+05	5.11E+06	9.53	6.81	
6	201	4.00E-05	1.50E+05	5.03E+06	13.79	5.72	
3	56	6.00E-05	5.00E+04	9.33E+05	24.73	14.66	
4	140	7.10E-05	5.63E+04	1.97E+06	13.20	6.70	
2	28	2.50E-05	8.00E+04	1.12E+06	32.95	24.12	
2	78	7.30E-05	2.74E+04	1.07E+06	11.85	8.49	
6	372	8.00E-05	7.50E+04	4.65E+06	7.46	3.07	
8	172	1.00E-04	8.00E+04	1.72E+06	21.48	7.77	
3	61	5.00E-05	6.00E+04	1.22E+06	22.71	13.43	
7	137	1.00E-04	7.00E+04	1.37E+06	23.59	9.14	
1	37	5.50E-05	1.82E+04	6.73E+05	12.49	12.66	
1	52	3.20E-05	3.13E+04	1.63E+06	8.89	8.97	
2	104	4.70E-05	4.26E+04	2.21E+06	8.89	6.35	
6	74	5.00E-05	1.20E+05	1.48E+06	37.39	15.88	
3	132	5.00E-05	6.00E+04	2.64E+06	10.50	6.13	
4	210	5.00E-05	8.00E+04	4.20E+06	8.80	4.44	
4	89	2.50E-05	1.60E+05	3.56E+06	20.75	10.61	
14	304	5.00E-05	2.80E+05	6.08E+06	21.26	5.82	
5	97	2.50E-05	2.00E+05	3.88E+06	23.80	10.92	
134	4276	1.67E-03	8.05E+04	2.57E+06	14.50	1.90	POOLED AGE
					16.30	1.30	MEAN AGE

97GW3								
la	2E-10		U (ppm)=	30				
z	4882.3							
pm	149300							
g	0.5							
ND	11053							
NS	Ni	area	ps	pi	age (Ma)	sdiv (Ma)		
3	46	3.20E-05	9.38E+04	1.44E+06	24.50	14.70		
5	133	3.20E-05	1.56E+05	4.16E+06	14.20	6.50		
6	72	3.20E-05	1.88E+05	2.25E+06	31.30	13.40		
3	84	3.20E-05	9.38E+04	2.63E+06	13.40	7.90		
3	92	3.20E-05	9.38E+04	2.88E+06	21.30	7.20		
5	2	3.20E-05	1.56E+05	6.25E+04	26.10	12.10		
1	20	3.20E-05	3.13E+04	6.25E+05	18.80	19.30		
0	4	1.60E-05	0.00E+00	2.50E+05	0.00	233.00		
3	44	3.20E-05	9.38E+04	1.38E+06	25.60	15.30		
2	27	1.60E-05	1.25E+05	1.69E+06	27.90	20.50		
2	9	3.20E-05	6.25E+04	2.81E+05	83.20	65.20		
6	124	3.20E-05	1.88E+05	3.88E+06	18.20	7.70		
0	9	3.20E-05	0.00E+00	2.81E+05	0.00	85.00		
7	140	3.20E-05	2.19E+05	4.38E+06	18.80	7.30		
5	49	3.20E-05	1.56E+05	1.53E+06	38.30	18.10		
2	44	1.60E-05	1.25E+05	2.75E+06	17.10	12.40		
2	27	1.60E-05	1.25E+05	1.69E+06	27.90	20.50		
3	44	1.60E-05	1.88E+05	2.75E+06	25.60	15.30		
1	5	1.60E-05	6.25E+04	3.13E+05	75.00	82.20		
4	33	3.20E-05	1.25E+05	1.03E+06	45.50	24.20		
63	1008	5.44E-04	1.16E+05	1.85E+06	22.70	2.97	POOLED AGE	
					70.30	44.30	MEAN AGE	

97PT1							
la	1.6E-10		U (ppm)=	19			
z	4882.3						
pm	149300						
g	0.5						
ND	11053						
NS	Ni	area	ps	pi	age (Ma)	sdiv (Ma)	
2	22	1.60E-05	1.25E+05	1.38E+06	32.8	24.3	
0	8	6.40E-05	0.00E+00	1.25E+05	0.0	100.0	
5	57	3.20E-05	1.56E+05	1.78E+06	31.7	14.8	
4	36	1.60E-05	2.50E+05	2.25E+06	40.1	21.2	
1	5	3.20E-05	3.13E+04	1.56E+05	72.0	78.9	
5	53	3.20E-05	1.56E+05	1.66E+06	34.1	16.0	
8	61	3.20E-05	2.50E+05	1.91E+06	47.3	17.9	
10	107	6.40E-05	1.56E+05	1.67E+06	33.7	11.3	
1	15	3.20E-05	3.13E+04	4.69E+05	24.1	24.9	
7	81	6.40E-05	1.09E+05	1.27E+06	31.2	12.4	
3	54	3.20E-05	9.38E+04	1.69E+06	20.1	11.9	
4	44	3.20E-05	1.25E+05	1.38E+06	32.8	17.2	
3	32	3.20E-05	9.38E+04	1.00E+06	33.8	20.5	
53	575	4.80E-04	1.10E+05	1.20E+06	33.5	4.83	POOLED AGE
					33.60	8.40	MEAN AGE
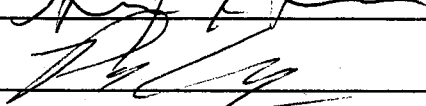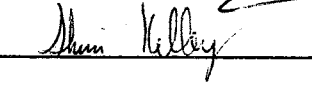
97PT2							
la	2E-10		U (ppm)=	17			
z	5420						
pm	170666						
g	0.5						
ND	11053						
NS	Ni	area	ps	pi	age (Ma)	sdiv (Ma)	
3	58	5.00E-05	6.00E+04	1.16E+06	23.88	14.14	
2	65	7.00E-05	2.86E+04	9.29E+05	14.22	10.21	
9	236	1.50E-04	6.00E+04	1.57E+06	17.61	5.98	
2	79	5.00E-05	4.00E+04	1.58E+06	11.70	8.38	
2	53	7.50E-05	2.67E+04	7.07E+05	17.43	12.56	
2	20	8.00E-06	2.50E+05	2.50E+06	46.09	34.18	
4	106	5.50E-05	7.27E+04	1.93E+06	17.43	8.88	
2	51	3.50E-05	5.71E+04	1.46E+06	18.11	13.06	
3	37	6.00E-05	5.00E+04	6.17E+05	37.39	22.45	
4	87	4.50E-05	8.89E+04	1.93E+06	21.23	10.86	
5	140	7.20E-05	6.94E+04	1.94E+06	16.50	7.51	
14	140	1.00E-04	1.40E+05	1.40E+06	46.09	12.93	
2	50	2.50E-05	8.00E+04	2.00E+06	18.47	13.32	
13	135	6.30E-05	2.06E+05	2.14E+06	44.38	12.90	
3	104	7.00E-05	4.29E+04	1.49E+06	13.33	7.81	
4	86	4.40E-05	9.09E+04	1.95E+06	21.48	10.99	
2	53	2.50E-05	8.00E+04	2.12E+06	17.43	12.56	
8	245	1.00E-04	8.00E+04	2.45E+06	15.08	5.42	
4	32	1.10E-05	3.64E+05	2.91E+06	57.56	30.53	
7	226	1.00E-04	7.00E+04	2.26E+06	14.31	5.49	
1	55	2.50E-05	4.00E+04	2.20E+06	8.40	8.48	
5	93	2.50E-05	2.00E+05	3.72E+06	24.82	11.40	
3	47	2.50E-05	1.20E+05	1.88E+06	29.45	17.54	
2	49	2.50E-05	8.00E+04	1.96E+06	18.85	13.60	
2	51	2.50E-05	8.00E+04	2.04E+06	18.11	13.06	
1	37	2.50E-05	4.00E+04	1.48E+06	12.49	12.66	
3	52	2.50E-05	1.20E+05	2.08E+06	26.63	15.81	
3	31	2.50E-05	1.20E+05	1.24E+06	44.60	26.97	
1	45	2.00E-05	5.00E+04	2.25E+06	10.27	10.38	
95	2003	1.21E-03	7.86E+04	1.66E+06	21.80	2.09	POOLED AGE
					23.60	2.10	MEAN AGE

97BW2

97GW1
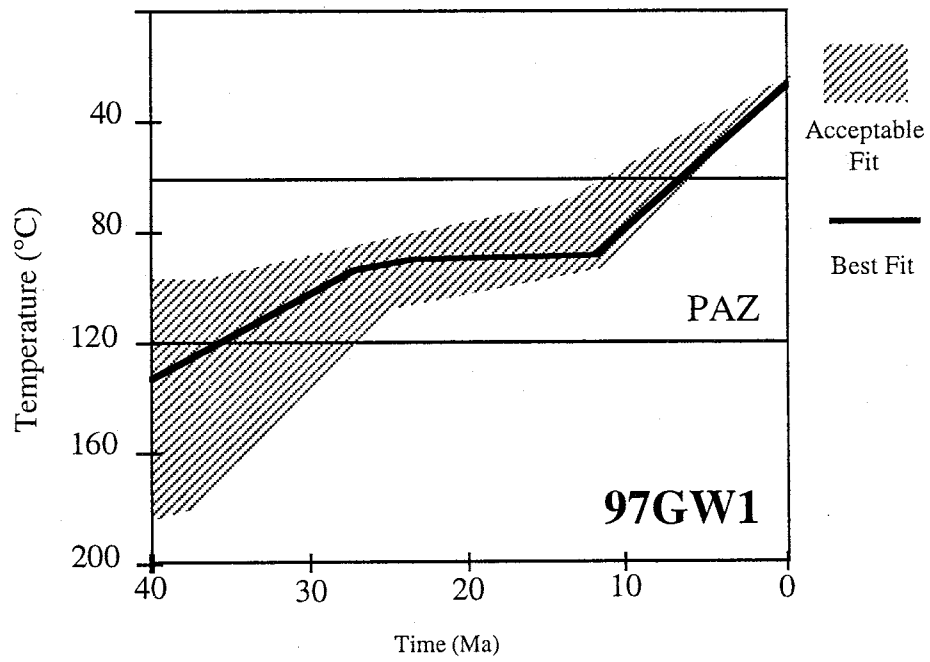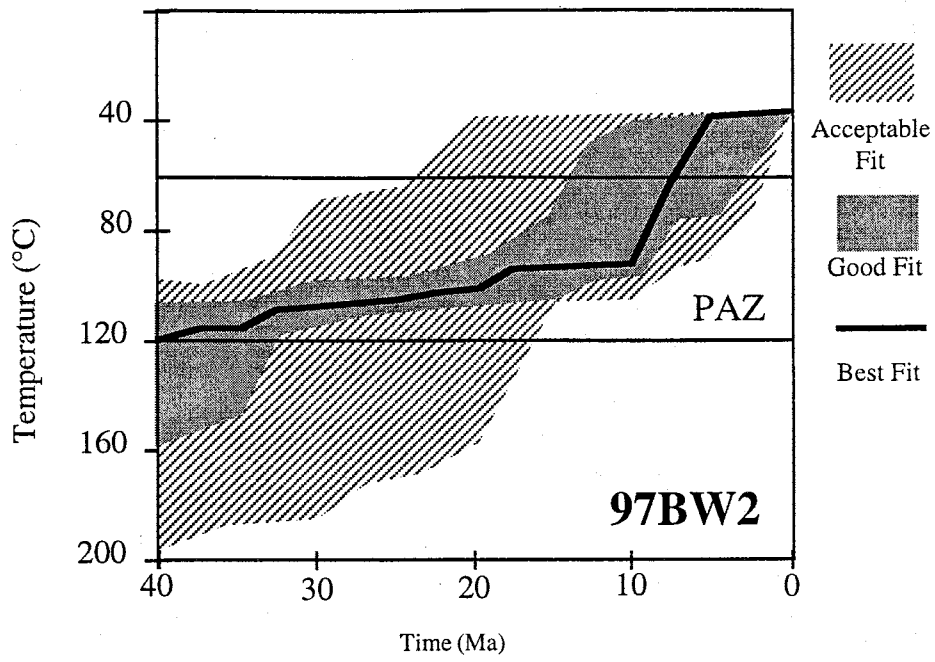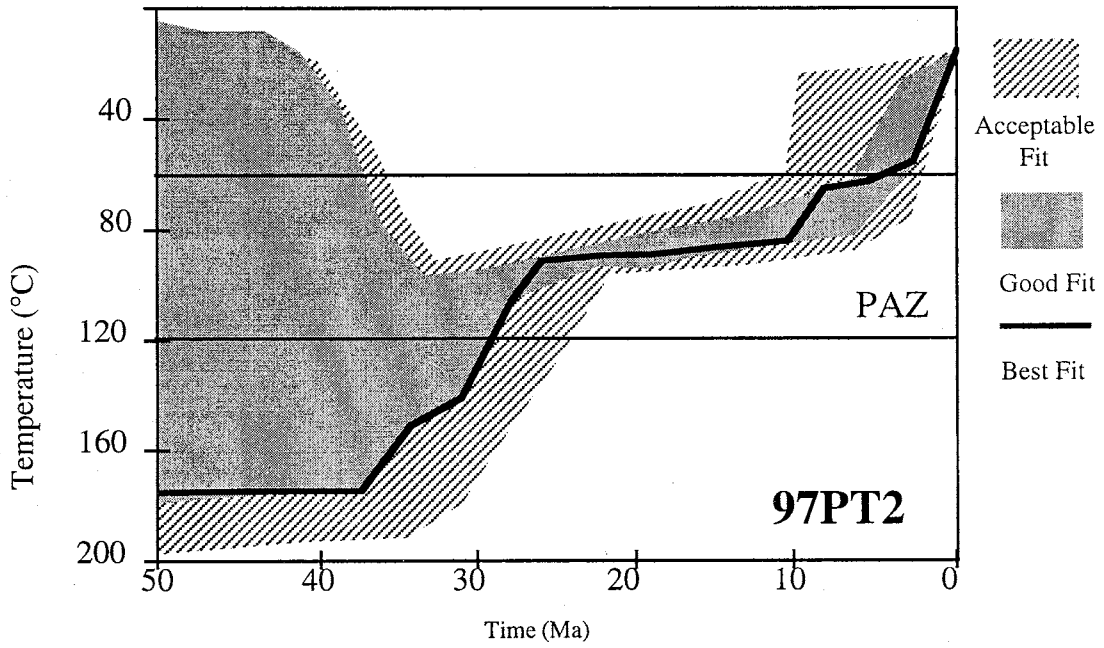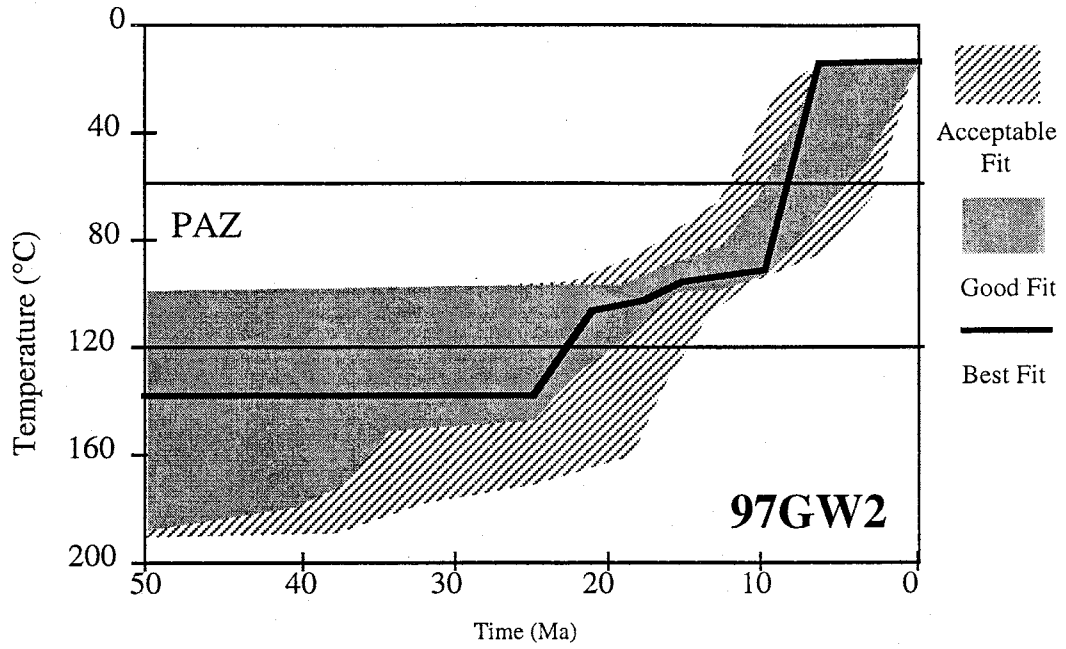
This thesis is accepted on behalf of the faculty
of the Institute by the following committee:

_____ Advisor

_____

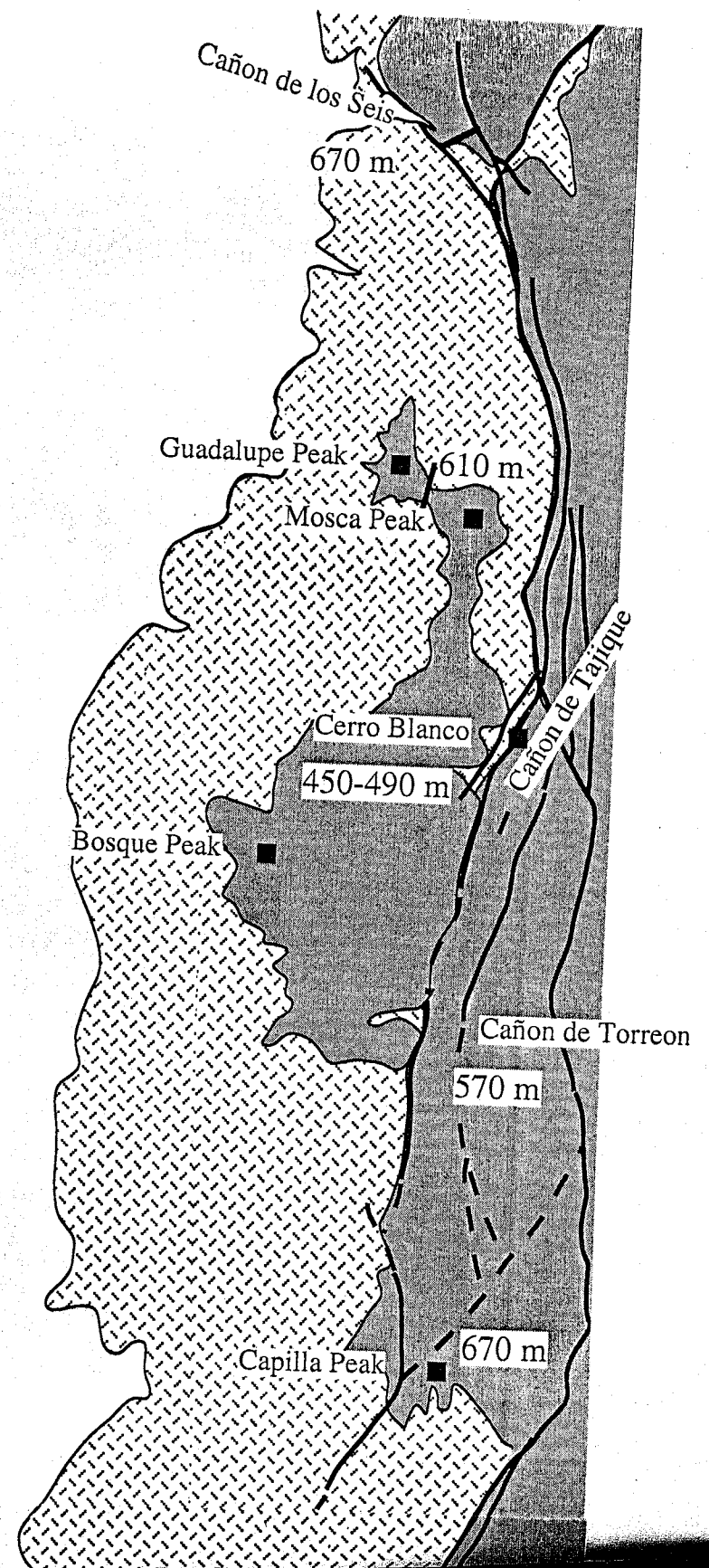_____

_____

_____

Date

I release this document to the New Mexico Institute of Mining and Technology.

_____   5/10/99
Student's Signature   Date

Cañon de los Seis

670 m

Guadalupe Peak ■ 610 m

Mosca Peak ■

Cerro Blanco ■ Cañon de Talique

450-490 m

Bosque Peak ■

Cañon de Torreon

570 m

Capilla Peak ■ 670 m
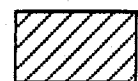
QUATERNARY-Holocene eolian deposits, floodplain deposits, colluvium, and alluvium, and Pliestocene pediments (Meyers et al., 1981).

TERTIARY- Pliocene basalts of Black Mesa. K-Ar age is 3.5Ma (Myers et al., 1986)
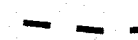
PERMIAN-
   Yeso Formation- orange sandstones and siltstones with yellow-grey gypsiferous limestone (Myers et al., 1986).
   Abo Formation- pale red to red orange and grey fine grained cross-bedded sandstone, siltstone, and shale.
   Bursum Formation-interbedded marine limestones and red-brown shale, slitstone, and sandstone.

PENNSYLVANIAN-
   Wild Cow Formation- sequence of yellow to grey sandstone and conglomerate, with local green to red siltstone and shale with thin to thick limestone beds. (Myers et al., 1986)
   Los Moyos Formation-interbedded grey calcarenite, grey shale, yellow-green siltstone, grey chert, and siltstone.
   Sandia Formation- pale brown to grey or moderate-orange cross-bedded arkose, conglomerate, and sandstone to siltstone.
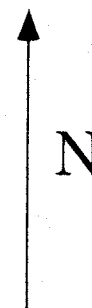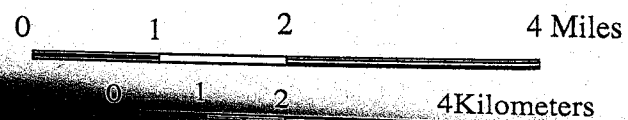
PRECAMBRIAN PRIEST QUARTZ MONZONITE- Pluton of 1.43±0.01Ga quartz monzonite (Thompson et al., 1996).
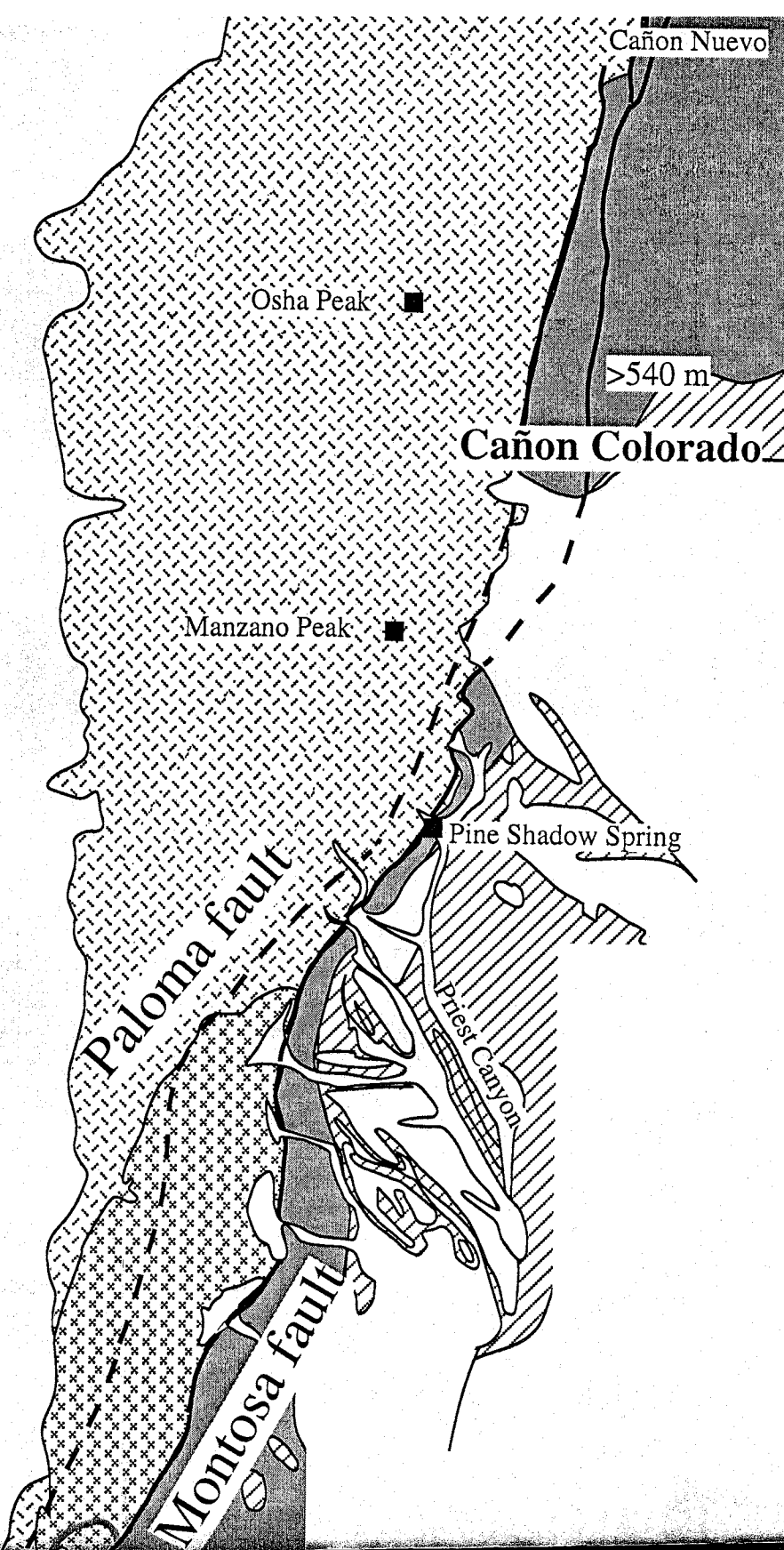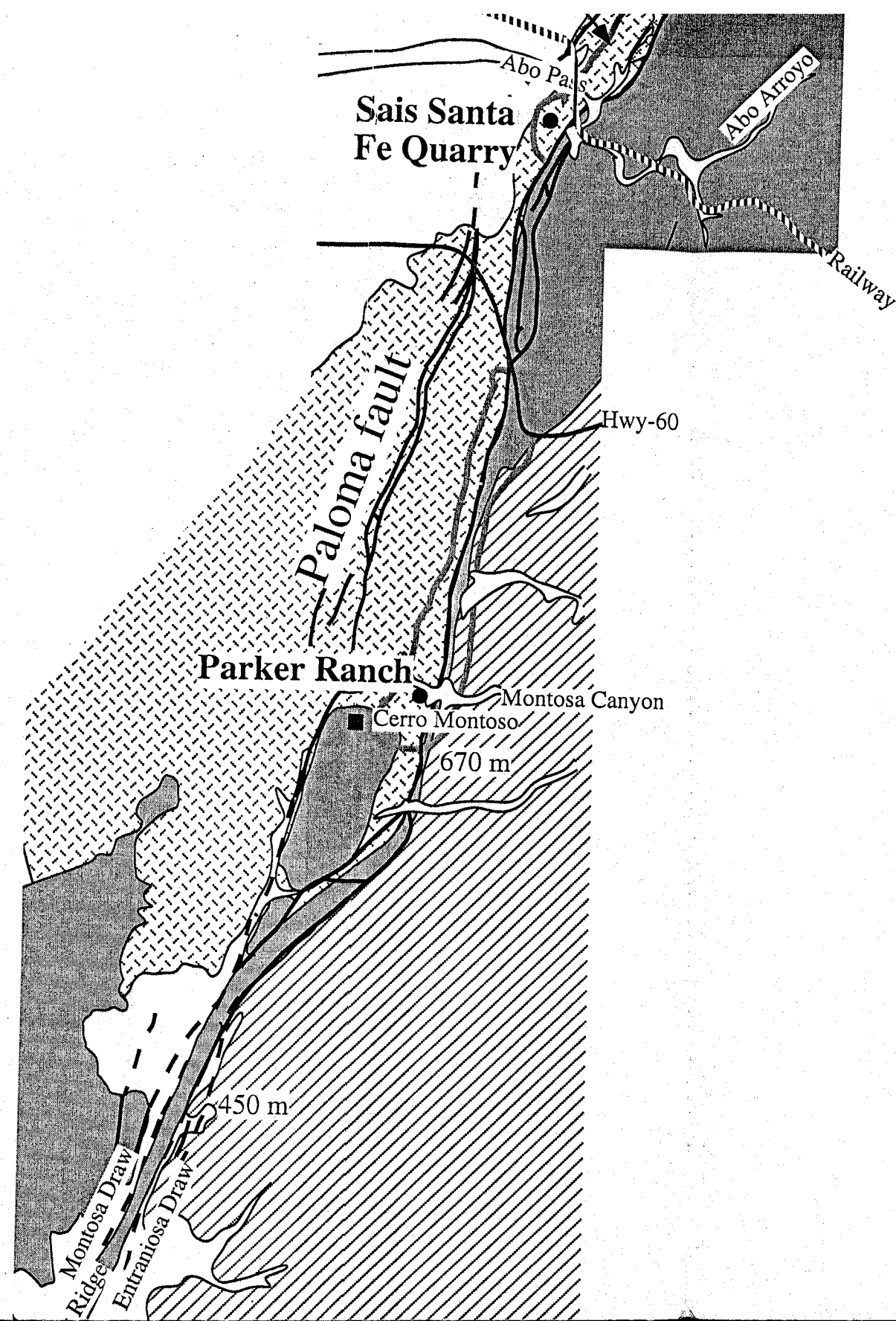
PRECAMBRIAN UNDIFFERENTIATED

—— Known faults

- - - Inferred faults

◯ Study area

N

0   1   2   4 Miles

0   1   2   4 Kilometers

Cañon Nuevo

Osha Peak ■

>540 m

Cañon Colorado

Manzano Peak ■

Pine Shadow Spring

Paloma fault

Priest Canyon

Montosa fault

Sand Canyon

Abo Pass

Sais Santa
Fe Quarry

Abo Arroyo

Railway

Paloma fault

Hwy-60

Parker Ranch

Montosa Canyon

Cerro Montoso

670 m

450 m
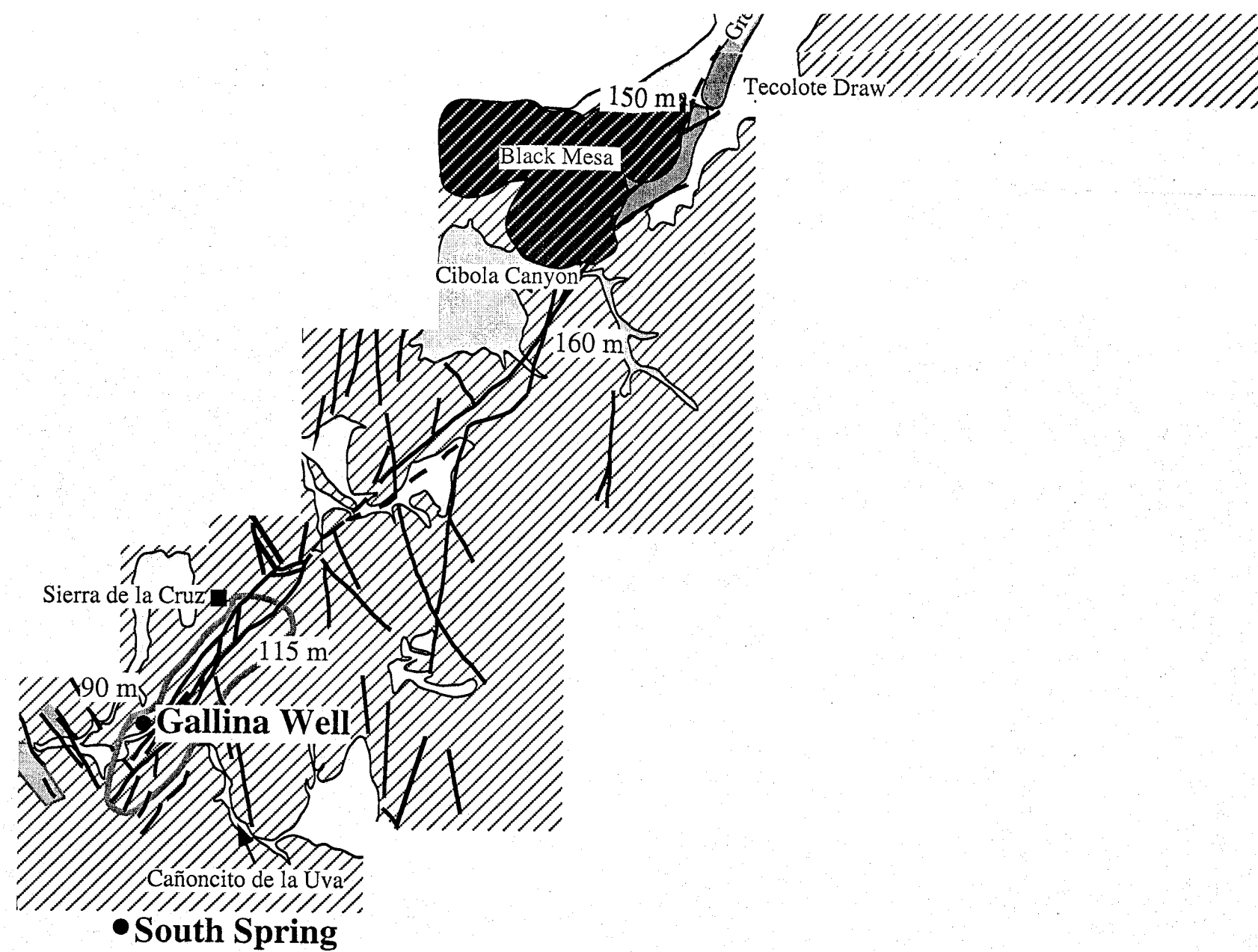
Montosa Draw

Entrañosa Draw

Ridge

Plate 1. Map of the Montosa fault. Names written in bold are areas focused on in this study. If a large area was covered it is outlined with a grey line, such as at Gallina Well, Parker Ranch, and Sand Canyon. Vertical separation is recorded in meters along the fault. North of Black Mesa, separation is reverse, and south it is normal.
From maps by Reiches (1949), Stark (1956), Myers (1973), Myers (1977), Myers and McKay (1971), Myers and McKay (1972), Myers and McKay (1974), Myers et al. (1981), Myers et al. (1986), and Cabezas (1987). Areas where various maps disagreed were resolved by field work.